

Design of the electrode system for the KATRIN main spectrometer

von

Karen Anna Hugenberg

Diplomarbeit in Physik

angefertigt im

Institut für Kernphysik

vorgelegt der

Mathematisch-Naturwissenschaftlichen Fakultät

der

Westfälischen Wilhelms-Universität

Münster

im Januar 2008

Ich versichere, dass ich die Arbeit selbständig verfasst und keine anderen als die angegebenen Quellen und Hilfsmittel benutzt, sowie Zitate kenntlich gemacht habe.

Referent: Prof. Dr. C. Weinheimer

Korreferent: Prof. Dr. J. Wessels

Contents

1	Introduction	1
1.1	Evidence for massive neutrinos	1
1.1.1	The solar neutrino problem	1
1.1.2	Neutrino oscillations	2
1.1.3	Neutrino oscillation experiments	3
1.1.4	Conclusion	7
1.2	Cosmic neutrinos	7
1.3	Measurements of β -decay kinematics	16
1.4	Outline	20
2	The KATRIN experiment	21
2.1	The tritium β - decay	21
2.2	The MAC-E filter	22
2.2.1	Basic principle	22
2.2.2	MAC-E filters in the KATRIN setup	27
2.2.3	Characteristics of a MAC-E filter	28
2.2.4	The wire electrode	30
2.3	Setup of the KATRIN experiment	32
3	Simulation tools	35
3.1	Magnetic field calculations	35
3.1.1	magfield2	39
3.1.2	magfield3	40
3.1.3	Fieldlinepot	42
3.2	Electric field calculations	44
3.2.1	elcd3_2	45
3.2.2	elcd3_3	47
3.2.3	gmainspec	50
3.2.4	MBEM - an improved method for calculating electric fields	50
3.3	Tracking	50
3.3.1	Traj	50
3.3.2	Transmission	52
4	Design simulations for the wire electrode	55
4.1	Tolerance simulations for the cylindrical part of the wire electrode	55
4.2	Detailed simulations of the wire electrode	59

5	Electron gun emission characteristics	67
5.1	Source properties required for calibration	67
5.2	The pre-spectrometer electron gun setup	69
5.3	Simulations of the electron gun emission	71
5.3.1	Geometry	71
5.3.2	Tracking the electrons from tip to magnet	73
5.3.3	General analysis	79
5.4	Summary	85
6	Discharges and Penning traps	89
6.1	Discharge mechanisms	89
6.1.1	Townsend discharge	89
6.1.2	Vacuum breakdown	92
6.1.3	Penning discharge	93
6.2	Discharge experience in predecessor experiments	100
6.2.1	The Troitsk experiment	100
6.2.2	The Mainz experiment	101
6.3	Particle trapping in the KATRIN pre-spectrometer	112
6.3.1	Experiments	112
6.3.2	Simulations of an additional electrode	120
6.4	The Penning trap between pre-spectrometer and main spectrometer . . .	127
6.5	Penning traps in the main spectrometer	127
6.5.1	Design requirements	127
6.5.2	Models for a shielding electrode fitting through the flange	129
6.5.3	Models for a shielding electrode exceeding the flange diameter . . .	134
6.5.4	Conclusion	137
7	Summary and outlook	139
A	Technical drawings	141
B	The magnetic field design	143

1 Introduction

Since their conception in 1930 by W. Pauli¹, neutrinos continue to fascinate scientists. Their elusive nature makes the investigation of neutrinos an intellectually and technologically challenging branch of nuclear and astroparticle physics with prospects to study the beginning of the Universe [Dol02, Han06] as well as supernova explosions ([Hir87, Bio87] and analyses based on these) and the inner structure of the Earth [Ara05].

One aspect that scientists concentrate on is the question of the absolute neutrino mass scale. This topic will be addressed in this chapter. In the first section the evidence for massive neutrinos will be discussed briefly. In the next section the properties of cosmic neutrinos and their implications on the mass scale are discussed. In the last section the search for the absolute neutrino mass scale by investigating the kinematics of β -decay is described.

1.1 Evidence for massive neutrinos

1.1.1 The solar neutrino problem

Neutrinos produced in solar fusion reactions have been studied for several decades already. The net fusion reaction² amounts to [Zub04]



with 26.73 MeV being radiated as thermal energy. The neutrinos are released in a number of different reactions (not listed here), each with a distinct ν energy signature. The calculated spectrum can be seen in figure 1.1.

The first measurements of the solar neutrino flux in the 1960s at the Homestake Experiment by J. N. Bahcall and R. Davis Jr.³ pointed either to deficiencies in the solar models, or to physics beyond the Standard Model: No neutrinos could be detected and an upper limit of 3 SNU⁴ was determined, while a solar neutrino flux of (7.5 ± 3.0) SNU was predicted [Dav64, Bah64]. Although solar neutrinos were successfully detected shortly afterwards, a discrepancy of about a factor 3 remained between the theoretical predictions and measured rates. This was also called *the solar neutrino problem*, and was confirmed by several other experiments (e.g. Gallex, SAGE) in the 1990s. A possibility

¹Pauli used the neutrino as a 'desperate remedy' to save the energy and angular momentum conservation. He first mentioned them in a letter to his colleagues at a conference in Tübingen [Pau30].

²including the annihilation reaction of two positrons with two additional electrons

³R. Davis Jr. was awarded the Nobel prize in Physics 2002 'for pioneering contributions to astrophysics, in particular for the detection of cosmic neutrinos'

⁴The Solar Neutrino Unit is defined as 10^{-36} neutrino captures per target atom and second.

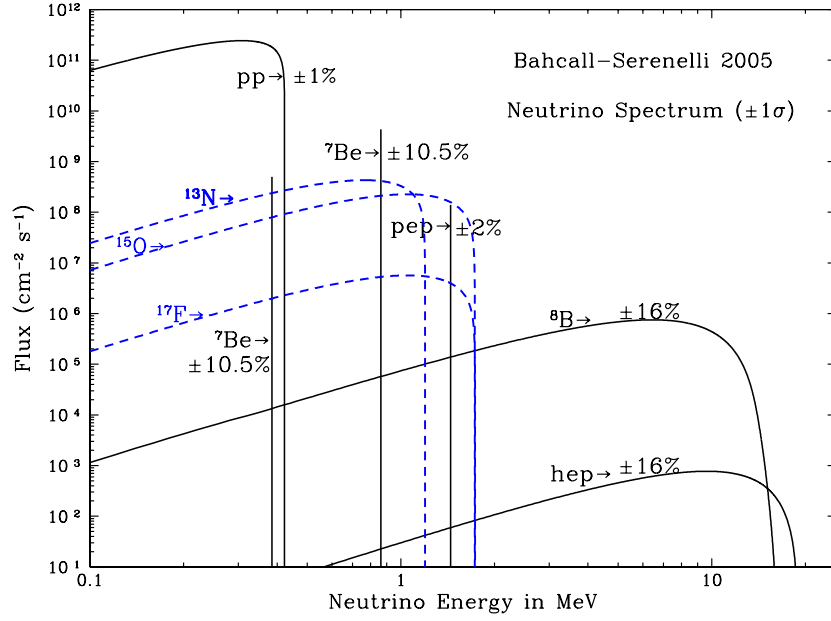


Figure 1.1: The solar neutrino flux divided into the different emission processes, figure taken from [Bah05]

to explain the apparent loss of electron neutrinos is the neutrino flavour oscillation model with massive neutrino eigenstates that are not identical to the eigenstates of the weak interaction.

1.1.2 Neutrino oscillations

If the neutrino eigenstates that couple to the weak interaction do not correspond to the mass eigenstates, they can be expressed as a superposition of these

$$|\nu_\alpha\rangle = \sum_i U_{\alpha i}^* |\nu_i\rangle, \quad (1.2)$$

with α being the neutrino flavour and i the number of the mass eigenstate. The unitary matrix U , also called Maki-Nakagawa-Sakata-Pontecorvo matrix (MNSP), can be decomposed into rotation matrices describing the mixing between the single states:

$$U = \begin{pmatrix} 1 & 0 & 0 \\ 0 & \cos \Theta_{23} & \sin \Theta_{23} \\ 0 & -\sin \Theta_{23} & \cos \Theta_{23} \end{pmatrix} \cdot \begin{pmatrix} \cos \Theta_{13} & 0 & \sin \Theta_{13} e^{-i\delta} \\ 0 & 1 & 0 \\ -\sin \Theta_{13} e^{-i\delta} & 0 & \cos \Theta_{13} \end{pmatrix} \cdot \begin{pmatrix} \cos \Theta_{12} & \sin \Theta_{12} & 0 \\ -\sin \Theta_{12} & \cos \Theta_{12} & 0 \\ 0 & 0 & 1 \end{pmatrix} \cdot \begin{pmatrix} e^{i\alpha_1/2} & 0 & 0 \\ 0 & e^{i\alpha_2/2} & 0 \\ 0 & 0 & 1 \end{pmatrix}. \quad (1.3)$$

with Θ_{ij} being the mixing angles. The factor $e^{-i\delta}$ takes into account the possibility that neutrino oscillations violate CP symmetry. The last matrix needs to be incorporated if the neutrinos are Majorana particles.

The time development of a quantum mechanical state is determined by its energy. As the neutrino flavour α is a superposition of states that will get the same energy but have different masses, the contribution of each state after propagating for a time interval t will give a different phase $e^{-i\frac{m_i^2}{2E}t}$, resulting in the possibility to measure the eigenstate β instead of α . The rate at which the transition between the states takes place is dependent upon the change in the contribution for each mass term. This results in a dependency on the differences between the squared masses $\Delta m_{ij}^2 = |m_i^2 - m_j^2|$. As the neutrinos are highly relativistic, we can approximate the time by the distance L covered in that time: $t \approx L/c$. The transition probability is then given by

$$\begin{aligned} P(\nu_\alpha \rightarrow \nu_\beta) &= |\langle \nu_\beta(t) | \nu_\alpha(t) \rangle|^2 \\ &= \delta_{\alpha\beta} \\ &\quad - 4 \sum_{i>j} \Re(U_{\alpha i}^* U_{\beta i} U_{\alpha j} U_{\beta j}^*) \sin^2 \left(1.27 \Delta m_{ij}^2 \frac{L}{E} \right) \\ &\quad + 2 \sum_{i>j} \Im(U_{\alpha i}^* U_{\beta i} U_{\alpha j} U_{\beta j}^*) \sin \left(2.54 \Delta m_{ij}^2 \frac{L}{E} \right), \end{aligned} \quad (1.4)$$

with L in km, E in GeV and Δm_ν^2 in eV^2/c^4 .

Thus, the neutrino oscillation model is able to explain the observed disappearance of neutrinos of a certain flavour. Generally, two ways of searching experimentally for neutrino oscillations consist of

- looking for the appearance of a neutrino flavour β other than the flavour α that was emitted at the source, or else
- detecting the disappearance of a neutrino flavour correlating to a length scale at a fixed energy.

1.1.3 Experimental confirmation of neutrino oscillation and measurements of its parameters

Atmospheric neutrinos Experimental evidence of neutrino oscillation was first found by the Super-Kamiokande experiment in 1998. The data showed with high accuracy that the number of atmospheric muon neutrinos interacting in the detector is dependent on the incident angle (an example for Sub-GeV energy electrons and muons is shown in figure 1.2). The muon neutrinos passing through the Earth ($\cos \Theta < 0$) have a longer path and can thus oscillate into tau neutrinos.

For Θ_{23} , one of the parameters of the neutrino mixing matrix U , the limit

$$\sin^2(2\Theta_{23}) > 0.92 \quad (1.5)$$

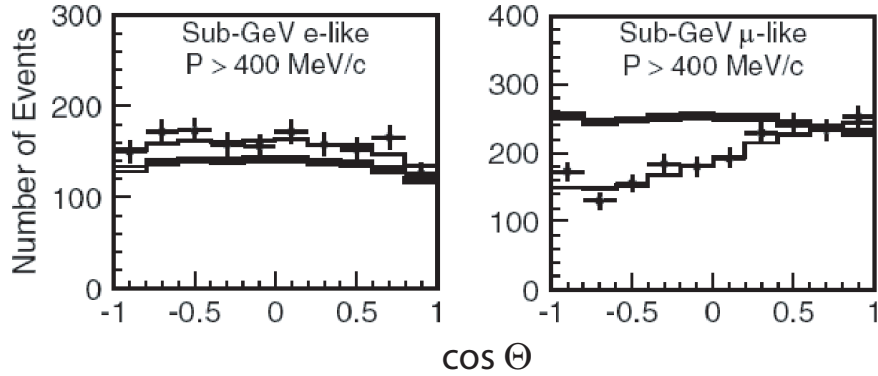


Figure 1.2: The zenith angle distribution for Sub-GeV neutrino energies with momentum $P > 400 \text{ MeV}/c$ measured by Super-Kamiokande. The rectangles describe simulated data without neutrino oscillations, the crosses the measured data and the lines the best fit for $\nu_\mu \leftrightarrow \nu_\tau$. In the left panel the data for electron neutrino events are shown, in the right panel the for muon neutrinos. Figure taken from reference [Ash05]

was determined and the mass difference Δm_{23}^2 constrained to the range [Ash05]

$$1.5 \cdot 10^{-3} \text{ eV}^2 < \Delta m_{23}^2 < 3.4 \cdot 10^{-3} \text{ eV}^2. \quad (1.6)$$

Solar neutrinos Shortly after the Super-Kamiokande publication hinting at neutrino oscillation, the SNO collaboration found evidence for oscillations in the field of solar neutrinos. The experiment was able to measure the total neutrino flux for all flavours combined as well as the flux of electron neutrinos by the reactions



The results state that only one third of all neutrinos coming from the Sun still have their initial flavour ν_e when reaching the Earth [Aha05]

$$\frac{\phi(\nu_e)}{\phi(\nu_e) + \phi(\nu_{\mu,\tau})} = 0.340 \pm 0.023(\text{stat})_{-0.031}^{+0.029}(\text{syst}), \quad (1.10)$$

with ϕ_α the measured flux of the neutrino flavour α . As the Sun only emits electron neutrinos, the appearance of the other neutrino flavours proves the oscillation theory. The total neutrino flux for all flavours is consistent with the solar neutrino flux predicted by the standard solar model (SSM) (see also figure 1.3).

The total analysis given in [Aha05] for the salt measurements⁵ in combination with the

⁵For the second phase of data taking purified NaCl was added to the D₂O target material to enhance the capture and detection efficiencies of the neutron produced in reaction (1.8). These measurements are commonly called the salt measurements.

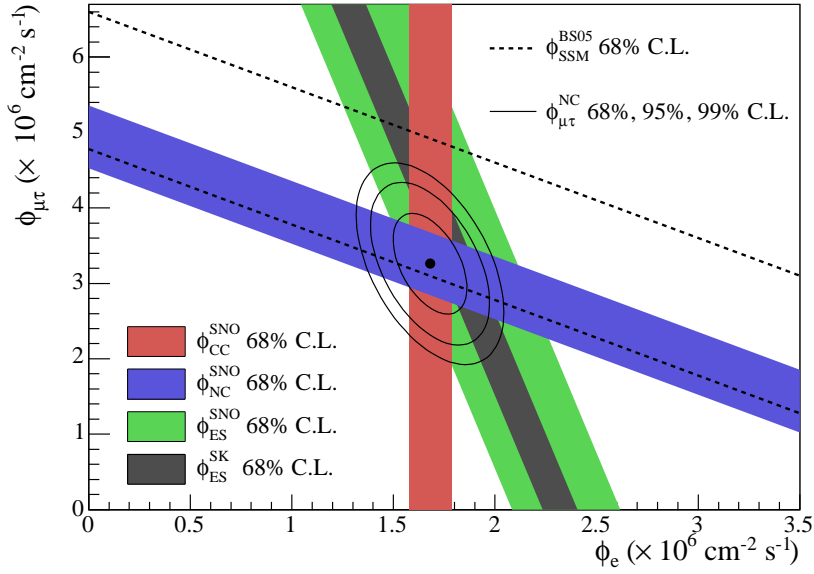


Figure 1.3: The neutrino flux of flavour μ , τ versus the flux of electron neutrinos as measured by the SNO and Super-Kamiokande experiments. The dashed line shows the predicted solar neutrino flux (SSM). The point and its surrounding lines represent ϕ_e from the CC flux and $\phi_{\mu\tau}$ from the NC - CC difference at various confidence levels. Figure taken from reference [Aha05]

KamLAND data yields a mixing angle of

$$\Theta_{12} = (33.9_{-2.2}^{+2.4})^\circ \quad (1.11)$$

and a mass difference of

$$\Delta m_{21}^2 = (8.0_{-0.4}^{+0.6} \cdot 10^{-5}) \text{eV}^2. \quad (1.12)$$

Reactor neutrinos In a nuclear reactor, mainly electron anti-neutrinos are emitted. Their rate is dependent on the mixing angles Θ_{13} and Θ_{12} as well as the mass differences Δm_{21}^2 and Δm_{32}^2 . For large distances the transition probability can be approximated and only depends on Θ_{12} and Δm_{21}^2 , as the term depending on Θ_{13} oscillates rapidly with L and averages to zero. For short distances ($L < 5$ km) the influence of Θ_{12} and Δm_{21}^2 is negligible and the transition probability is mainly dependent on the parameters Θ_{13} and Δm_{32}^2 .

With a threshold of 1.8 MeV for the neutrino energy, the KamLAND experiment observed electron anti-neutrinos from reactors with an average distance of $L = 180$ km by the reaction

$$\bar{\nu}_e + p \rightarrow e^+ + n, \quad (1.13)$$

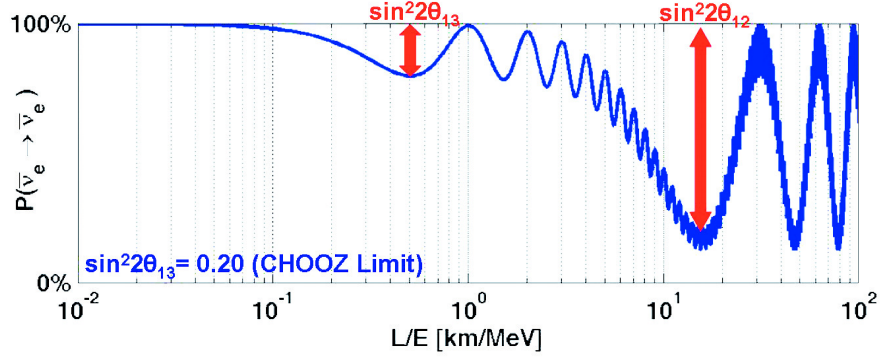
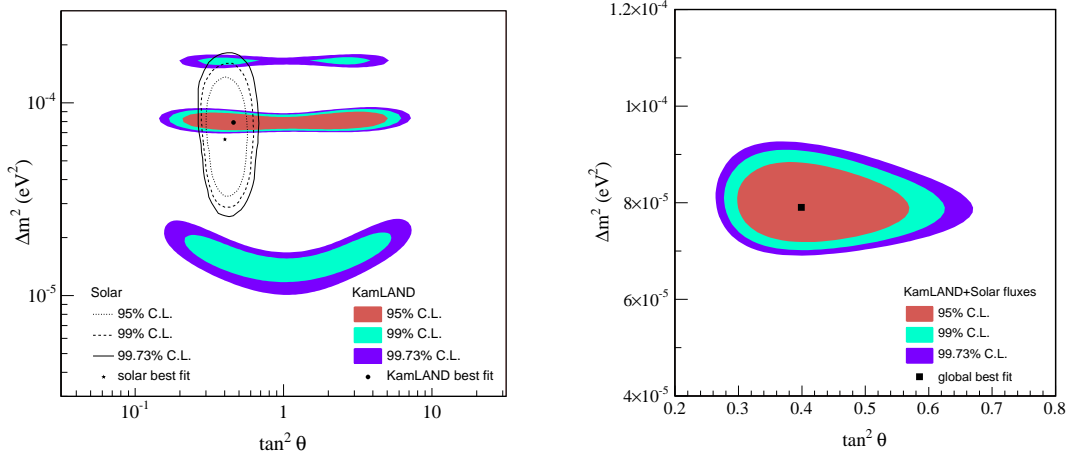


Figure 1.4: The transition probability $\bar{\nu}_e \rightarrow \bar{\nu}_e$ is dependent on the energy E and traveled distance L of the particle. At short distances the oscillation is dominated by the angle Θ_{13} , at large distances the angle Θ_{12} is more prominent. Figure taken from [KAT06]

and is therefore sensitive to the parameters Θ_{12} and Δm_{21}^2 . Evidence for the disappearance of electron antineutrinos has been observed by the experiment. The best-fit for a



(a) Allowed region of neutrino oscillation parameters measured by the KamLAND experiment (colour) and the SNO experiment (contours)

(b) The combination of the SNO data with the KamLAND measurements restricts the neutrino parameters to the LMA I region

Figure 1.5: Oscillation parameters. Figures taken from reference [Aha05]

rate-and-shape analysis of the KamLAND data yields

$$\Delta m_{21}^2 = (7.9_{-0.5}^{+0.6}) \cdot 10^{-5} \text{ eV}^2 \quad (1.14)$$

and

$$\tan^2 \Theta_{12} = 0.46 \quad (1.15)$$

with a large uncertainty on $\tan^2 \Theta_{12}$. Combining the results with the solar measurements of SNO (see figure 1.5b) constrains the angle to

$$\tan^2 \Theta_{12} = 0.40_{-0.07}^{+0.10}. \quad (1.16)$$

The Double Chooz collaboration is currently setting up two detectors in a distance of $L_1 = 0.30$ km and $L_2 = 1.05$ km of a nuclear reactor. The experiment will measure $\sin^2 2\Theta_{13}$ up to a sensitivity of $\sin^2 2\Theta_{13} < 0.03$ at 90% C.L. [Ard06].

Accelerator neutrinos Assuming negligible mixing angle Θ_{13} , accelerator neutrino experiments are sensitive to the oscillation of a muon neutrino into a tau neutrino and can therefore determine the parameters Θ_{23} and Δm_{32}^2 . This has been measured with a neutrino beam from the KEK facility to Super-Kamiokande, yielding under the assumption $\sin^2 2\Theta_{12} = 1$ a range for the mass difference of [Ahn06]

$$1.9 \cdot 10^{-3} \text{ eV}^2 < m_{32}^2 < 3.5 \cdot 10^{-3} \text{ eV}^2 \quad (1.17)$$

with a best-fit value of

$$\Delta m_{32}^2 = 2.8 \cdot 10^{-3} \text{ eV}^2. \quad (1.18)$$

The recently started experiment OPERA aims to detect the tau neutrino produced in the $\nu_\mu \rightarrow \nu_\tau$ oscillation.

1.1.4 Conclusion

A consistent picture of neutrino oscillations is presently being supported by the results of various experiments. The coupling parameters between the different neutrino flavours has been determined or restricted, and also the mass squared differences between the different mass eigenstates has been measured. A compilation of the available data can be found in figure 1.6 [Mur06].

Some questions still remain open:

- Oscillation experiments only measure the differences between squared masses. What is the absolute mass scale? Are the masses degenerate?
- How are the neutrinos ordered? As the sign of the mass differences is not known, normal hierarchy ($m_1 < m_2 < m_3$) as well as inverted ($m_3 < m_1 < m_2$) is possible.

1.2 Cosmic neutrinos

Today's cosmological models describe the evolution of the Universe starting with a singularity, the big bang. In the beginning, high temperatures and densities dominate the behaviour of the particles. Quarks, leptons and the intermediate bosons are in equilibrium, interacting with a rate Γ_i higher than the expansion rate of the Universe H

$$\Gamma_i > H. \quad (1.19)$$

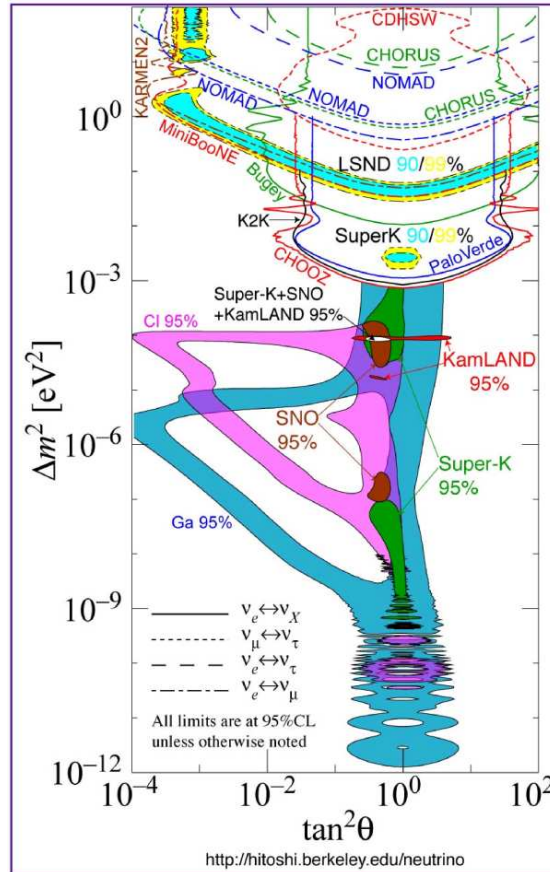


Figure 1.6: The favoured (filled) or excluded (separated by lines) regions for the different neutrino oscillation parameters measured in different experiments. Figure taken from reference [Mur06]

The interaction rate is dependent on the energy of the particles. With the adiabatic expansion of the Universe the energy decreases. If the interaction rate of one kind of particles falls below the expansion rate, the Universe becomes transparent for the particle and its distribution decouples from the rest of the plasma. As the particles do not interact any more, the distribution remains the same and therefore reflects the properties of the early Universe. A timeline of the evolution of the Universe with the decoupling and formation times of different particles can be seen in figure 1.7.

An important evidence supporting the big bang theory is the cosmic microwave background radiation, short CMBR. Photons freeze out of the equilibrium at a temperature at which protons and electrons combine to form hydrogen H . No free electrons are available any more for interaction. Therefore the Universe becomes transparent for photons. Due to the expansion of the Universe the wavelength of the photons increases, corresponding to a temperature decrease. Today, the temperature of the CMBR is measured

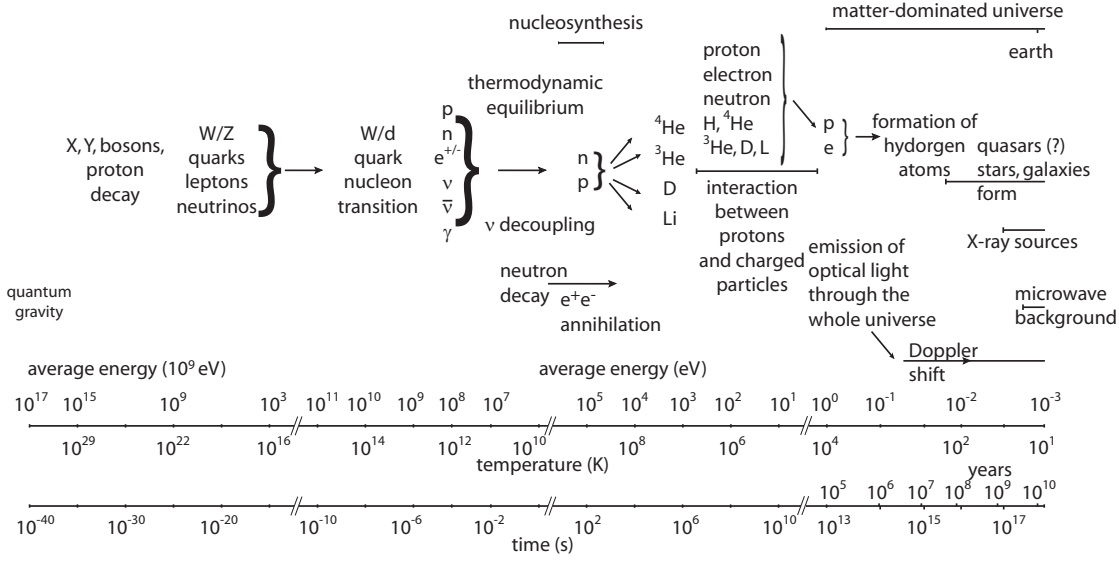


Figure 1.7: A timeline of the evolution of the Universe, adapted from [Kla97]

[Mat99]⁶ to be

$$T_\gamma = (2.725 \pm 0.002) \text{ K}, \quad (1.20)$$

and the spectrum corresponds to that of an ideal black body.

The decoupling temperature of the neutrinos can be approximated with the weak interaction rate Γ :

$$\Gamma \equiv \frac{\dot{n}_\nu}{n_\nu} \propto n \langle \sigma_{\nu_e n_e} \rangle, \quad (1.21)$$

with the number density of neutrinos $n \propto T^3$ and $\langle \sigma_{\nu_e n_e} \rangle \sim \mathcal{O}(10^{-2}) \frac{T^2}{m_W^4}$. The Hubble expansion rate depends on T^2 :

$$H = \left(\frac{8\pi G_N \rho}{3} \right) \sim 1.66 \frac{N(T)^{\frac{1}{2}} T^2}{M_P} \quad (\text{using } M_P = G_N^{-1/2}) \quad (1.22)$$

ρ is the total energy density in the equilibrium plasma. It can be expressed in terms of the effective number of degrees of freedom $N(T)$. This quantity is temperature dependent as particles freeze out and thus decrease this number. M_P is the Planck mass. Together with equation (1.21) a decoupling temperature $T_{d,\nu}$ of [Yao06]

$$T_{d,\nu} \lesssim \left(500 \frac{m_W^4}{M_P} \right)^{\frac{1}{3}} \sim \mathcal{O}(1 \text{ MeV}) \quad (1.23)$$

⁶For their discovery of the blackbody form and anisotropy of the CMB the physicists J. C. Mather and G. F. Smoot were rewarded the Nobel prize in physics 2006.

can be derived.

The photon background decouples later as the electromagnetic interaction with the remaining electrons is still possible at $T < T_{d,\nu}$. The photons are heated up again at temperatures of $T \lesssim m_e$ when the electrons and positrons start to annihilate (see also figure 1.7). Using entropy conservation the relation between the two background temperatures can be calculated:

$$T_\nu = \left(\frac{4}{11}\right)^{\frac{1}{3}} T_\gamma. \quad (1.24)$$

Therefore the temperature of the neutrino background today is predicted to be

$$T_\nu(t = \text{today}) \approx 1.945 \text{ K} = 1.6 \cdot 10^{-4} \text{ eV}. \quad (1.25)$$

Although there exist many experiments that investigate high-energy neutrinos from astrophysical sources⁷, none of them is able to measure neutrinos of such low energies.

In contrast to oscillation experiment that only measure squared mass differences, limits on the absolute neutrino mass scales can be extracted from cosmological models.

The total energy density of the Universe plays an important role for cosmological models. The Friedmann-Lemaître equations

$$H^2 \equiv \left(\frac{\dot{R}}{R}\right)^2 = \frac{8\pi G_N \rho}{3} - \frac{k}{R^2} + \frac{\Lambda}{3} \quad (1.26)$$

$$\frac{\ddot{R}}{R} = \frac{\Lambda}{3} - \frac{4\pi G_N}{3}(\rho + 3p) \quad (1.27)$$

offer a possibility to describe the evolution of the Universe. Λ is the cosmological constant, ρ gives the energy density and k is a parameter describing the geometric curvature. Assuming $\Lambda = 0$, equation (1.26) yields for $k = 0$ the critical density ρ_c

$$\begin{aligned} \rho_c &= \frac{3H^2}{8\pi G_N} = 1.88 \cdot 10^{-26} h^2 \text{ kg m}^{-3} \\ &= 1.05 \cdot 10^{-5} h^2 \text{ GeV cm}^{-3}. \end{aligned} \quad (1.28)$$

h^2 is the scaled Hubble parameter with $H \equiv 100h \text{ km s}^{-1} \text{ Mp c}^{-1}$. The critical density offers a possibility to parametrise the Universe. The cosmological density parameter is described as the ratio between the energy density and the critical density

$$\Omega_{tot} = \frac{\rho}{\rho_c} \quad (1.29)$$

and offers a measure to describe the curvature of the Universe which depends on its energy:

$$\frac{k}{R^2} = H^2(\Omega_{tot} - 1). \quad (1.30)$$

⁷e.g. IceCube as successor of the Arctic Muon And Neutrino Detector Array for the southern and KM3Net, a collaboration arising from Antares, Nemo and Nestor on the northern hemisphere search for neutrinos of energies in the TeV to PeV range (for further information see e.g. reference [Ahr01]).

For a flat Universe, the cosmological density parameter has to be $\Omega_{tot} = 1$. It can also be described as the sum of various energy density contributions:

$$\Omega_{tot} = \Omega_m + \Omega_\Lambda \quad (1.31)$$

with Ω_m the matter density and Ω_Λ the density of Dark Energy⁸, which only contributes, if $\Lambda \neq 0$. The matter density Ω_m can be subdivided further

$$\begin{aligned} \Omega_m &= \Omega_{dm} + \Omega_b \\ &= \Omega_{CDM} + \Omega_\nu + \Omega_b, \end{aligned} \quad (1.32)$$

with Ω_{dm} the Dark Matter density⁹ and Ω_b the baryon density. The dark matter content of the Universe can be categorized into Hot Dark Matter (HDM) identified with particles such as neutrinos (Ω_ν), which were relativistic at early times and Cold Dark Matter (CDM) consisting of non-relativistic heavy particles whose nature is not yet known (Ω_{CDM}). The current cosmological models assume that the Universe is dominated by Dark Energy Λ (see figure 1.8), as observations indicate an acceleration of the expansion of the Universe that cannot be explained with the energy density of matter and Dark Matter alone. With a prior on the Hubble parameter, the WMAP three-year data indicate that the Universe is flat [Yao06]

$$\Omega_{tot} = 1.003_{0.017}^{+0.013} \quad (1.33)$$

thus providing another indication for Dark Energy.

Neutrinos do not interact electromagnetically. Thus they cannot be observed by electromagnetic radiation and therefore belong to the Dark Matter. The neutrino density for neutrino masses in the range $5 \cdot 10^{-4} \text{ eV} < m_\nu < 1 \text{ MeV}$ is given by the standard weak interaction [Yao06]:

$$\Omega_\nu h^2 = \frac{\sum m_\nu}{93 \text{ eV}}. \quad (1.34)$$

By the conservative assumption $\Omega_\nu \leq 1$ ¹⁰ a mass limit of [Han06]

$$m_\nu \lesssim \frac{46 \text{ eV}}{N_\nu} \quad (1.35)$$

⁸Dark Energy makes up the unobservable 'rest' of the Universe. It is also called vacuum energy as it is assumed to have negative pressure $p < 0$ that gives rise to the accelerated expansion of the Universe observed today.

⁹Dark Matter is defined as matter that cannot be observed directly, as it does not interact electromagnetically, but is seen in effects it has, for example, on the rotation of galaxies. Neutrinos belong to the category Hot Dark Matter as they behave relativistically over a long period of time. In the common cosmological models, however, Cold Dark Matter (CDM) is supposed to make up most of the Dark Matter content of the Universe. It consists of non-relativistic heavy particles and has not been directly observed up to now. Possible CDM candidates are e.g. WIMPS (weakly interacting massive particles).

¹⁰This assumption is very loose, as the total content of the Universe Ω_{tot} is known to amount to one (see equation (1.33)) and the neutrinos contribute only a small fraction to it.

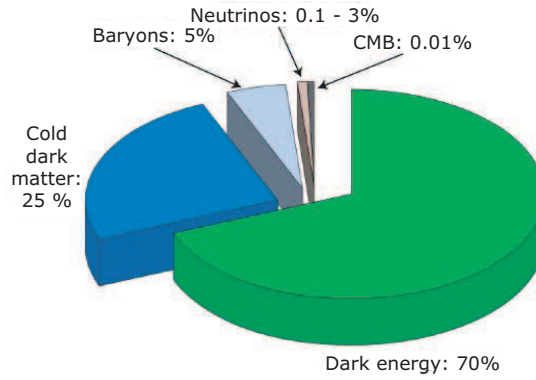


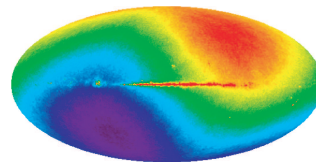
Figure 1.8: Content of the Universe in today's model, the Λ CDM Universe, figure taken from [KAT06]

can be found. This boundary has already improved by the laboratory direct neutrino mass measurements in Mainz and Troitsk which yield an upper neutrino mass limit of $m_{\nu_e} < 2.3 \text{ eV}$ [Kra05], thus an upper bound on the sum of all neutrino masses is $\sum m_\nu \leq 7 \text{ eV}$.

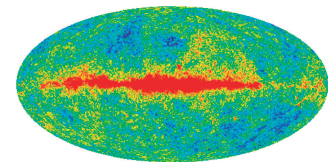
Stronger bounds on the neutrino mass can be derived if the structure formation of the Universe is considered. On small scales, such as galactical diameters the Universe is inhomogeneous. Moving on to larger scales¹¹, the fluctuations become negligible. This can be seen in figure 1.9a.



(a) CMB observed in a temperature range between 0.0000 K and 4.0000 K



(b) CMB observed in a temperature range between 2.7210 K and 2.7290 K



(c) CMB observed in a temperature range between 2.7249 K and 2.7251 K

Figure 1.9: False color images of simulation of the WMAP detection potential. The difference between the figures is the temperature range indicated by the colors. In figure 1.9a the temperature distribution seems homogeneous and no structure is visible. The dipole anisotropy seen in plot 1.9b is a result of the solar motion in front of the homogeneous background. In figure 1.9c the radiation of the milky way dominates the spectra in the central plane. Figures taken from reference [WMAP].

¹¹e.g. surveys regarding the large scale structure such as the Sloan Digital Sky Survey (for further information see <http://www.sdss.org/>) and the Galaxy Redshift Survey using the Two degree Field system at the Anglo-Australian Telescope (2dFGRS, for further information see <http://www.mso.anu.edu.au/2dFGRS/>), surveys of type Ia supernovae (w.g. Supernova Cosmology Project, <http://supernova.1bl.gov>, and High-z Supernova Search, <http://www.cfa.harvard.edu/supernova/HighZ.html>) and the cosmic microwave background.

The measured anisotropies and polarization direction of the oldest light can be seen in figure 1.10. The data was taken with an angular resolution of 0.3° and a sensitivity of $20 \mu\text{K}$ [WMAP].

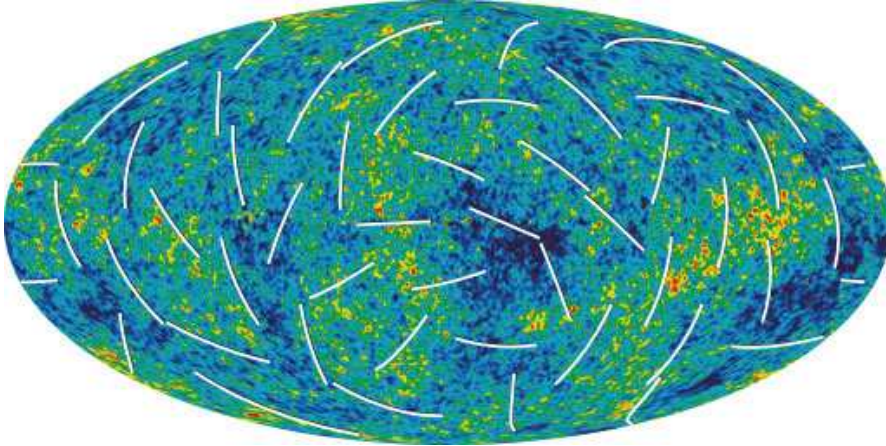


Figure 1.10: CMB fluctuation and polarization measured by the WMAP project. Figure taken from reference [WMAP].

The temperature fluctuation can be expanded into the spherical harmonics $Y_{lm}(\Theta, \Phi)$

$$\frac{\Delta T}{T}(\Theta, \Phi) = \sum_{lm} a_{lm} Y_{lm}(\Theta, \Phi). \quad (1.36)$$

The angular power spectrum is then given by the ensemble average of the coefficients a_{lm} , where the angular average corresponds to a value extracted from all $2l + 1$ m -modes for each l :

$$C_{T,l} \equiv \langle |a_{lm}|^2 \rangle. \quad (1.37)$$

The angular power spectrum fitted for the three-year WMAP observations can be seen in figure 1.11. Its main features are several peaks, called acoustic peaks. They were caused by tiny gravitational perturbations at temperatures where matter and radiation were still in equilibrium. These fluctuations influenced the density distribution of all matter components. As the cold Dark Matter, which makes up most of the matter density interacting gravitatively, was (and still is) non-relativistic, the main share of the gravitational fluctuation has stayed in its initial place. At that time the photons were still coupled with the proton-electron plasma, which can be described with a fluid model. As the perturbations are small in amplitude, they evolve in a linear fashion and their Fourier components can each be approximated by an harmonic oscillator. The perturbation is then passed through this fluid like a pressure wave in acoustics at the sound speed of the plasma and is therefore called acoustic oscillation. After the decoupling of the photons, the evolution of the spectrum is imprinted in their distribution. The maximum peak is given by the first density maximum, reached after $1/4$ of a period at the decoupling

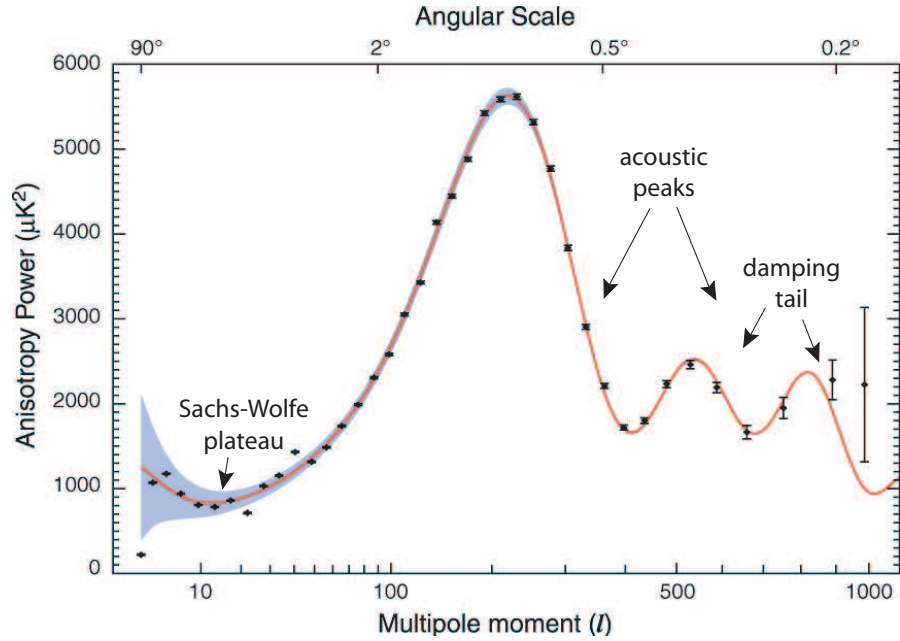


Figure 1.11: Angular power spectrum measured by the WMAP project. Figure for the three-year data, taken from reference [WMAP].

time. The additional peaks are all suppressed due to the 'Silk damping', which is caused by the non-instantaneous recombination. For a short time some interactions still take place between the photons and the protons and electrons, leading to a leveling-out of the distributions at small scales (large l), given by the sound horizon.

Until the decoupling, the perturbation can only travel a certain distance. On larger scales (small l) the anisotropies have not developed significantly, thus displaying their initial form. The perturbations measured here result from perturbations of the gravitational potential $\partial\phi$ and gravitational redshift. They can be described by

$$\frac{\partial T}{T} \simeq \frac{1}{3} \frac{\partial\phi}{c^2}. \quad (1.38)$$

Additional effects such as the filling of the troughs due to the Doppler effect, are well known. Thus, the physics of the angular power spectrum is understood and the distribution itself can be simulated accurately. Therefore, this data offers the possibility to derive cosmological parameters. Analysis of the WMAP data displays the best fit for a power-law flat Λ CDM model. A set of 6 parameters is needed for the fit and results in constraints given in table 1.1.

Neutrinos leave an imprint on the cosmic microwave background according to their mass. At the time of the perturbations the neutrinos are relativistic. They are 'free-streaming', meaning they seldom interact with particles (a detailed description of free-streaming can be found in the review [Les06]). Thus they carry their part $\Omega_\nu h^2$ from the initial perturbation to a minimum diffusion length $\lambda = \int_0^t v d\tau < \int_0^t c d\tau$. This length

Table 1.1: Best-fit parameters for the three-year WMAP data, taken from [Spe07].

parameter		best-fit value
matter energy density	$\Omega_m h^2$	$0.1277^{+0.0080}_{-0.0079}$
baryon energy density	$\Omega_b h^2$	0.02229 ± 0.00073
Hubble constant	h	$0.732^{+0.031}_{-0.032}$
scalar spectral index at 0.002 Mpc s^{-1}	n_s	0.958 ± 0.016
reionisation optical depth	τ	0.089 ± 0.030
linear theory amplitude of matter fluctuations on $8h^{-1} \text{ Mpc}$	σ_8	$0.761^{+0.049}_{-0.048}$

corresponds to a particular angle in the power spectrum. The neutrino can therefore lead to a damping (see figure 1.12 for a simulated example).

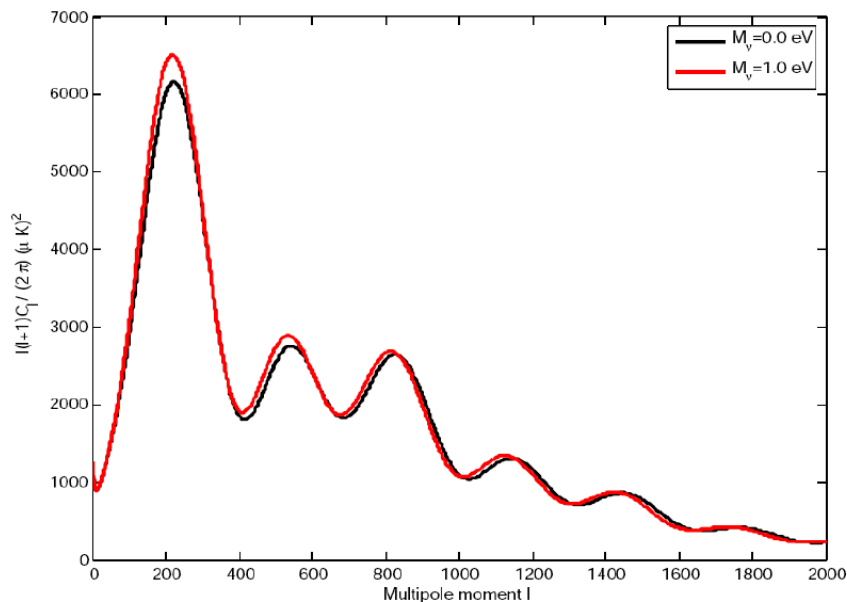


Figure 1.12: Angular power spectrum simulated for different neutrino masses, figure taken from [Kri07]

Using only the three-year WMAP data without any other assumptions, the sum of neutrino masses is bound to [Spe07]

$$\sum m_\nu < 1.8 \text{ eV}. \quad (1.39)$$

Using additional data from sky surveys (e.g. SDSS, 2dFGRS), the Lyman- α forest and Type Ia supernovae measurements the limit can be further constrained.

A problem with these analyses is the choice of data and priors, as there are slight inconsistencies between the sets. A discussion of oddities that occur when using different

Table 1.2: Constraints on the neutrino mass for different data sets, taken at 95% confidence level, taken from [Spe07].

data set	$\sum m_\nu$
WMAP	1.8 eV
WMAP + SDDS	1.3 eV
WMAP + 2dFGRS	0.88 eV
CMB + LSS + SN	0.66 eV

data sets is given in reference [Kri06]. Using only consistent data sets, a conservative, robust cosmological neutrino mass limit of

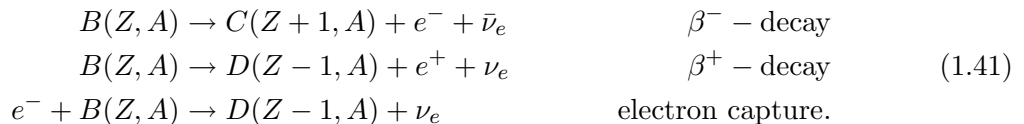
$$\sum m_\nu < 1.43 \text{ eV} \quad (1.40)$$

is derived by using only WMAP data in combination with the cluster mass function prior.

Studies, such as in reference [Kri06] show that cosmology gives bounds for the neutrino mass, but the analysis can be prone to systematic errors. Therefore it is important to measure such parameters using model independent methods. An example of this is the investigation of β -decay kinematics.

1.3 Measurements of β -decay kinematics

The term β -decay was first attributed to radioactive processes that emit an electron. It is extended now to all charged current reactions in which a nucleon is altered into a different nucleon.



As the decay is a 3-body process, the energy is distributed between the components. Therefore the emission spectrum is continuous. A typical spectral form can be seen in figure 1.14.

Due to energy conservation the total energy E_0 released in this decay needs to be to at least equal to the sum of the rest energies of the generated particles, thus introducing the step function

$$\Theta(E_0 - m_e c^2 - m_{\bar{\nu}_e} c^2) \quad (1.42)$$

into the spectrum. The transition probability T for the decay can be described with the help of Fermi's Golden Rule

$$T \propto |M|^2 \rho(E) \quad (1.43)$$

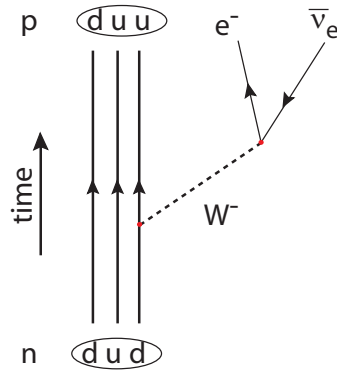


Figure 1.13: The neutron decay as an example for a β^- -decay

stating that the decay depends on the overlap between the initial and final state functions with perturbation H_{pert} . As the final state wave functions of the electron and the anti-neutrino can be considered constant, this is given by the nuclear matrix element $|M|^2 = \langle \phi_f | H_{pert} | \phi_i \rangle$. The transition probability also depends on the density of the available final states ρ available (for details of the derivation see reference [Fer34]). In detail the decay rate has the following dependency on the electron energy E [Alt03]:

$$\frac{d\dot{N}}{dE} = R(E) \sqrt{(E_0 - E)^2 - m_{\bar{\nu}_e}^2 c^4} \Theta(E_0 - E - m_{\bar{\nu}_e} c^2) \quad (1.44)$$

where $R(E)$ is the product of factors which are not relevant for the neutrino mass determination:

$$R(E) = \frac{G_F^2}{2\pi^3 \hbar^7} \cos^2 \theta_C |M|^2 F(Z + 1, E) p (E + m_e c^2) (E_0 - E). \quad (1.45)$$

with

- G_F the Fermi coupling constant
- θ_C the Cabibbo angle
- M the nuclear matrix element for the transition
- F the Fermi function that takes into account the Coulomb interaction between the emitted electron and the daughter nucleus
- p the electron momentum
- E the kinetic energy of the electron
- E_0 the endpoint energy of the β -spectrum
- $m_e c^2$ the rest energy of the electron
- $m_{\bar{\nu}_e} c^2$ the rest energy of the electron anti-neutrino

The dependence on the neutrino mass can be seen in equation (1.44). If the neutrino mass is not zero, the form of the spectrum and the endpoint position will be different. In the energy region with high count rates, the difference is hardly discernible. Close to the maximum energy E_0 the neutrino mass will be visible as a shift of the maximum energy and a slight change in the form of the spectrum. This is plotted schematically in figures 1.15.

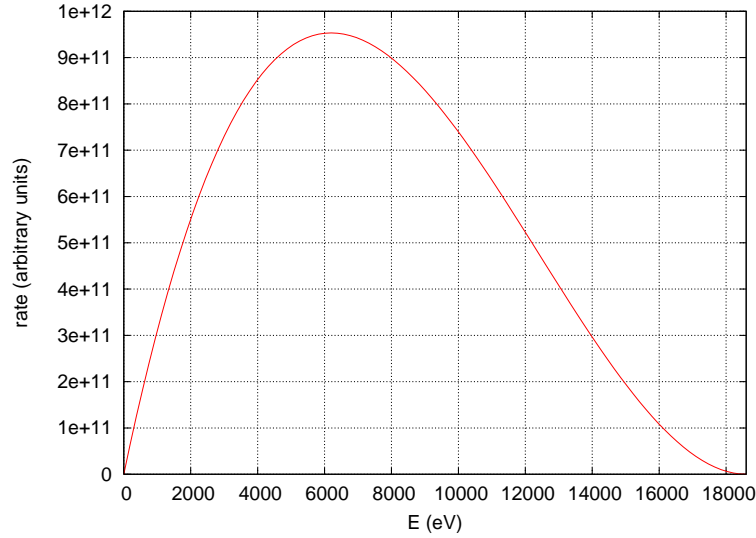


Figure 1.14: Schematic view of a β spectrum, neglecting the Fermi function

Taking into account the composition of the electron neutrino as a weighted superposition of states,

$$\nu_e = \sum_i U_{ei} \nu_i, \quad (1.46)$$

the decay spectrum should even incorporate the signatures of the different mass eigenstates:

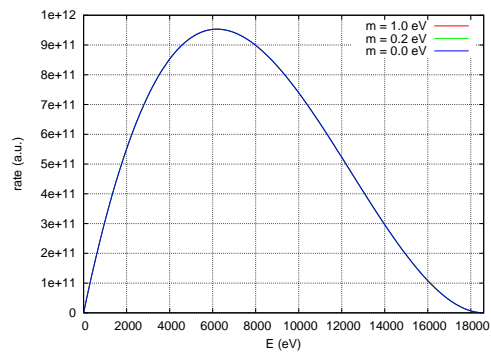
$$\frac{dN(E)}{dE} = R(E) \sum_i |U_{ei}|^2 \sqrt{(E_0 - E)^2 - m_i^2 c^4} \Theta(E_0 - E - m_i c^2). \quad (1.47)$$

Up to now these substructures cannot be resolved in current kinematic measurements, as the mass differences are tiny (see section 1.1.3), therefore only a weighted sum

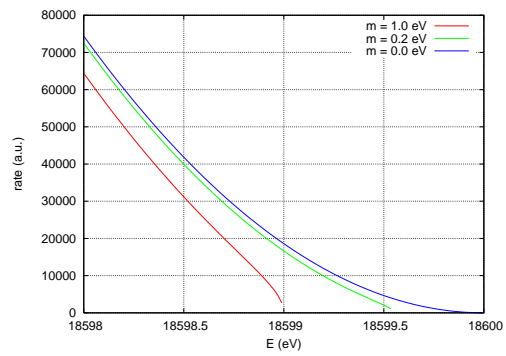
$$m_{\nu_e}^2 = \sum_{i=1}^3 |U_{ei}| m_i^2 \nu_i \quad (1.48)$$

is used as observable.

Most of the variables needed to describe the β -spectrum are known or can be measured with a certain accuracy. The fit function used to evaluate kinematic searches for the neutrino mass has to take into account the remaining unknown quantities, among those m_ν and the β -decay endpoint E_0 (which usually is not known with sufficient precision). The Karlsruhe Tritium Neutrino experiment (KATRIN) aims to measure the kinematics of the tritium β -decay with an integrating spectrometer. It is currently under construction at the Forschungszentrum Karlsruhe where measurements will start in 2010.



(a) Influence of different neutrino masses on a β -spectrum



(b) Influence of different neutrino masses close to the endpoint of the spectrum

Figure 1.15: Form of the β -spectrum for different neutrino masses

1.4 Outline

This diploma thesis gives an overview of simulations performed for the KATRIN collaboration in 2006/2007. The main concern lies on the design and technical realization of a wire electrode for the KATRIN main spectrometer with emphasis on the reduction of background effects.

After an introduction into neutrino physics in the first chapter, the next one explains the KATRIN experimental setup with special emphasis on the main spectrometer and its wire electrode. In the third chapter the simulation tools, which were used for this work, will be introduced. Design optimization simulations for the wire electrode will be described in the fourth chapter. The emphasis of the fifth chapter lies on simulations of an electron gun, a calibration source for the KATRIN pre-spectrometer with which different design properties can be tested. The sixth chapter gives an introduction into discharge effects and Penning traps and their impact on previous experiments, before discussing possible background sources in the KATRIN experiment. In the last chapter the simulations will be summarized and an outlook to further work will be given.

2 The KATRIN experiment

The KATRIN experiment aims to determine the mass of the electron anti-neutrino by ultra-precise measurements of tritium β - decay kinematics. With three years worth of data, the experiment has a discovery potential of 5σ (3σ) for a neutrino mass of $m_{\bar{\nu}_e} = 0.35 \text{ eV}/c^2$ ($m_{\bar{\nu}_e} = 0.30 \text{ eV}/c^2$) or can place an upper limit of $m_{\bar{\nu}_e} < 0.2 \text{ eV}/c^2$ at 90% C.L. [KAT04].

In this chapter the experiment is introduced. In the first section the choice of tritium as β -decay emitter is motivated. As the requirements on spectrometer properties for neutrino mass measurements are highly demanding, the KATRIN experiment uses a special type of spectrometer to allow the energy resolution needed, while at the same time fulfilling the demands of the acceptance angle and background. In the second section this spectrometer of type MAC-E filter is introduced. In the last section an overview of the remaining components of the setup is given.

2.1 The tritium β - decay

Any β -emitter could in principle be used for measuring the mass of the electron anti-neutrino. The KATRIN collaboration decided to utilise tritium ${}^3\text{H}$, as this isotope yields several advantages.

Endpoint energy Tritium is the β -emitter with the second lowest endpoint energy. The decay distribution described by equation (1.44) depends on the endpoint energy by $\frac{dN}{dE} \propto (E_0 - E)^2$. The fraction of β -decay electrons in the end-point region rises with $\frac{1}{E_0^3}$, therefore a low endpoint energy leads to a higher relative rate in the high energy tail where the effects of a non-zero neutrino mass are most pronounced.

As the energy is analysed electrostatically, a lower endpoint simplifies the experiment, as lower filter voltages can be applied.

The nuclear matrix element The decay ${}^3_1\text{H} \rightarrow {}^3_2\text{He} + e^- + \bar{\nu}_e$ is super-allowed as it is a transition between mirror nuclei. The matrix element is energy independent and has a rather large value.

Half life With a half life of 12.3 a, tritium is rather short living. This reduces the amount of source material needed to reach a sufficiently high count rate.

Electronic structure Being low Z nuclei, the electronic structure of tritium and its daughter ${}^3\text{He}^+$, as well as their molecular states as T_2 , THe^+ are relatively simple and

can be computed. A description of calculations for the final state distributions carried out recently can be found in reference [Dos06]. It emphasizes on the influence of parameters such as temperature and isotopic composition. The electronic structure has an impact on the β -spectrum and therefore is a parameter for the analysis.

Inelastic scattering As they are low Z nuclei, the fraction of decay electrons colliding inelastically with molecules in the source is small; 41.3 % reach the spectrometer without any scattering [KAT04]. In addition, the first inelastic scattering will be seen in the spectrum at an energy 12 eV lower than the endpoint due to the high excitation threshold of T_2 . It can easily be separated from the unscattered spectrum. With an energy resolution of 0.93 eV, a constant plateau with a width of ≈ 10 eV separates the onset of the transmission function and the rise in count rate due to scattering. A detailed discussion on this can be found in reference [Wol08].

The lowest energy endpoint of a β -decay was found with about 2.47 kV for ^{187}Rh . Cryo-bolometer measurements applying ^{187}Rh for neutrino mass determination yield a limit of $m_{\bar{\nu}_e} < 15 \text{ eV}/c^2$ [Sis04]. The Rhenium based successor experiment MARE aims for a sensitivity on the order of the current $m_{\bar{\nu}_e}$ -limits from Mainz and Troitsk within the next decade with the outlook of sub-eV/ c^2 sensitivity in the further future. The bolometric approach offers scalability and the possibility to reduce systematic errors, as the source and detector are not separated.

2.2 The MAC-E filter

At the highest β -energies close to the spectral end point, the count rate becomes very low (e.g. only $\approx 10^{-12} - 10^{-13}$ of all β -decays fall into a small interval of 1 eV below the endpoint of the Tritium spectrum). However most of the information on the neutrino mass is contained in this region just below E_0 (see equation (1.44)). For this reason, a spectrometer with a very large angular acceptance and an energy resolution of $\Delta E \approx 1$ eV at the endpoint energy $E_0 \approx 18600 \text{ V}$ of ^3H is needed. This can be fulfilled with a spectrometer working with the principle of magnetic adiabatic collimation, analysing the energy with an electrostatic filter (short: MAC-E filter) [Pic90, Pic92].

2.2.1 Basic principle

A schematic view of a MAC-E filter can be seen in figure 2.1. The basic principle of a MAC-E filter consists of the adiabatic guidance of electrons on cyclotron tracks along magnetic field lines. Decreasing slowly the strength of the magnetic field, the kinetic energy E_{kin} of the electrons stored in the transversal motion E_{\perp} is transformed into longitudinal energy E_{\parallel} . At the position of the minimal magnetic field B_{min} an electric

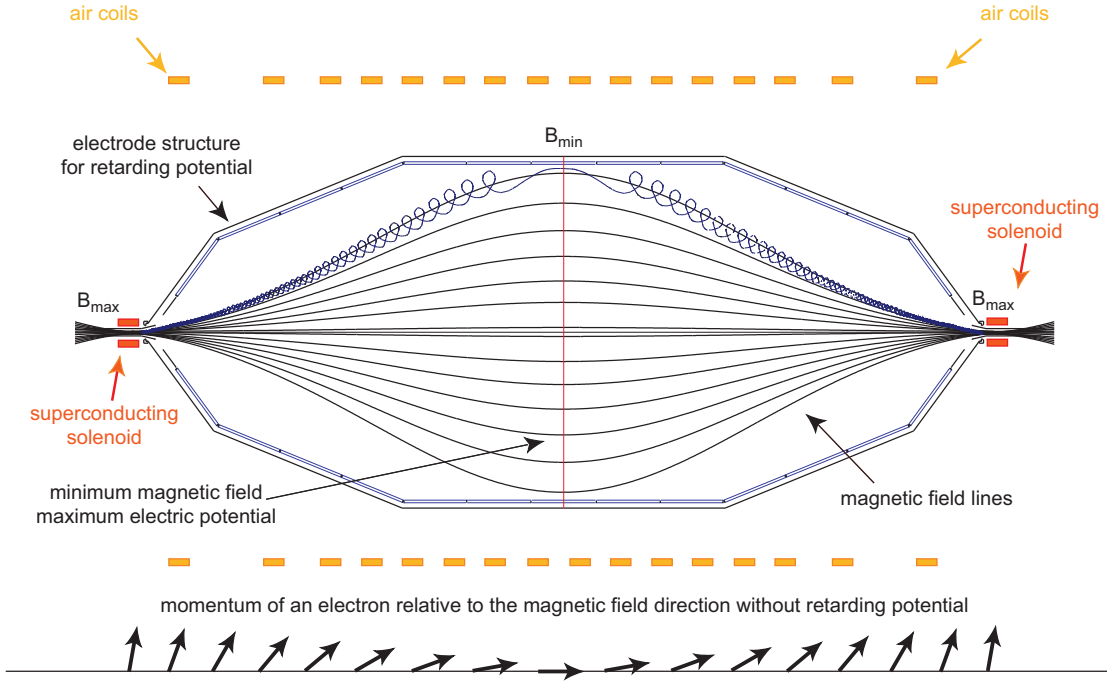


Figure 2.1: Schematic drawing of the KATRIN main spectrometer as an example for a MAC-E filter. An exaggerated cyclotron motion of an electron is shown in blue. The arrows at the bottom of the figure give the relative momentum of an example electron.

retardation field U_0 is applied¹. Only electrons with longitudinal energies

$$E_{\parallel} > qU_0 \quad (2.1)$$

can cross the potential barrier. The spectrometer thus acts as a high-pass filter; only electrons with energies exceeding a certain value will reach the exit of the MAC-E filter and can be counted in a detector. The measured rate will then represent an integrated spectrum.

To measure a monoenergetic electron beam the acceleration voltage at the source or the retarding potential in the spectrometer have to be driven. The detected rate corresponds to the transmission function of the spectrometer. An example transmission function is shown in figure 2.2.

The transmission function is not a step function, as the spectrometer has a finite resolution. This is due to incomplete transformation of transversal energy into longitudinal

¹The plane on which the minimum magnetic field and maximum electric potential are applied is called analysing plane, as here the selection between passing and not passing takes place. In the KATRIN spectrometers, this plane is positioned in the symmetry plane. It is denoted as $z = 0$ m if each MAC-E filter is considered separately. In the KATRIN beamline setup used in the simulations within this thesis the analysing plane of the main spectrometer is defined as $z = 0$ m. The analysing plane of the pre-spectrometer therefore has the position $z = -14.3$ m.

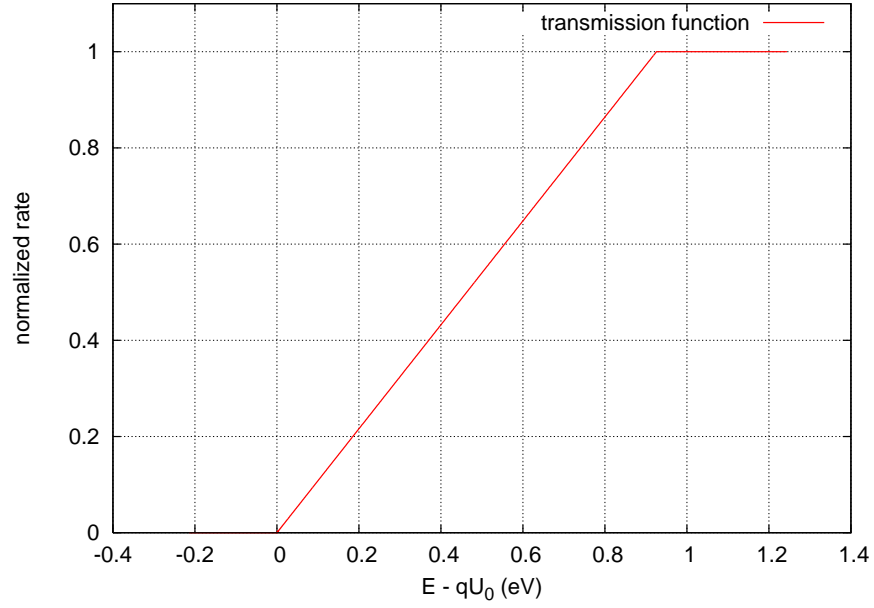


Figure 2.2: Theoretical transmission function for MAC-E filter with pinch magnet

energy. Therefore, electrons can be reflected even though their total kinetic energy E_{kin} exceeds the potential barrier qU_0 . In order to derive an expression for the energy resolution, the basic relations in a MAC-E filter need to be explained.

The kinetic energy of the electrons guided around the magnetic field lines can be divided into a longitudinal component E_{\parallel} that is stored in the motion parallel to the magnetic field and a transversal component E_{\perp} due to the cyclotron motion around the magnetic field lines. E_{\parallel} and E_{\perp} are defined by the angle Θ between the momentum of the electron and the magnetic field \vec{B} (see figure 2.3).

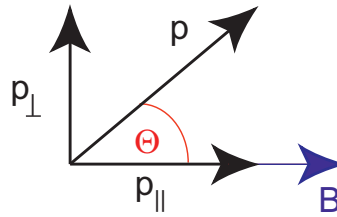


Figure 2.3: Definition of the angle Θ

As the kinetic energy is, in non-relativistic approximation, equal to $E_{kin} = \frac{p^2}{2m}$ the basic relations below are valid:

$$\begin{aligned}
E_{kin} &= E_{\parallel} + E_{\perp} \\
E_{\perp} &= E_{kin} \sin^2 \Theta \\
E_{\parallel} &= E_{kin} \cos^2 \Theta.
\end{aligned} \tag{2.2}$$

If the magnetic field and the electric potential changes only slightly over the cyclotron periods of an electron motion, the motion is adiabatic. This means that the motion is able to adjust to changes in the magnetic field by resizing the radius of the cyclotron motion, thus conserving the magnetic flux $\Phi = \int B dA$ enclosed by the gyrating trajectory. This can be expressed in terms of the adiabatic invariant

$$Br_c^2 = const. \tag{2.3}$$

An equivalent formulation is the conservation of the product of the absolute value of the magnetic moment $|\vec{\mu}|$ and the Lorentz-factor $\gamma = \frac{1}{\sqrt{1-\frac{v^2}{c^2}}}$

$$\gamma\mu = const. \tag{2.4}$$

As the maximum γ factor reached by electrons in the tritium decay is 1.04, one finds that to good approximation the magnetic moment itself is conserved

$$\mu = \frac{E_{\perp}}{B} = const. \tag{2.5}$$

This relation is useful to derive an expression for the energy resolution ΔE of the MAC-E filter. If in the maximum magnetic field B_{max} at the entrance of the spectrometer the maximum energy $E_{kin,max}$ is stored in the perpendicular component E_{\perp} , the amount of the energy still remaining in the cyclotron motion ΔE_{\perp} at the minimal magnetic field can be determined by the relation

$$\frac{E_{kin,max}}{B_{max}} = \frac{\Delta E_{\perp}}{B_{min}}. \tag{2.6}$$

As ΔE_{\perp} is not transformed into longitudinal energy, it cannot be analysed. The maximum magnetic field strength in the KATRIN main spectrometer is $B_{max} = 6 \text{ T}$ at the exit of the spectrometer and decreases to a minimum value of $B_{min} = 3 \text{ G} = 3 \cdot 10^{-4} \text{ T}$. The endpoint of ${}^3\text{H}$ lies at approximately $E_0 = 18600 \text{ V}$. This gives rise to a resolution of

$$\Delta E = \frac{B_{min}}{B_{max}} E_0 = \frac{1}{20000} 18600 \text{ V} = 0.93 \text{ eV}. \tag{2.7}$$

If at the entrance of the spectrometer all energy is stored in the perpendicular component E_{\perp} , the angle between the momentum of the electron and the magnetic field is $\Theta = 90^\circ$. The energy is transformed into longitudinal energy, at the same time the electric field

reduces the longitudinal energy. Therefore the angular distribution in the analysing plane contains all angles.

The MAC-E filter analyses all electrons that enter the spectrometer. This means that all electrons that have forward momentum ($\Theta_{start} < 90^\circ$, with *start* describing the conditions at the entrance of the MAC-E filter) at the entrance magnet will be analysed. The initial energy component perpendicular to the magnetic field $E_{\perp,start}$, which can be expressed in terms of the initial angle Θ_{start} between magnetic field and the momentum of the electrons, determines the retardation potential U_0 at which it will pass the filter:

$$\begin{aligned}
 E_{\parallel,Bmin} &> 0 & (2.8) \\
 E_{\parallel,Bmin} &= E_{kin,Bmin} - E_{\perp,Bmin} \\
 &= E_{kin,Bmin} - E_{\perp,Bstart} \frac{B_{min}}{B_{start}} \\
 &= E_{kin,Bstart} - qU_0 - E_{kin} \sin^2 \Theta_{start} \frac{B_{min}}{B_{start}} \\
 \Rightarrow qU_0 &< E_{kin,Bstart} \left(1 - \sin^2 \Theta_{start} \frac{B_{min}}{B_{start}} \right). & (2.9)
 \end{aligned}$$

The index *min* describes the conditions in the analysing plane. This relation can be translated into a transmission condition for all angles:

$$\Theta \leq \Theta_{start} = \arcsin \sqrt{\frac{E_{kin} - qU_0}{E_{kin}} \frac{B_{start}}{B_{min}}}. \quad (2.10)$$

Only electrons emitted in the cone defined by the angle Θ_{start} can pass the filter. The fraction of electrons passing the filter in comparison to the maximum number possible gives the transmission function. The relation between the solid angle $\Delta\Omega$ which can be obtained using equation (2.10) and the maximum accepted solid angle 2π (all particles emitted in forward direction are analysed) is

$$\frac{\Delta\Omega}{2\pi} = 1 - \cos \Theta. \quad (2.11)$$

Together with equation (2.10), this results in the transmission function $T(E_{kin}, U_0)$ of

$$T(E_{kin}, U_0) = \begin{cases} 0 & E_{kin} < qU_0 \\ 1 - \sqrt{1 - \frac{E_{kin} - qU_0}{E_{kin}} \frac{B_{start}}{B_{min}}} & \text{for } qU_0 \leq E_{kin} \leq \frac{qU_0}{1 - \frac{B_{min}}{B_{start}}} \\ 1 & \frac{qU_0}{1 - \frac{B_{min}}{B_{start}}} \leq E_{kin} \end{cases} \quad (2.12)$$

Using a monoenergetic electron source with $E_{kin} = \text{const}$ to measure the transmission function, either the retarding potential U_0 has to be driven or an additional potential which can be changed has to be applied to the source. The width of the transmission function is given by the magnetic field ratios. If a source with an energy distribution is used, the width increases. The transmission function has to be convolved with the distribution.

As the starting solenoid in the source of the KATRIN experiment is not providing the maximum field in the setup, the magnetic mirror effect has to be taken into account. If a particle is guided from a lower magnetic field into a region with higher field strength, those with angles exceeding a critical value

$$\Theta_{max} = \arcsin \sqrt{\frac{B_{start}}{B_{max}}} \quad (2.13)$$

given by the ratio of the starting and maximum magnetic fields are reflected. Taking this into account, a modified transmission function can be derived

$$T(E_{kin}, U_0) = \begin{cases} 0 & E_{kin} < qU_0 \\ \frac{1 - \sqrt{1 - \frac{E_{kin} - qU_0}{E_{kin}} \frac{B_{start}}{B_{min}}}}{1 - \sqrt{1 - \frac{B_{start}}{B_{max}}}} & \text{for } qU_0 \leq E_{kin} \leq qU_0 \frac{B_{max}}{B_{max} - B_{min}} \\ 1 & qU_0 \frac{B_{max}}{B_{max} - B_{min}} \leq E_{kin} \end{cases} \quad (2.14)$$

In a real measurement the transmission function has to be corrected for several experimental deviations from an ideal setup.

2.2.2 MAC-E filters in the KATRIN setup

The main spectrometer

The measuring tool of the KATRIN experiment is the main spectrometer. To achieve a resolution of $\frac{\Delta E}{E_{max}} = \frac{1}{20000}$, the magnetic field has to be reduced from the entrance to the analysing plane by four orders of magnitude. At the minimum of the magnetic field of 3 G the reference flux tube of 191 Tcm² will have a radius of 4.5 m. The outer hull of the vacuum vessel has a radius of 4.9 m. Detailed studies investigating the transmission, adiabatic energy transformation and field homogeneity were conducted in [Val04]. It was decided to build a spectrometer with a length of ca. 23 m. The vessel itself will be elevated to potential, thus not requiring an inner electrode system as it was used in predecessor experiments (see section 6.2.1 and 6.2.2 for details). Due to other reasons discussed in section 2.2.4, an electrode system will still be inserted into the spectrometer. The magnetic field at the entrance and the exit of the main spectrometer will be generated by two superconducting magnets, providing a maximum field of 4.5 T and 6 T respectively. To reduce the asymmetry of the flux tube as well as to correct for the influence of the terrestrial magnetic field, air coils are constructed around the spectrometer (see also figure 2.7).

The pre-spectrometer

Predecessor experiments have shown that ionisation of residual gas molecules and traps for charged particles inside the MAC-E filter lead to an increased background (see also chapter 6). To prevent this, an additional MAC-E filter is used to reflect all electrons with energies below $\approx E_0 - 300$ eV back into the source section. Thus only $\approx 10^4$ of

initially 10^{10} decay electrons enter the main spectrometer per second. As it works far below the interesting endpoint of the tritium β - decay, the requirements on the energy resolution are not high ($\Delta E \lesssim 100$ eV). The pre-spectrometer has a length of 3.4 m and a diameter of 1.7 m. It is already in operation at Forschungszentrum Karlsruhe for test measurements (see also chapter 6).

The monitor spectrometer

An additional MAC-E filter will be installed outside the beam line of the KATRIN experiment. It will be used for real-time calibration measurements. As the retarding potential applied to the main spectrometer electrode system will not be constant on the required sub-ppm level, it needs to be monitored. Therefore, the HV will be divided down to a level of 10 V for which precision measurement tools are available and stored for the data analysis. An ultraprecision voltage divider has been built for this purpose. As the divider has a long-term drift, this is monitored and recorded. Simultaneous measurements with electron sources based on atomic and nuclear standard will be conducted with an additional MAC-E filter, the so-called monitor spectrometer. The same retarding potential that is used for the main spectrometer and controlled with the voltage divider will be applied to this spectrometer.

The MAC-E filter used in the Mainz neutrino mass experiment (see also section 6.2.2) will be transported to Karlsruhe and used for this purpose.

For detailed informations on calibration and monitoring see references [Tüm07, Ost08].

2.2.3 Characteristics of a MAC-E filter

In this section several important properties of MAC-E filters are discussed with respect to the way they can be seen in simulations and how they influence the measurements. In addition to its basic properties such as the energy resolution, deviations from the ideal MAC-E filter are mentioned.

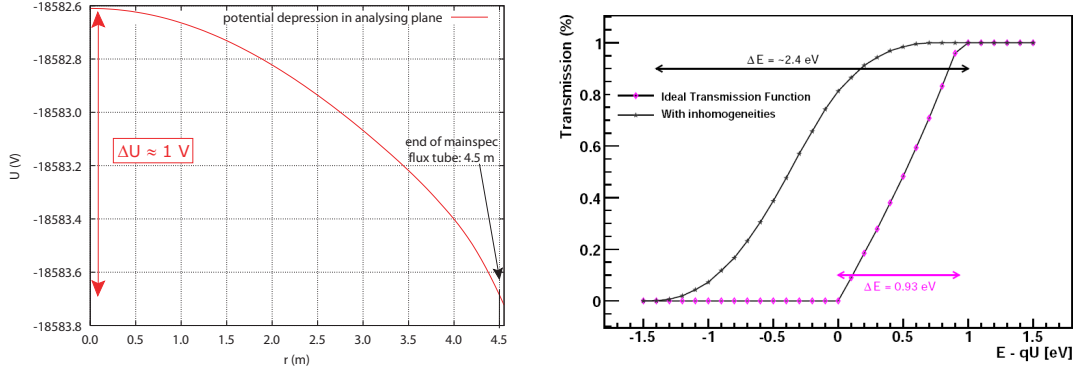
- Energy resolution

The energy resolution is an essential property of the MAC-E filter. It is defined in equation (2.6). The main spectrometer has an energy resolution of 0.93 eV for electrons with $E = 18.6$ keV. The pre-spectrometer has a relative energy resolution of $\frac{\Delta E}{E} \approx \frac{200}{45000}$, which would lead to $\Delta E \approx 83$ eV for $E = 18.6$ keV.

- Potential depression

As the spectrometers have relatively large diameters in the analysing plane, the potential across these planes is not constant. The deviation from a homogeneous potential is called *potential depression*. The potential depression in the analysing plane for the KATRIN main spectrometer can be seen in figure 2.4a. Therefore the transmission condition of an electron depends on its starting radius. To be able to take this into account in the analysis, the detector has to record the radial position of the transmitted electron. If this is not done, the transmission function broadens (see figure 2.4b). Therefore the area of the detector will be segmented (see figure

2.9). The mean values of the retardation potential have to be measured for each radial detector segment with a calibration electron source (see also chapter 5). As a large potential depression gives rise to higher inaccuracies in the retarding potential, the value should be as small as possible. For the main spectrometer without wire electrode, a potential depression of 0.5 V for a radius of 4.5 m was possible [Val04]. Implementing wires and their holding structure increases this to values of ≈ 1.4 V (see also chapter 4 and section 6.5). In comparison the potential depression of the pre-spectrometer according to simulations amounts to $\Delta U \approx 20$ V on a radius of 0.62 m².



(a) Potential depression in the analysing plane of the main spectrometer

(b) Results of a MC simulation including potential and magnetic field inhomogeneities $\Delta U \approx 1.2$ V and $\Delta B \approx 0.4$ G, figure taken from reference [Dun07]

Figure 2.4: The influence of field inhomogeneities on the transmission function

- Magnetic field depression

Also the magnetic field cannot be kept entirely homogeneous in the analysing plane, resulting in a radial dependence of the energy resolution. In the main spectrometer the deviation has the relative strength of $\frac{\Delta B}{B} \approx 10\%$; for the pre-spectrometer the deviation amounts to $\frac{\Delta B}{B} \approx 25\%$.

- Transmission

The electrons need to be guided adiabatically through the spectrometer. In particular electrons following magnetic field lines at the border of the flux tube and starting with large angles $\Theta \lesssim \Theta_{max}$ (thus their E_{\perp} is large) will typically be most sensitive to critical transmission conditions. Therefore, thorough studies need to be carried out in order to verify transmission also for these special starting conditions.

²As the pump port and the holding structure of the inner electrode is not included in the simulations, the real value will deviate from the calculated one.

2.2.4 Background reduction for a MAC-E filter: The wire electrode

For the ultra-precise measurements that are aimed to be conducted with the KATRIN experiment, a background level of about 10 mHz is an essential prerequisite.

Possible background sources in a MAC-E filter are

- residual gas ionisation,
- particle trapping and
- electrons emitted from the vessel hull by radioactivity or incident cosmic muons.

Residual gas ionisation is suppressed by the low pressure of 10^{-11} mbar inside the spectrometer vessels. It is known from predecessor experiments that measurements were not possible if the pressure exceeded specific limits, as then discharges were started (see also chapter 6).

Particle traps could exist inside the KATRIN MAC-E filters. They are discussed in detail in chapter 6. A possibility to empty a particle trap is to apply a dipole electric potential to the electrode. Previously stable trajectories become unstable due to an $\vec{E} \times \vec{B}$ drift motion. For detailed information see reference [Mue02].

A large fraction of the electrons emitted from the spectrometer hull do not reach the detector, since first of all no magnetic field lines connect electrode surfaces on high potential with the detector.

Electrons can reach the flux tube if the magnetic or electric field has a non-axial symmetric component [Glu05]. The resulting magnetron drift can lead the electrons to the flux tube, where they then are accelerated and reach the detector or become stored inside the sensitive volume and cause scattering, thus leading to increased background. Therefore, electrons from the vessel hull have to be prevented from reaching the flux tube.

A possibility to prevent electrons from the vessel hull from entering the spectrometer is to install a quasi-massless wire electrode a small distance from the surface. Applying a slightly more negative potential to it reflects electrons back into the vessel hull. This principle is illustrated in figure 2.5.

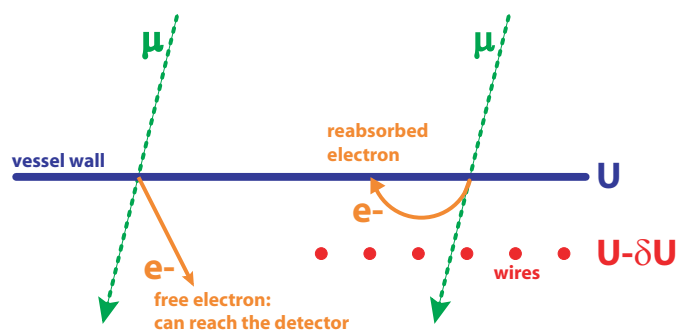


Figure 2.5: Illustration of the wire electrode principle

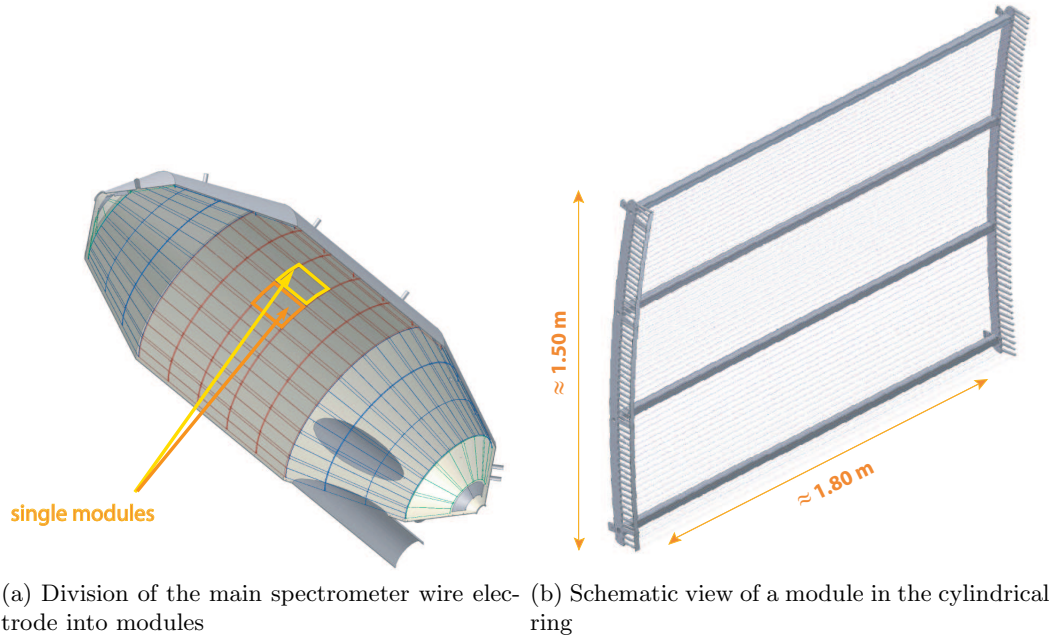


Figure 2.6: Modular design of the KATRIN main spectrometer wire electrode

The electric screening quality of a wire electrode is given by the screening factor S :

$$S = 1 + \frac{2\pi l}{s \ln \frac{s}{\pi d}}, \quad (2.15)$$

with s the distance between the wires, l the distance from the wire layer to the vessel hull and d the wire diameter. Larger wire diameters increase the screening factor, if the other parameters are kept constant. On the other hand the wires should not introduce additional background, their diameter needs to be kept small. Therefore, a double layer electrode has been designed with larger wire diameter wires in the outer layer, shielding the vessel hull. A second layer with a smaller wire diameter is used to shield the first layer and most of the massive mounting structure. For further details discussing the properties of a screening electrode see reference [Val04]. The parameters chosen for the main spectrometer wire electrode can be seen in table 2.1.

Table 2.1: Parameters of the KATRIN main spectrometer wire electrode

	diameter d	distance l	potential difference ΔU	
outer layer	0.3 mm	150 mm	-100 V	rel. to vessel
inner layer	0.2 mm	220 mm	-200 V	rel. to vessel
		70 mm	-100 V	rel. to outer layer

The wires inside the spectrometer are arranged in the form of a large number of modules

(see figure 2.6).

Tests with the improved Mainz setup have demonstrated the effectiveness of a wire electrode to screen background [Fla04, Mue02].

Several details of the wire electrode setup are also discussed in chapter 4.

2.3 Setup of the KATRIN experiment

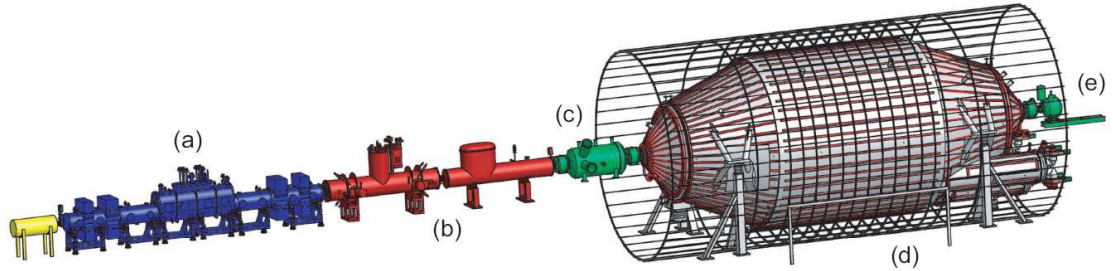


Figure 2.7: The KATRIN setup (without monitor spectrometer): a) WGTS, b) transport section, c) pre-spectrometer, d) main spectrometer with air coil system and e) detector section

The KATRIN setup consists of several parts which are shown in figure 2.7.

The WGTS The β -electrons will be supplied by a windowless gaseous tritium source (short: WGTS). Molecular tritium gas will be injected in the middle of the 10 m long source section and diffuses towards both ends (see also figure 2.8 for a source density profile). The decay tube has a diameter of 0.09 m. The column density inside the source section is optimized with regard to both luminosity and scattering on residual gases.

At both ends turbo molecular pumps reduce the tritium density. The gaseous tritium will then be purified and reinjected into the circuit.

The decay electrons are guided by a strong magnetic field (3.6 T) towards the spectrometer section.

The transport section To reduce background effects, it is essential that no tritium reaches the spectrometer section. Therefore a differential pumping section is needed in which the gas flow is reduced by a factor of 10^{11} . To achieve this, two different sections are deployed: The differential pumping section (DPS) that reduces the tritium flow with turbomolecular pumps and the cryogenic pumping section (CPS), in which the residual tritium will be frozen onto the cold surface covered with argon frost. Several bends are introduced in the transport beam line to allow to pump molecules more efficiently, while the decay electrons are guided by a 5.6 T magnetic field adiabatically towards the spectrometer section.

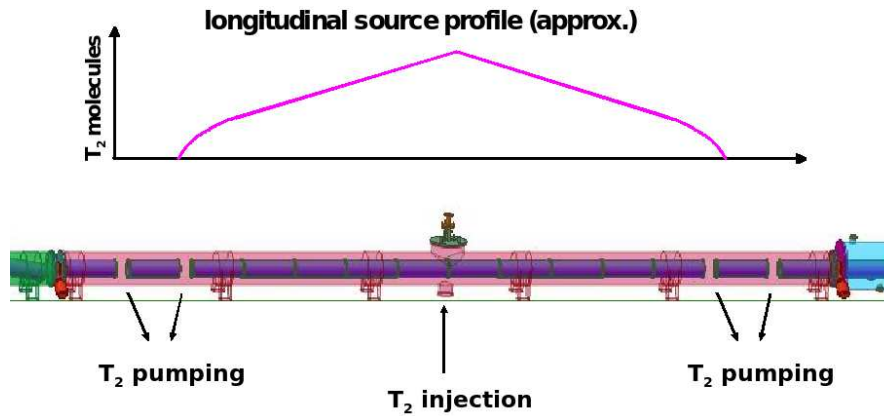


Figure 2.8: Schematic view of the WGTS and the gaseous T_2 density profile

The detector The energy analysis of the β -decay electrons is done by the KATRIN main spectrometer. Therefore the detector *only* needs to count the electrons passing the filter. A relatively good energy resolution is still necessary, as this would help to discern signal from background. Therefore, an energy resolution of about 600 eV is targeted for electron energies of 18600 eV. The detector will be a silicium semiconductor detector. Background requirements on the detector call for an active and passive shielding. The detector needs to be very sensitive to low electron rates, but also needs to be able to cope with high rates from calibration sources as well.

A very important requirement on the detector has already been mentioned in section 2.2.3: The detector has to be segmented to take into account the potential depression in the analysing plane. It is subdivided into radial segments. The sizes of the segments are adjusted so that each element has the same size. For an illustration see figure 2.9.

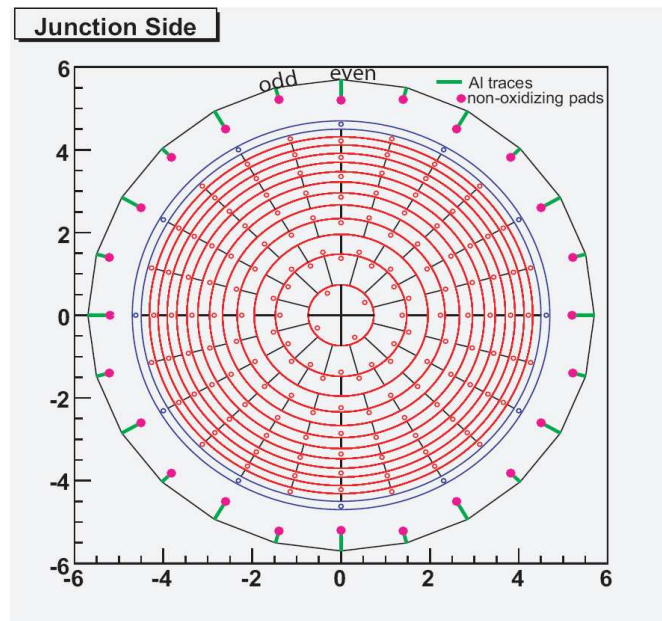


Figure 2.9: Segmentation of detector area, figure taken from reference [Ste07]

3 Simulation tools

This diploma project deals with electromagnetic design simulations for the KATRIN experiment. The computer code used for the simulations was made available mainly by Dr. Ferenc Glück (Forschungszentrum Karlsruhe) and was processed and maintained by Sebastian Vöcking (for detailed information on the C-Code see also [Voe08]).

As the KATRIN experiment implements static electric and magnetic fields, the configurations can be calculated separately, because they are decoupled. Therefore, separate tools are used for the electric and magnetic field simulations. The results are needed as input for trajectory calculations of electrons and stored charged particles, and for the search for particle traps.

In general, the programs work with variables of the double type. Therefore accuracy and comparison computations are done to double accuracy.

3.1 Magnetic field calculations

In the KATRIN experiment the magnetic fields are generated by inductor coils. To calculate a magnetic field, Biot-Savart's law (see eq. 3.1 and figure 3.1) can be employed:

$$d\vec{B} = \frac{\mu_0}{4\pi} \frac{I d\vec{l} \times \hat{r}}{r^2}. \quad (3.1)$$

$d\vec{B}$ is the magnetic field induced from an infinitesimal conductor segment with current I on a field point, $d\vec{l}$ an infinitesimal segment of the conductor in direction of the current, \hat{r} the unit vector in direction of the field point and r the distance between the infinitesimal segment and the field point.

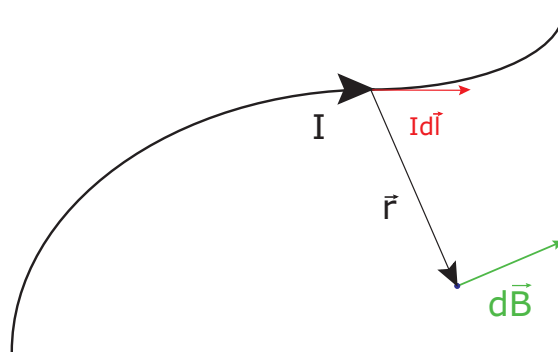


Figure 3.1: Illustration of Biot-Savart's law

Working with coils with one symmetry axis, it is sufficient to characterise them by their profile in the positive r - z plane. The complete body will then be obtained by rotation. For thin coil wire dimensions equation (3.1) can be expressed in terms of the complete elliptic integrals (I) - (III)

$$\begin{aligned}
 (I) \quad K(k) &= \int_0^{\pi/2} \frac{d\phi}{\sqrt{1-k^2 \sin^2 \phi}} \\
 (II) \quad E(k) &= \int_0^{\pi/2} d\phi \sqrt{1-k^2 \sin^2 \phi} \\
 (III) \quad \Pi(c, k) &= \int_0^{\pi/2} \frac{d\phi}{(1-c^2 \sin^2 \phi) \sqrt{1-k^2 \sin^2 \phi}}
 \end{aligned} \tag{3.2}$$

thus making a completely analytical computation possible (see for example [Lan67]):

$$B_r = \frac{I}{c} \frac{2z}{r \sqrt{(a+r)^2 + z^2}} \left[-K(k) + \frac{a^2 + r^2 + z^2}{(a+r)^2 + z^2} E(k) \right] \tag{3.3}$$

$$B_\phi = 0 \tag{3.4}$$

$$B_z = \frac{I}{c} \frac{2}{\sqrt{(a+r)^2 + z^2}} \left[K(k) + \frac{a^2 - r^2 - z^2}{(a+r)^2 + z^2} E(k) \right], \tag{3.5}$$

with B_r , B_ϕ and B_z the magnetic field strength in polar coordinates, see fig. 3.2 and $k^2 = \frac{4ar}{(a+r)^2 + z^2}$. If an infinitely thin solenoid is used, also the third elliptic integral is needed.

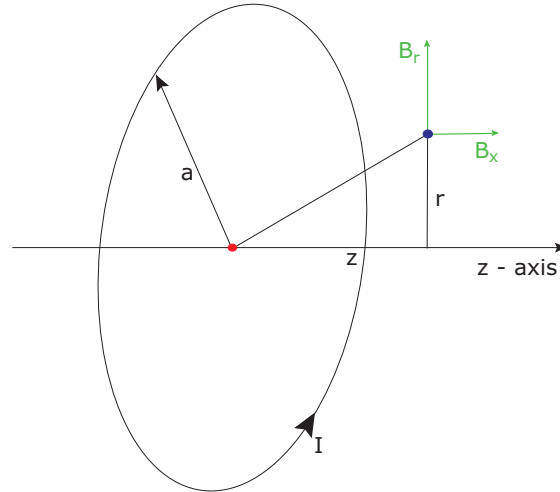


Figure 3.2: Magnetic field B induced by current I running through a loop with radius a

In reality the wire thickness cannot be neglected. Therefore a numerical integration in the radial direction is necessary.

With elliptic integrals, the magnetic field can be calculated for all field points, including the wire wound coil body. They have also the advantage of high precision and can be used for every field point, but their calculation is rather time consuming¹. Therefore, a more approximative approach via Legendre polynomial expansion is generally used to calculate the magnetic fields.

At a point $\vec{P} = (r, 0, z)$ close to the symmetry axis of the coils, the magnetic field can be expressed in terms of its derivatives in the point z_0 on the symmetry axis (called source point) with respect to z (B_n^{cen} , also called source coefficient) and the Legendre polynomials $P_n(u)$:

$$B_r = -s \sum_{n=1}^{\infty} \frac{B_n^{cen}}{n+1} \left(\frac{\rho}{\rho_{cen}} \right)^n P_n'(u), \quad (3.6)$$

$$B_\phi = 0 \text{ and} \quad (3.7)$$

$$B_z = \sum_{n=0}^{\infty} B_n^{cen} \left(\frac{\rho}{\rho_{cen}} \right)^n P_n(u). \quad (3.8)$$

Here, ρ_{cen} is the central convergence radius with respect to the source point z_0 , ρ the distance between the field point \vec{P} and the source point z_0 and $u = \cos \theta = \frac{z-z_0}{\rho}$. This series only converges if the point P lies inside the area of the central convergence circle of radius ρ_{cen} around the source point z_0 , which is given by the distance to the closest coil (see figure 3.3).

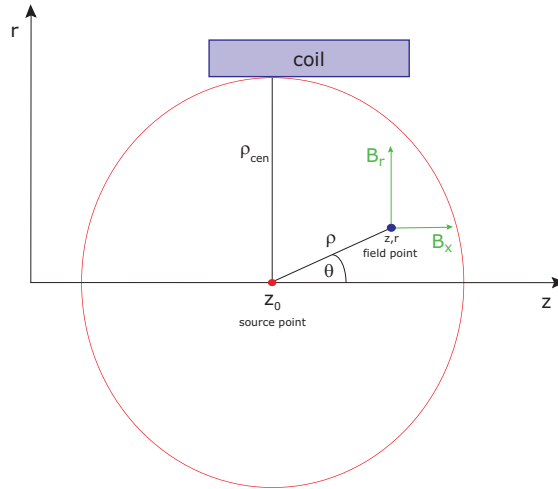


Figure 3.3: The central convergence circle

If more complicated setups with more coils are computed, the convergence radius is determined by the closest coil (see figure 3.4).

¹For a one-coil system the computation of the magnetic field in an arbitrary field point with the elliptic integral method for a computer with a multiplication time of approximately 10 ns takes about 2 ms [Glu06a]

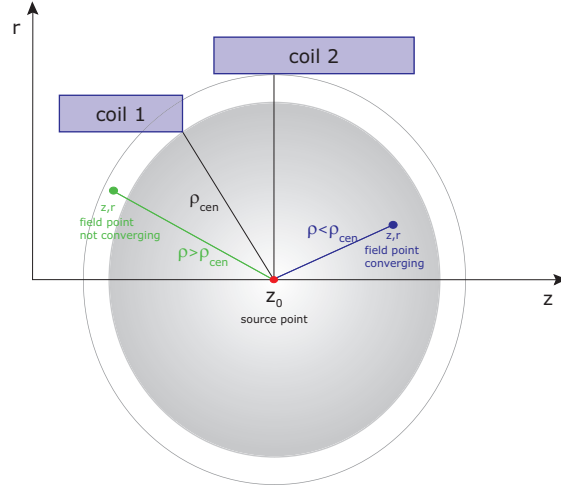


Figure 3.4: Convergence radius for a two-coil system

More source points can be used to cover a larger area, as demonstrated in figure 3.5.

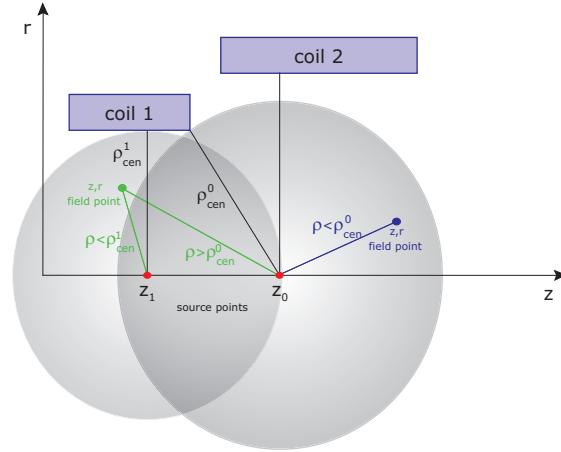


Figure 3.5: Using more source points leads to a better coverage of the area

The Legendre polynomial expansion converges faster if the coefficient $\frac{\rho}{\rho_{cen}}$ is small and the series needs only few terms. If the coefficient is large, more terms are needed for accurate results (see table 3.1). Thus computation time can be saved by searching the source coefficient with the best $\frac{\rho}{\rho_{cen}}$ ratio.

Table 3.1 shows that, for a small ρ/ρ_{cen} ratio, the Legendre polynomial expansion is about 10^3 times faster than the magnetic field computation by elliptic integrals. Even for a ratio of 0.93 one obtains a factor of 10 in time saving. Thorough testing showed that the Legendre polynomial expansion is preferable up to a ρ/ρ_{cen} ratio of 0.99 to the elliptic integrals.

The source coefficients B_n^{cen} can be expressed in two-dimensional integrals over the coil

Table 3.1: Number of terms n_{min} needed to achieve double precision accuracy for a given ρ/ρ_{cen} ratio and the computation time for a computer with approximately 10 ns multiplication time, taken from [Glu06a]

ρ/ρ_{cen}	n_{min}	time t [μs]
0.03	15	5
0.50	42	15
0.83	140	45
0.93	350	110

profile:

$$B_n^{cen} = \int_{R \in \text{coil body}} dR \int_{Z \in \text{coil body}} dZ b_n(Z, R) \quad (3.9)$$

with

$$b_n(Z, R) = \frac{\mu_0 I}{2\rho_{cen} A} \left(1 - \left(\frac{Z - z_0}{\rho_{ZR}} \right)^2 \right) \left(\frac{\rho_{cen}}{\rho_{ZR}} \right)^{n+1} P'_{n+1} \left(\frac{Z - z_0}{\rho_{ZR}} \right),$$

$\frac{I}{A}$ being the current density running through the coil and ρ_{ZR} the distance between the source point z_0 and the point (Z, R) in the coil body ($\rho_{ZR} = \sqrt{(Z - z_0)^2 + R^2}$).

3.1.1 magfield2

The program magfield2 calculates the magnetic field for a coil configuration with only one common symmetry axis (convention: the z-axis). For the calculation it needs the following parameters:

Ncoil

```
z_mid[1]    r_in[1]    d[1]    L[1]    I[1]
⋮          ⋮          ⋮          ⋮          ⋮
```

```
z_mid[Ncoil] r_in[Ncoil] d[Ncoil] L[Ncoil] I[Ncoil]
```

which are imported from the file `inputcoil.dat`.

Ncoil represents the total number of coils, z_{mid} the central z value of the coil, r_{in} the inner radius of the coil, d its thickness, L its length and I the current running through one wire multiplied with the number of windings (see figure 3.6).

Launching the program `magmain.c` by

```
./magmain -d delz_0 -m z_min -M z_max inputcoil.dat
```

calculates the source points z_0 in the interval $[z_{min}, z_{max}]$ with the equidistant spacing $delz_0$ and the source coefficients B_n^{cen} and stores them in the file `magsource.dat`.

The magnetic field for the field point (r, z) is then calculated by calling the routine `magfield2(z,r,inputcoil,n,&A,&Bz,&Br)` with the output variables A , Bz and Br .

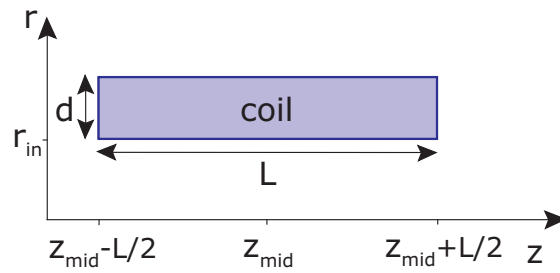


Figure 3.6: Input parameters for the magfield2 program

The parameter n and the coil geometry file (stored in the variable `inputcoil`) are passed in case the ρ/ρ_{cen} ratio exceeds 0.99. Then the magnetic field will be calculated with the elliptic integral computation.

3.1.2 magfield3

In contrast to magfield2, magfield3 is capable of calculating magnetic fields for a coil system with different axial symmetry axes. A global symmetry axis is defined for $r = 0$ and additional axes have to be described by two points on them.

In addition to the elliptic integrals and the Legendre polynomial expansion for field points close to the symmetry axis which were already implemented in magfield2, magfield3 also uses the Legendre polynomial expansion for field points far away from the symmetry axis (see figure 3.7).

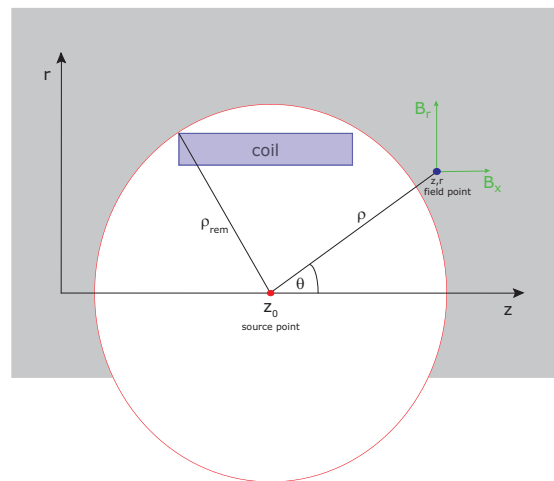


Figure 3.7: Illustration of the remote source point

For the remote field points the magnetic field is given by:

$$B_r = \sum_{n=2}^{\infty} \frac{B_n^{rem}}{n} \left(\frac{\rho_{rem}}{\rho} \right)^{n+1} P'_n(u), \quad (3.10)$$

$$B_\phi = 0 \text{ and} \quad (3.11)$$

$$B_z = \sum_{n=2}^{\infty} B_n^{rem} \left(\frac{\rho_{rem}}{\rho} \right)^{n+1} P_n(u). \quad (3.12)$$

The source points can be computed by 2-dimensional integrals over the coil profile:

$$B_n^{rem} = \int_{R \in \text{coil body}} dR \int_{Z \in \text{coil body}} dZ b_n^*(Z, R), \quad (3.13)$$

with

$$b_n^*(Z, R) = \frac{\mu_0 I}{2\rho_{cen} A} \left(1 - \left(\frac{Z - z_0}{\rho_{ZR}} \right)^2 \right) \left(\frac{\rho_{cen}}{\rho_{ZR}} \right)^n P'_{n-1} \left(\frac{Z - z_0}{\rho_{ZR}} \right). \quad (3.14)$$

The expansion converges for $\frac{\rho_{rem}}{\rho} < 1$ and is faster if the fraction is small. If it is large, more expansion terms are needed.

For the calculation of the magnetic field, the central source points and their source coefficients are calculated and stored in the file `magsource_central.dat`. Then, the remote source points and source coefficients are computed and written into the file `magsource_remote.dat`. In the last step, the source points and coefficients for all coils with the global axis as symmetry axis are evaluated separately and stored into the file `magsource_axisymm.dat`. This calculation is not necessary, but offers the opportunity to save calculation time, because in the Legendre polynomial expansion these coils can be considered as one.

The input file should include information on the local symmetry axis (\vec{A} and \vec{B} , see figure 3.8) as well as the coil parameters R_{min} and R_{max} and the current density I of the coil given by the total current (current running through a winding times the number of windings) divided by the coil cross section.

```

Ncoil
I[1]      A[1][x]      A[1][y]      A[1][z]      B[1][x]
B[1][y]   B[1][z]      R_min[1]     R_max[1]     n[1]
:
I[Ncoil]  A[Ncoil][x]  A[Ncoil][y]  A[Ncoil][z]  B[Ncoil][x]  B[Ncoil][y]
B[Ncoil][z] R_min[Ncoil] R_max[Ncoil] n[Ncoil]

```

The last parameter in each line of the inputfile is for the numerical integration in the radial direction in the elliptic integral method. A value of 20 should be sufficient for

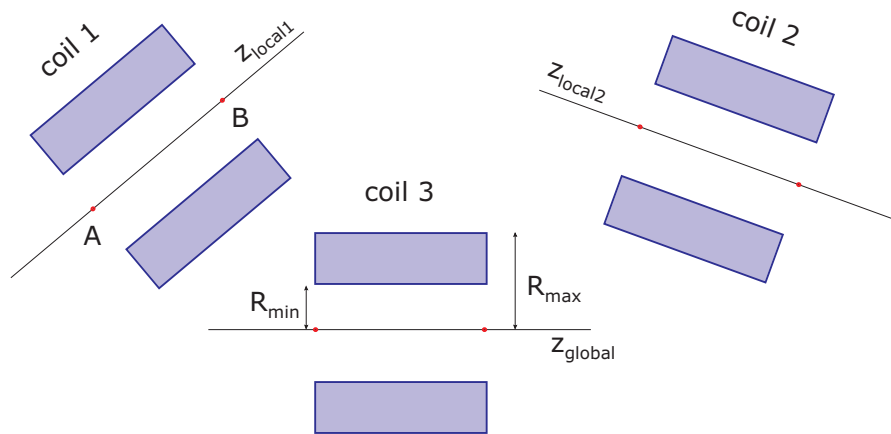


Figure 3.8: Input parameters for the magfield3 program

small coil thicknesses. This parameter can be increased to reach higher accuracy at the cost of a rise in computation time.

For the KATRIN experiment the magfield3 program is needed if the tilted coils of the transport section are included in the calculations (see figure 3.9a).

In design simulations for the main spectrometer it is sufficient to include only the main spectrometer and detector magnets as well as the air coils. For design simulations of the pre-spectrometer, additional coils of the CPS should be included. It is sufficient to approximate the tilted coils here with one coil on the symmetry axis, as the contributions of the stray fields are of the same order of magnitude.

3.1.3 Fieldlinepot

The program *fieldlinepot.c* was developed on the basis of the magnetic field calculations. It tracks magnetic field lines, giving out their coordinates and the electric potential for these coordinates. This is used for simulations looking for particle traps, which can be seen as potential hills or wells (see chapter 6).

A Runge-Kutta algorithm is used for tracking the magnetic field lines, using the equation

$$\frac{d}{dx}y_i(x) = f_i(y_1, \dots, y_n) \quad (3.15)$$

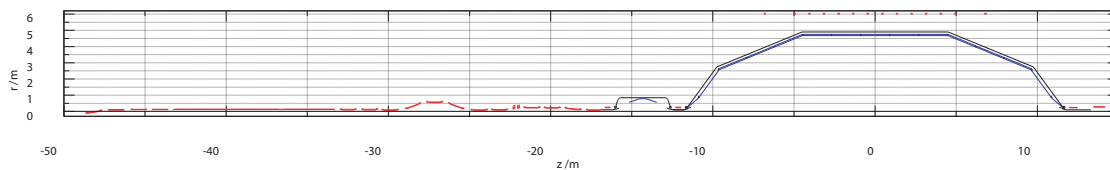
with the starting conditions

$$y_i(x = 0) = y_i^0.$$

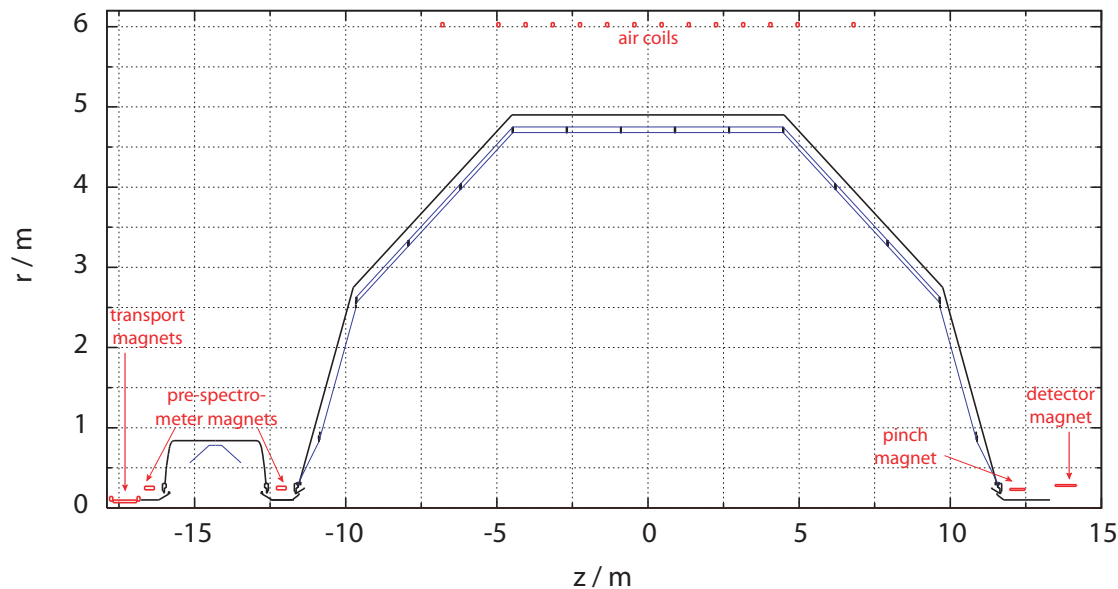
This calculates the next point in the direction the field changes least. The electric potential is calculated with the routine *elcd3_2* or *elcd3_3* (see section 3.2).

The program is called with the parameters

```
./fieldlinepot -i imax -p pathlength -R numstep -r r0 -s z0 -e z_end -n nfl -o
```



(a) Total setup with coil configuration of the KATRIN experiment



(b) The two-spectrometer section of the KATRIN experiment with the magnets used for the pre-spectrometer design simulations with magfield2 computation

Figure 3.9: The different magnetic field configurations for magfield2 and magfield3 computations

output.dat inputcoil.dat,

where `imax` gives the maximum number of points along the field line, `pathlength` the size of the steps and `numstep` the number of Runge-Kutta steps between two points on the field line. `r0` and `z0` give the starting point of the field line, `zend` the maximum `z`-value to which will be tracked and `nf1` the number of field lines in the output. The output file has the form

`z[1][j] ... z[nf1][j] r[1][j] ... r[nf1][j] Phi[1][j] ... Phi[nf1][j]`

and ends with either `z[k][imax]` or `zend`, depending on which condition is fulfilled first.

3.2 Electric field calculations

There are many commercial codes for electric field calculation (e.g. CPO² and SIMION³) on the market. None of those has turned out to be suitable for the KATRIN experiment as they are not capable of calculating such a huge setup (vacuum vessel with 23 m length and 9 m diameter) with as tiny details as the wire structure (0.2 mm diameter). Some tests with SIMION can be found in reference [Val04].

The program SIMION, for example, works with the finite difference method (FDM) which is based on the approximation:

$$\frac{f(x+h) - f(x)}{h} \approx f'(x). \quad (3.16)$$

This yields a useful method to solve differential equations. It only has one problem: the volume has to be divided into a fine grid on which adjacent points are used for further calculations. This grid has equidistant spacing leading to major memory problems when doing simulations for extended geometries with complex substructures. Therefore, an electric field calculation routine based on the boundary element method (BEM) was developed by Dr. F. Glück especially for the KATRIN setup and its symmetries ([Glu04]).

The boundary element method assumes that on a given part of the surface the charge density is homogeneous and the resulting electric field is derived from it. Discretisation is therefore an essential step for this tool to calculate accurate results. This discretisation offers the possibility to compute huge structures with tiny details as the division of electrode surfaces is independent of the total size of the setup. In an environment with different potentials, the number of elements needs to be higher than in an area with a rather homogeneous potential distribution, as the charge densities are influenced by them. Therefore, subelements of different sizes are used.

The electrode configuration of the KATRIN setup is in first approximation rotational symmetric. Therefore, starting from Coulomb's equation we also get a method to calculate the electric potential $\Phi(r, z)$ for a charged circular ring via the elliptic integrals

$$\Phi(z, r) = \frac{Q}{2\pi^2\epsilon_0} \frac{K(k)}{S}, \quad (3.17)$$

with the charge Q , $k = \frac{2\sqrt{Rr}}{S}$, the elliptic integral $K(k)$ and $S = \sqrt{(R+r)^2 + (z-Z)^2}$, and via the Legendre polynomial expansion:

²further information on <http://www.simion.com/cpo/>

³further information on <http://www.simion.com/>

$$\Phi = \sum_{n=0}^{\infty} \phi_n^{cen} \left(\frac{\rho}{\rho_{cen}} \right)^n P_n(u), \quad (3.18)$$

$$E_z = -\frac{1}{\rho_{cen}} \sum_{n=0}^{\infty} (n+1) \phi_{n+1}^{cen} \left(\frac{\rho}{\rho_{cen}} \right)^n P_n(u) \quad (3.19)$$

$$E_r = \frac{s}{\rho_{cen}} \sum_{n=0}^{\infty} \phi_{n+1}^{cen} \left(\frac{\rho}{\rho_{cen}} \right)^n P_n'(u), \quad (3.20)$$

with s being the ratio of the r to the z component $s = \frac{r}{\rho} = \frac{r}{z-z_0} = \sin \Theta$. The ϕ_n^{cen} are the source coefficients, $P_n(u)$ the Legendre polynomials and ρ the distance to the field point.

The Legendre polynomial expansion needs the source coefficients ϕ_n^{cen} , which can be expressed as the integral of the surface charge density over the total electrode surface:

$$\phi(\vec{r}) = \frac{1}{4\pi\epsilon_0} \int_S \frac{\sigma(\vec{r}_S)}{|\vec{r} - \vec{r}_S|} d^2\vec{r}_S. \quad (3.21)$$

In order to compute this expression, we need to know the electrode geometry S and surface charge densities $\sigma(\vec{r}_S)$. Therefore, the boundary element method (BEM) is an obvious choice. Under the assumption that they do not change on a surface element S_i , the charge densities are computed from the potential applied on the element:

$$U_i = \sum_{j=1}^N C_{ij} \sigma_j, \quad (3.22)$$

with $C_{ij} = C_j(R_i)$ the Coulomb matrix element which is a completely geometrical factor given by:

$$C_j(\vec{r}_i) = \frac{1}{4\pi\epsilon_0} \int_{S_j} \frac{1}{|\vec{r}_i - \vec{r}_S|} d^2\vec{r}_S. \quad (3.23)$$

Problems arise if the electric field for a point located very close to the electrode surfaces is calculated, as the BEM does not work accurately there (for an example see figure 3.10). The distance in which the deviation of the real potential appears, is also dependent on the discretisation of the electrode surfaces. For the discretisation it is important to keep in mind how close to the surface the potential will be computed (see also chapter 5).

3.2.1 elcd3_2

The program *elcd3_2* works with a complete rotational symmetry for all electrode elements but the wires. The inputfile `inputfull.dat` for the full electrode segments

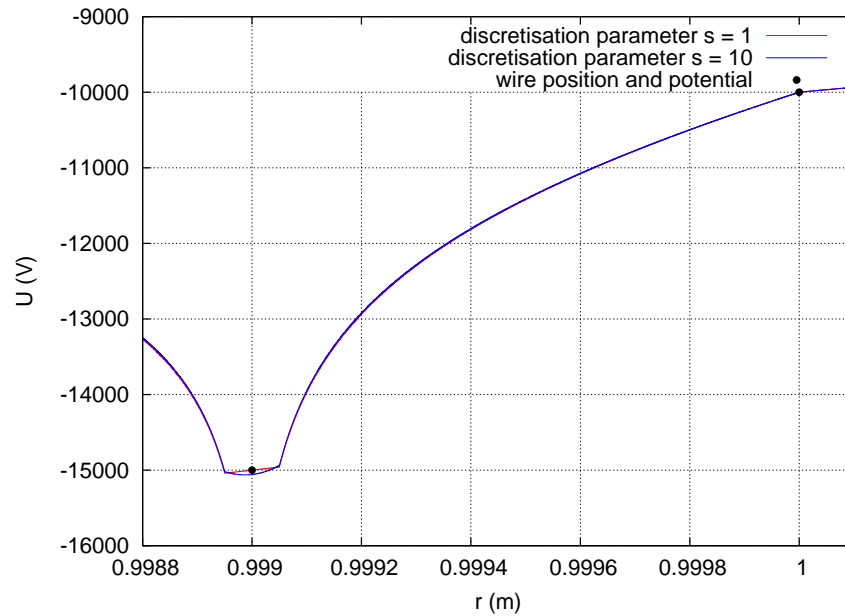


Figure 3.10: Inaccuracies in the BEM calculation: The points mark the position of wires with a diameter of 0.1 mm and applied potentials of -1000 V and -1500 V (y-axis). The potential calculated with the BEM method for bad discretisation is shown as a red line. It already deviates in a distance of $\approx 5 \cdot 10^{-5}$ m from the accurate potential. The blue curve shows the potential calculated for a better wire discretisation. Here the potential approximates the realistic gradient better, but still assumes wrong values at the same distance.

describes polygons in the r - z plane that will be rotated to create cylindrical structures.

```

Nel
z1[1]  r1[1]  z2[1]  r2[1]  U[1]  disc[1]
...
z1[Nel] r1[Nel] z2[Nel] r2[Nel] U[Nel] disc[Nel]

```

`Nel` states the total number of electrodes. Their z - and r - coordinates are given in m and U in V (for a graphic example see figure 3.11a). The parameter `disc` is used for further division of the electrode into subelements. The smaller the subelements, the more accurate the electric field gets because the surface charge density, which is assumed to be constant on the subelements, does not change abruptly but continuously. With a rising of the number of subelements the computation time increases.

In addition, the program can calculate the electric field generated by wires in a configuration with cylindrical symmetry centered on the z -axis. The wires are described in the file `inputwire.dat` with the parameters:

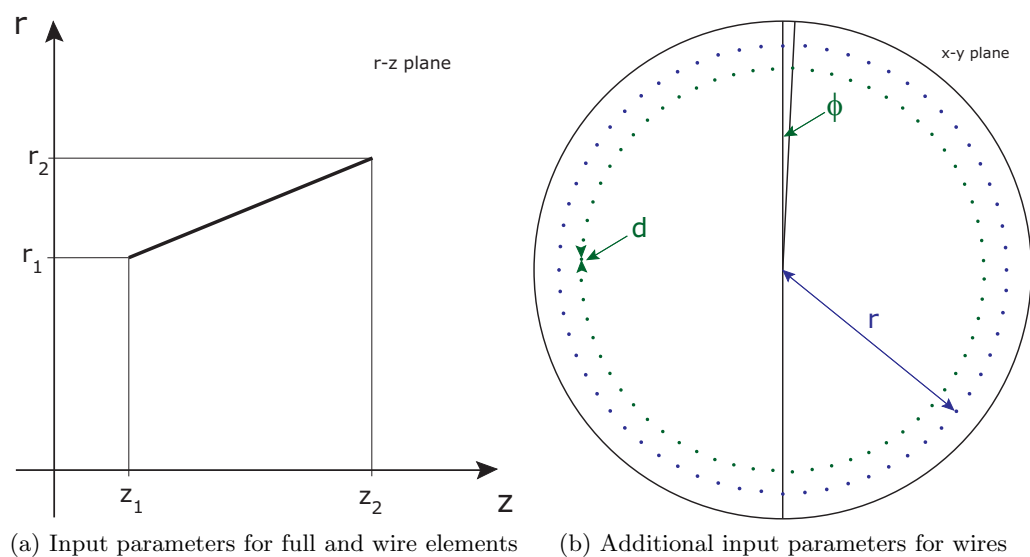


Figure 3.11: Graphic explanation of input parameters for elcd3_2

Nwire

```

z1[1] r1[1] z2[1] r2[1] d[1] phi[1] N[1] U[1] disc[1]
...
z1[Nwire] r1[Nwire] z2[Nwire] r2[Nwire] d[Nwire] phi[Nwire] N[Nwire] U[Nwire]
disc[Nwire]

```

The entry d gives the diameter of the wire, ϕ its angle to the $\phi = 0$ deg, $z = 0$ m line in degrees and N the number of wires on the total circumference (see also figure 3.11).

The source points are calculated by calling the routine

```

./elmain2 -s scale -p power -z z_mirror -d source point distance -m z_min -M z_max
inputfull.dat inputwire.dat

```

with the parameter $-s$ for additional subdivision of all electrode elements, p giving the spacing ($p = 1$: linear spacing, $p = 2$: the size of the elements decreases quadratically towards the end of the elements), z giving a mirror plane in z , the parameters m and M give the z - range for which the source points will be calculated with an equidistant spacing of d .

The potential in a point $P = (P[1], P[2], P[3])$ will be calculated when calling `elcd3_2_Phitor(P)`.

A KATRIN main spectrometer input for `elcd3_2` simulations can be seen in figure 3.12.

3.2.2 elcd3_3

With the program `elcd3_3` structures that hold only a partial rotational symmetry can be calculated. This is important for the KATRIN experiment because the influence of the support structure of the wire electrode on the electric field has to be considered

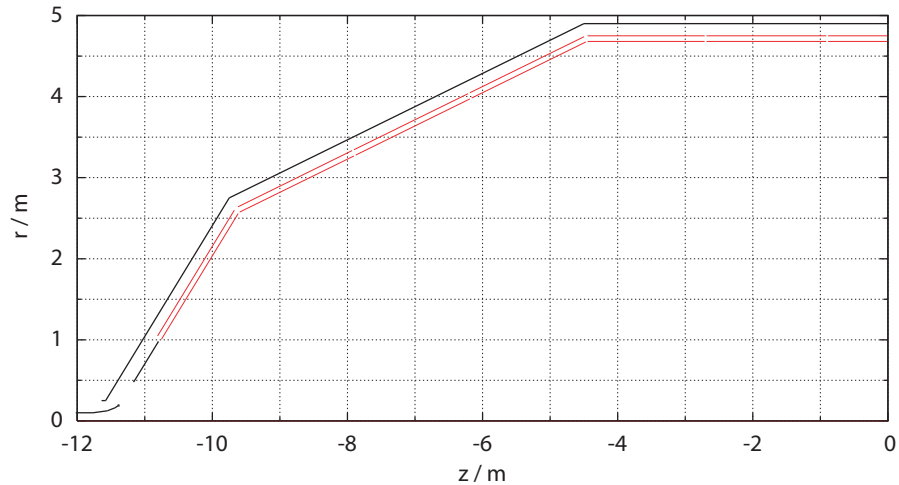


Figure 3.12: Input for *elcd3_2*, black: vessel structure, completely rotated; red: wire structure, discretely rotated

(some of these simulations are described in chapter 4).

All electrode elements are implemented as rectangles or wires. Thus complete round cylinders are no longer possible, but a multifaceted structure has to be used for an approximation.

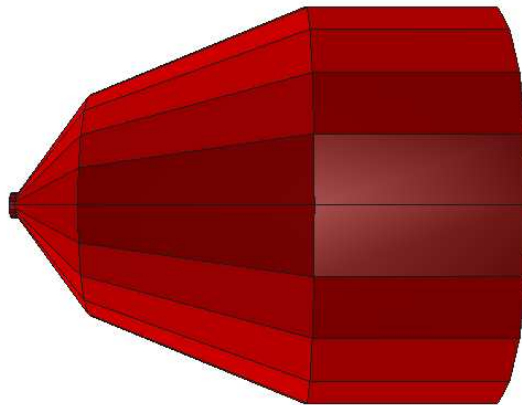


Figure 3.13: The spectrometer vessel in form of the input for *elcd3_3* with a discretisation of $rot = 20$ in angular direction (in simulations this parameter was set to 1200, the maximum number of implemented wires)

There is only one inputfile for all elements. Its first entry is the total number of elements N_{tot} . Then the elements are given. The index of the respective element is a control variable standing in the first column. Elements having the same charge density can be given the same charge density number in the second column. In the third column the

numbers 1 or 2 give the type of element: a rectangle or a wire respectively. The next column gives the rotation parameter rot .

If the element is a parallelogram (entry 1 in third column), columns five to seven give the vector \vec{P} pointing to a corner of the shape. Then the normal vectors spanning the quadrangle are given in columns eight to thirteen. Their length parameters are stored in columns fourteen and fifteen. In the last column, the potential applied to these surfaces is given. An overview of the geometry parameters is given in figure 3.14.

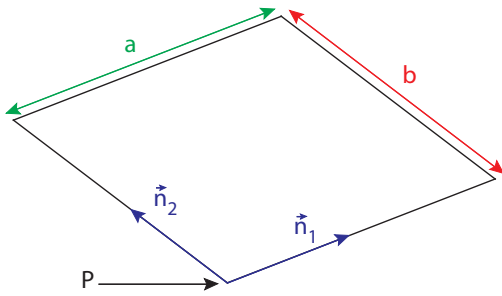
For parallelograms, a line in the inputfile will have this form:

```
 $i$   $i_\sigma$  1  $\text{rot}$   $\vec{P}_x[i]$   $\vec{P}_y[i]$   $\vec{P}_z[i]$ 
 $\vec{n}_{1x}[i]$   $\vec{n}_{1y}[i]$   $\vec{n}_{1z}[i]$   $\vec{n}_{2x}[i]$   $\vec{n}_{2y}[i]$   $\vec{n}_{2z}[i]$   $a[i]$   $b[i]$   $U[i]$ 
```

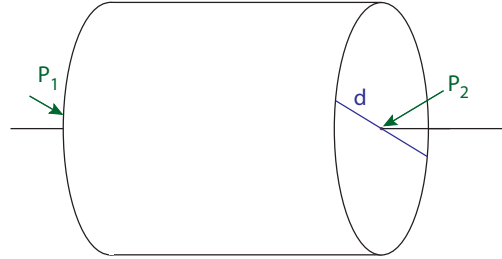
If a wire is described (entry 2 in third column), the two endpoints are given in Cartesian coordinates in column five to ten. The last parameter needed for the description is the applied potential that will be stored in column 16. Columns 11 to 15 can be filled with random numbers.

An inputline for a wire can have this form:

```
 $i$   $i_\sigma$  2  $\text{rot}$   $\vec{P}_{1x}[i]$   $\vec{P}_{1y}[i]$   $\vec{P}_{1z}[i]$ 
 $\vec{P}_{2x}[i]$   $\vec{P}_{2y}[i]$   $\vec{P}_{2z}[i]$   $d[i]$  0.0 0.0 0.0 0.0  $U[i]$ .
```



(a) Input parameters for a parallelogram in *elcd3_3*



(b) Input parameters for a wire in *elcd3_3*

Figure 3.14: Geometry input parameters in *elcd3_3*

The program is executed with the command

```
./elmain3 -m -z  $z_{mirror}$  -c -a -r  $r_{max}$  -s  $step$  inputfile.
```

If the parameter $-m$ is added, the design will be mirrored at the z -position z_{mirror} , per default at $z = 0$ m. The parameter $-c$ allows the program to use the circle approximation (at the moment not recommended). Giving the term $-a$ leads to the output of a testfile scanning the analysing plane. The parameter r_{max} stores the end radius of the scan, per default $r_{max} = 4.5$ m, which marks the end of the flux tube in the analysing plane. The variable $step$ stores the step length between two output points. For *elmain3* only one inputfile can be added.

The potential in a point $P = (P[1], P[2], P[3])$ will be calculated when calling *elcd3_3_Potential*(P), the electric field will be computed if the routine *elcd3_3_elfield*(P,E,Phi) is called.

3.2.3 Setting up the inputfiles: gmainspec

As described before the input file for *elcd3_3* is difficult to follow. There is no possibility to characterize the input parameters more clearly and mistakes therefore become common while typing the numbers. Programs like *gnuplot* can be used to visualize the 2-dimensional input for *elcd3_2*, this is neither simple for the 3-dimensional structures used in *elcd3_3* nor is this kind of visual control foolproof.

As many input parameters were already fixed when changing from *elcd3_2* to *elcd3_3* (e.g. the distance between the wire layers and the vessel hull, the form of the holding structure for the cylindrical modules, see also section 4) a tool was programmed by S. Vöcking to automate the file construction and allow an easy way to convert *elcd3_2* into *elcd3_3* input files. In addition to that, the *python* based program was connected with a *root* program, *rootsim*, which generates a 3-dimensional model of the input parameters. In order to reduce mistakes, it is useful to consider only an angular cutout, as otherwise the structures will not be easily recognisable. For an example, see figure 3.15.

3.2.4 MBEM - an improved method for calculating electric fields

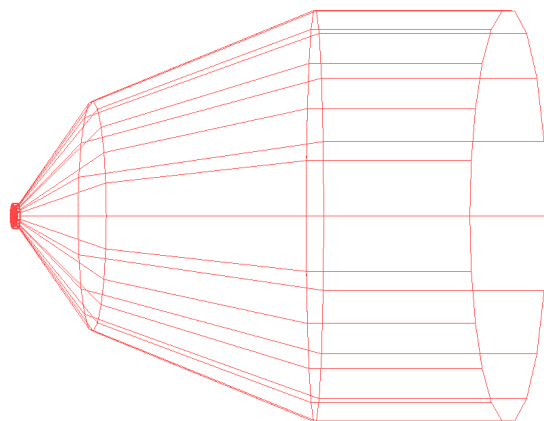
The size of the memory needed for the BEM calculations rises approximately with the square of the number of elements N^2 . Therefore with a RAM size of the order of 1 GB, a maximum number of approximate $N \approx 1000$ elements can be implemented in a simulation. This number is, as mentioned above, clearly not enough for the KATRIN experiment if a computation of the whole setup without discrete rotational symmetry should be done. Implementing more complex and smaller structures, the rotational symmetries used in simpler and faster models are lost. Therefore, a larger number of subelements with independent charge densities has to be used in the computations. To solve this problem, new methods for field calculations have to be investigated.

One possibility is the usage of the multipole boundary element method (MBEM) for field calculations. It separates for each field point the surface elements which contribute to the field strength into near and far elements. The near elements are computed in the way already described for the *elcd3_2* und *elcd3_3* routines. Elements far away are summed into bigger boxes for which the monopole, dipole and quadrupole of all subelements inside were calculated in advance. To get the effect from the far elements, the multipoles are taken into consideration. The implementation of this method to a program compatible for the KATRIN simulation tools is done by S. Vöcking and described in detail in reference [Voe08].

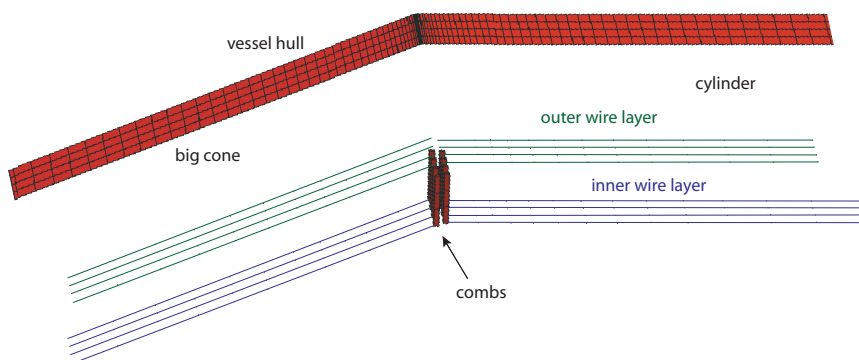
3.3 Tracking

3.3.1 Microscopic tracking with traj

The tracking routine *traj.c* is based on the microscopic calculation of the movement of a particle which is determined by six first order differential equations



(a) A total view of the main spectrometer with *rootsim*



(b) An angular cut of the main spectrometer showing in detail the holding structures

Figure 3.15: Different perspectives of the main spectrometer seen with *rootsim*

$$\begin{aligned}\dot{\vec{x}} &= \vec{v} \\ \dot{\vec{p}} &= \vec{F}_L,\end{aligned}\tag{3.24}$$

with the Lorentz force $\vec{F}_L = q(\vec{E} + \vec{v} \times \vec{B})$. For each point \vec{x} that is evaluated along the trajectory, the electric and magnetic fields are evaluated and used to solve the equations 3.24.

A detailed description of the input parameters and coefficients can be found in references [Val04, Voe08, Val08].

This program is useful because it also calculates the violation of the adiabatic energy

transformation. It can be used with the program package *elcd3_2*. Using *elcd3_3* leads to problems because the field calculation routine `elcd3_3_elfield`, which needs to be called for each point on the trajectory, is slow. Several tests have been made to make microscopic tracking available for the *elcd3_3* program package, including

- the reducing the parameter `ntimestep` leading to a reduced accuracy
- the usage of a prepared electric field card from which the field will be evaluated by finite differences - for this the field will have to be calculated once on a time on a grid pattern. This approach is used by the Fulda group with the program *PartOpt*^{TM4} but is not serviceable for design calculations.

Therefore, for design calculations the program *transmission.c* is used. As described in section 3.3.2 it is based on several assumptions. Thus, a check of the simulations with *el-traj* is essential after finishing a simulation step.

3.3.2 Transmission

The program *transmission.c* was specially written for the KATRIN main spectrometer. It is based on the assumption that the energy of an electron is transformed adiabatically in the MAC-E filter. Using the starting parameters set by different parts of the whole KATRIN experiment, the track of an electron at the edge of the flux tube is calculated. In this computation the cyclotron motion around the field line is neglected and only the path along a field line is computed. The output is the z - and r position of the electron with its corresponding energy.

The starting conditions are given by the experimental setup (the numbers mentioned below are approximate; they are calculated exactly in the program each time it is called):

- Starting position:

For the z_{start} value the middle of the entrance magnet should be chosen as here a homogeneous field predominates.

The maximum r_{max} value of the flux tube at the given z_{start} value is calculated with the maximum radius r_{WGTS} in the windowless gaseous tritium source (WGTS):

$$r_{max} = \sqrt{\frac{B_{WGTS}}{B_{z_{start}}}} r_{WGTS}.$$

The magnetic field in the WGTS has a strength of $B = 3.6$ T and the maximum radius there is $r_{WGTS} = 4.2$ cm, resulting in a starting radius of

$$r_{start} \approx \sqrt{\frac{3.6 \text{ T}}{4.0 \text{ T}}} \cdot 0.042 \text{ m} \approx 0.0398 \text{ m for } z_{start} = -12.13 \text{ m} \quad (3.25)$$

- Starting angle:

The maximum angle in the WGTS is given by the magnetic bottle effect and amounts to $\approx 51^\circ$, leading to an angle of $\approx 55^\circ$ at $z_{start} = -12.13$ m

⁴For further information visit www.partopt.net

- Starting energy:

The starting energy E_0 is calculated for an electron just passing the MAC-E filter, meaning that the longitudinal energy of the particle is equal to zero in the analysing plane $E_{long}^{ana} = 0.0 \text{ eV}$. This means that the retardation potential is equal to the longitudinal energy $E_{long,no}^{ana}$ the electron should have, if no electric fields are present:

$$0 = E_{long}^{ana} = E_{long,no}^{ana} - q \cdot (U_{ana} - U_{start}). \quad (3.26)$$

The energy in the analysing plane can be expressed in terms of the starting energy:

$$\begin{aligned} E_{long,no}^{ana} &= E_{tot}^{start} - E_{\perp}^{ana} \\ &= E_{tot}^{start} - E_{tot}^{ana} \cdot \sin^2 \Theta_{ana} \\ &= E_{tot}^{start} - E_{tot}^{start} \cdot \frac{B_{ana}}{B_{start}} \cdot \frac{1 + \gamma_{start}}{1 + \gamma_{ana}} \cdot \sin^2 \Theta_{ana} \\ &= E_{tot}^{start} \cdot \left(1 - \frac{B_{ana}}{B_{start}} \frac{1 + \gamma_{start}}{1 + \gamma_{ana}} \cdot \sin^2 \Theta_{start} \right). \end{aligned} \quad (3.27)$$

Fitting equation 3.27 into 3.26 and solving for E_{tot}^{start} gives the starting energy of the electron

$$E_{tot}^{start} = \frac{q(U_{start} - U_{ana})}{1 - \sin^2 \Theta_{start} \cdot \frac{B_{ana}}{B_{start}} \frac{1 + \gamma_{start}}{1 + \gamma_{ana}}}. \quad (3.28)$$

Due to the retarding potential, the energy in the analysing plane is small. Therefore, there is no need to calculate relativistic there and $\gamma_{ana} = 1$. At the starting point the relativistic factor has the maximum value it can get in the tritium β - decay: $\gamma_{start} \approx 1.04$.

After setting the starting conditions, the next z_i point at a distance h is used to calculate the longitudinal energy $E_{long}(z_i)$ by subtracting the transversal component and the energy loss in the electric field:

$$\begin{aligned} E_{long}(z_i) &= E_{tot}^{start} - q(U(z_i) - U_{start}) - E_{\perp}(z_i) \\ &= q(U_{start} - U(z_i)) - E_{tot}^{start} \cdot \left(1 - \sin^2 \Theta_{start} \cdot \frac{B(z_i)}{B_{start}} \frac{1 + \gamma_{start}}{1 + \gamma(z_i)} \right) \end{aligned} \quad (3.29)$$

The potential and magnetic field strength are assumed homogeneous in the analysing plane. In order to take into account deviations, the values are approximated with the Newtonian iteration method.

A detailed description of the programs magfield2, magfield3, elcd3_2, elcd3_3 and the microscopic tracking routine can be found in references [Glu06b], [Val04] and [Voe08].

4 Design simulations for the wire electrode

This chapter gives an overview of the design specifications and modifications that have been done in the course of this diploma thesis. In this section tolerance simulations as well as the implications of technical and mechanical necessities will be discussed. The additional shielding electrode for the entrance and exit region will be discussed in detail in section 6.5.

Tolerance simulations have been done for the cylindrical part of the wire electrode. These only included radial displacement, as irregularities in angular direction cannot be implemented in the rotationally symmetric design.

In the run of the design optimisation the program *gmainspec.py* (see section 3.2.3) was developed, tested for bugs, modified, and put into operation. The current design has been constructed with the help of this program.

4.1 Tolerance simulations for the cylindrical part of the wire electrode

Tolerance simulations for the cylindrical part of the wire electrode were done in an earlier phase of the design process with the program package *elcd3-3* and the tracking routine *transmission.c* (a detailed description of these programs can be found in chapter 3). At that time, only combs and endcaps in the cylindrical part were implemented in the simulations (see figure 4.1 for geometry details). Each module ring and their respective wires were displaced in the radial direction to see the result of inaccurate mounting.

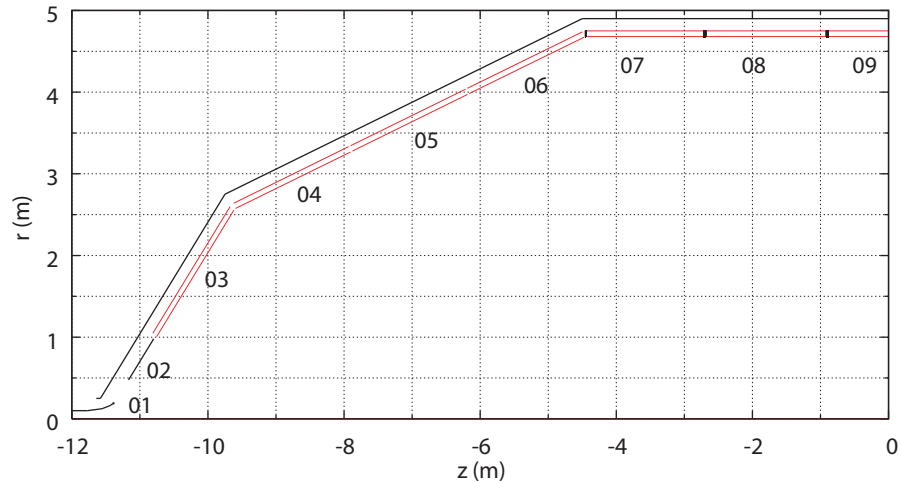
The original design revealed a potential depression in the analysing plane of ≈ 0.9 V (see figure 4.2). The potential depression ΔU is defined as the maximum inhomogeneity

$$\Delta U = U_{max} - U_{min}$$

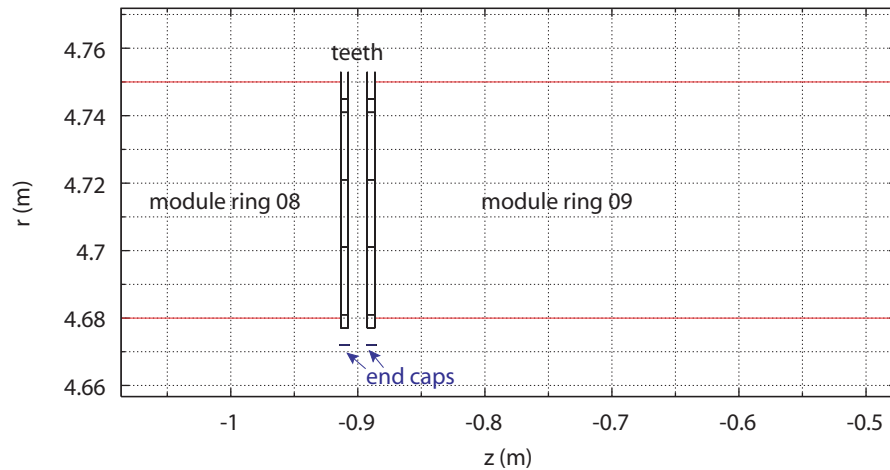
in the analysing plane for the whole flux tube. With a value of $\phi = 191$ Tcm², the maximum radius with $B_{min} = 3$ G in the analysing plane is $r = 4.5$ m.

In order to test how the displacement influences the transmission, electrons in the outer flux tube area are tracked with the program *transmission.c*. These electrons are used, as they will pass very close to the wire electrode and will therefore be the first to see an effect of inaccuracies in the mounting of the electrodes.

For the exact setup, the whole flux tube is transmitted. In figure 4.3 one can see the influence of the holding structure: In the area of the gaps between the combs, where the more positive potential -18400 V of the vessel hull and -18500 V from the holding structure is not effectively screened by a wire layer, the electrons gain longitudinal energy.



(a) Geometry used for the tolerance simulations: Comb holding structure for the cylindrical, no holding structure in the conical part



(b) Zoom to comb structure with endcaps implemented for the tolerance simulations

Figure 4.1: Geometry setup for the tolerance simulations

The displacement simulations were done by shifting complete module rings, as otherwise the rotational symmetry is broken and the computation would be too time, memory and computer power consuming. Nevertheless, from these simulations limits can be deduced for the mounting of every single module, as the transmission is tested for electrons passing very close to the wires. The influence of the other modules can be neglected at these points, as within these distances to the wire electrode only the closest module contributes significantly to the potential.

For the tolerance simulations, one end of a wire module was displaced with respect to its original position in positive and negative r -direction. For module ring 09 this was only possible for both ends at the same time due to the mirror plane at $z = 0$ m. A schematic

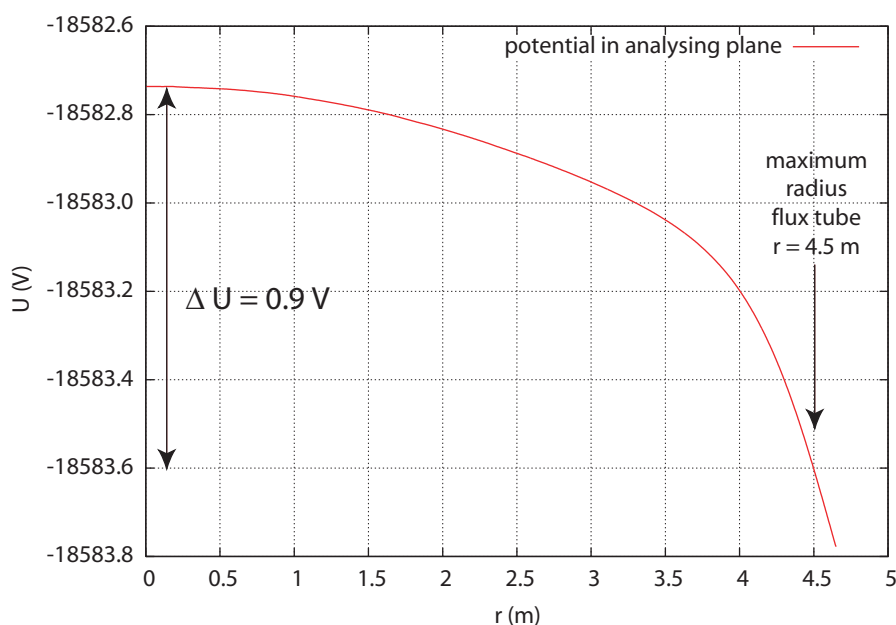


Figure 4.2: Potential depression for original input with no displacements

view of the different displacement possibilities is given in figure 4.4.

If a displacement is too severe, some of the outer electrons cannot pass the MAC-E filter, which will be seen in negative longitudinal energies (see figure 4.5).

Figure 4.5 shows how a displacement of the center module ring (09) will influence the outer electrons of the flux tube: these will not pass the filter at the expected retarding potential, as their longitudinal energy reaches negative values. Therefore they will be reflected back towards the source. Electrons with the same starting radius and angle but excess starting energies can pass the filter. This leads to a deviation of the sharp analytical form in the saturation region of the transmission function and should be avoided. Table 4.1 summarizes the results of these simulations.

Table 4.1: Results of the design simulations: maximum displacement in radial direction

Module ring	upper limit for displacement
09	± 0.5 mm
08	-0.5 mm
07	-1 mm

In table 4.1 for module rings 07 and 08, displacement limits are only given in the radial direction towards the center of the spectrometer. Limits on a dislocation towards the vessel hull are much more relaxed with respect to negative longitudinal energies, but show changes in the transmission behaviour (see figure 4.6) that should be investigated separately to analyse whether the adiabatic transformation is still valid in these cases.

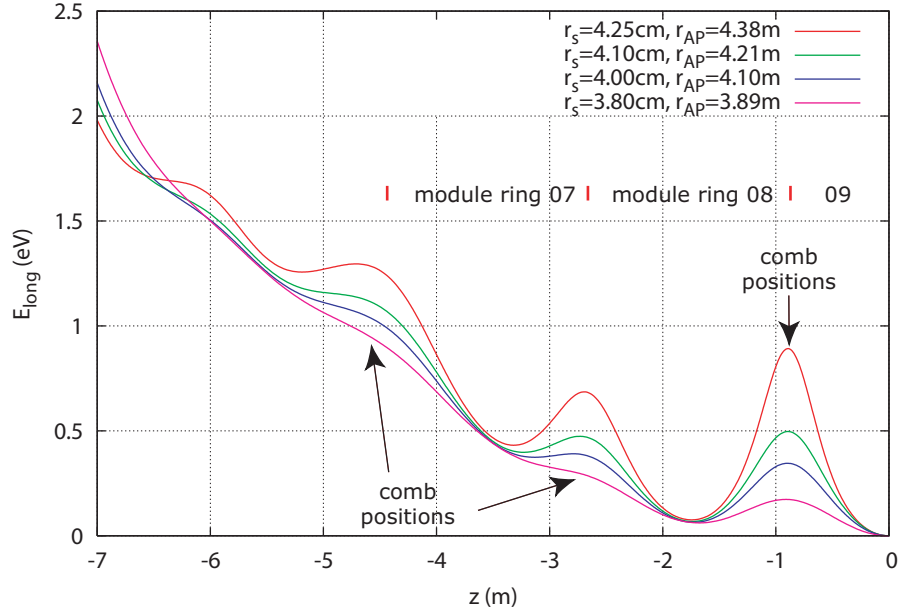


Figure 4.3: Transmission of outer electrons for original input with no displacements

Simulations with only one end of a module displaced show that the transmission is more sensitive on the module end in the direction of the analysing plane. This is due to the smaller distances between flux tube and wire electrode in the center of the spectrometer and the lower electron energy.

These simulations show that an exact mounting is very important in order to get full transmission. The displacements can be seen as a misalignment between two modules. If one module edge ends on a different radial level than the next, this leads to an offset in the potential distribution, thus changing the path of electrons close to the corresponding module junction. If both modules were to be misaligned to a similar extent, the potential does not change as abruptly. Therefore, the mounting structure inside the spectrometer vessel has been adjusted to control the displacement between two adjacent modules.

The holding structure that will be mounted in the spectrometer vessel has been optimised to avoid the abovementioned displacements. A ring structure will be installed inside the vessel at the module intersection points. The ends of the modules will be attached to these rings. As adjacent modules are attached to the same ring, the discrepancies will be kept at a minimum.

As of now, no statement can be made with respect to misalignment between modules of the same ring, as these simulations require significant reduction of the applied rotational symmetries.

Tests have been made for the step cone to estimate the influence of displacements there. Changing the position of module ring 02 by around 1 cm shows no visible influence on the transmission. This can be due to the large distances between the electrode and the flux tube. In addition, electrons in this region still have longitudinal energies above

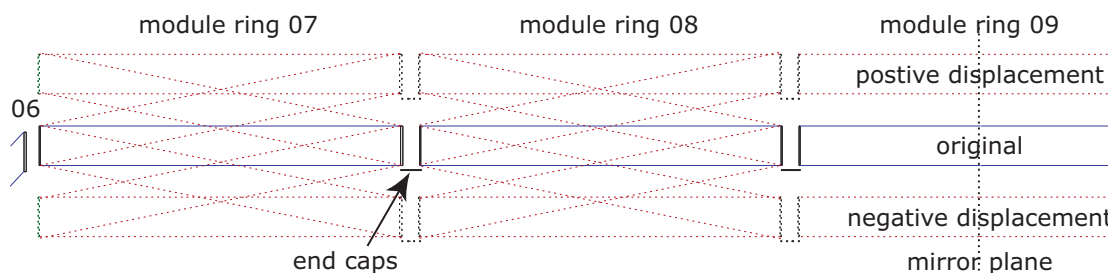


Figure 4.4: Schematic view of the wire electrode displacements. For the simulations each module ring of the cylinder was investigated separately. For module rings 07 and 08 either one end alone or both ends together can be displaced. Due to the symmetry plane, module ring 09 can only be displaced with both ends at the same time. The modules have a length of 1.8 m. The displacements were tested in the mm range.

10 keV. Therefore, the influence of changes in the transmission function of ≈ 10 eV are not directly visible. In contrast, electrons close to the analysing plane only have energies in the 10 eV range and are therefore very sensitive to any changes.

Although they were done with a fragmentary setup, these simulations give clear indication of the precision needed for the experiment. As they do not answer all questions, it would be useful to conduct a more detailed study with the more detailed present setup, especially for modules in the big cone.

4.2 Detailed simulations of the wire electrode

As mentioned in the previous section, the implementation of all detailed structures turned out to be difficult and error-prone.

Simulating the KATRIN setup in detail has proven to be difficult because of the extensive structures as well as the complexity of the input parameters needed for the code (see also section 3.2). Therefore, the structural details were implemented step by step and tested separately.

To simulate the KATRIN setup completely, the program *elcd3_3* has to be used. With the program *elcd3_2* only 2-dimensional structures can be implemented as polygons. These line elements are rotated totally. This would for example lead to 'barrel hoops' instead of comb structures. The program *elcd3_3* uses rectangles that are then rotated in discrete steps.

The implementation of comb structures (a technical drawing of a cylindrical comb can be seen in figure 4.7) in *elcd3_3* is not easy. The full material structure has to be approximated with surfaces.

To maintain the highest level of symmetry possible, the subdivision into a modular design was neglected. A single tooth (see figure 4.8) of the comb structure is implemented into the program and rotated to represent the holding structure.

For the cylindrical part, the 1200 wires per layer (60 per module and layer) are included.

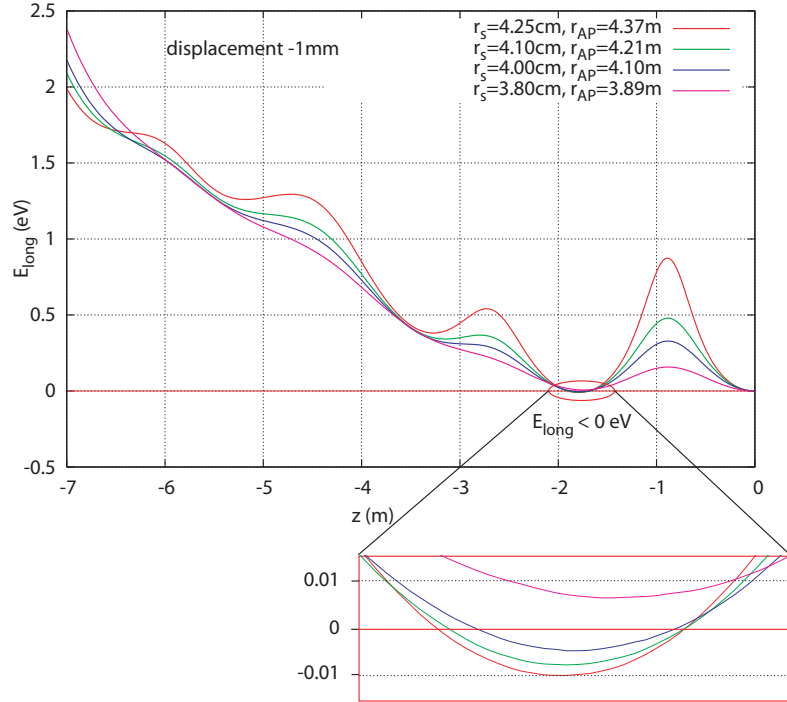


Figure 4.5: Transmission problems due to a displacement of module ring 09 by -1 mm

Therefore, also 1200 teeth have to be implemented. In the conical part, the number of wires per module and layer decreases (see table 4.2), thus also the rotation parameter of the combs becomes smaller.

Table 4.2: Number of wires for the different module rings

Number of wires	Cylinder			Large cone			Steep cone	
	09	08	07	06	05	04	03	02
Per module and layer	60	60	60	52	42	34	40	50
Wire layers	2			2			1	
Per layer	1200	1200	1200	1040	840	680	400	200

The rotation in the conical part is more complicated than in the cylinder, because the base structure has to be adjusted in width to cover the radius continuously, and also the length of the teeth needs to be varied, because of the slope of the conical part. The comb structure has been designed to 'stand' perpendicular to the spectrometer axis. In order to have the same shielding factor everywhere, the inner wire layer is placed at a distance of 220 mm parallel to the vessel hull, leading to longer combs for the holding structure (see also figure 4.9).

The implementation of the combs for the cylinder was first tested by hand, while the structure in the conical part was originally represented by barrel hoops. The end caps

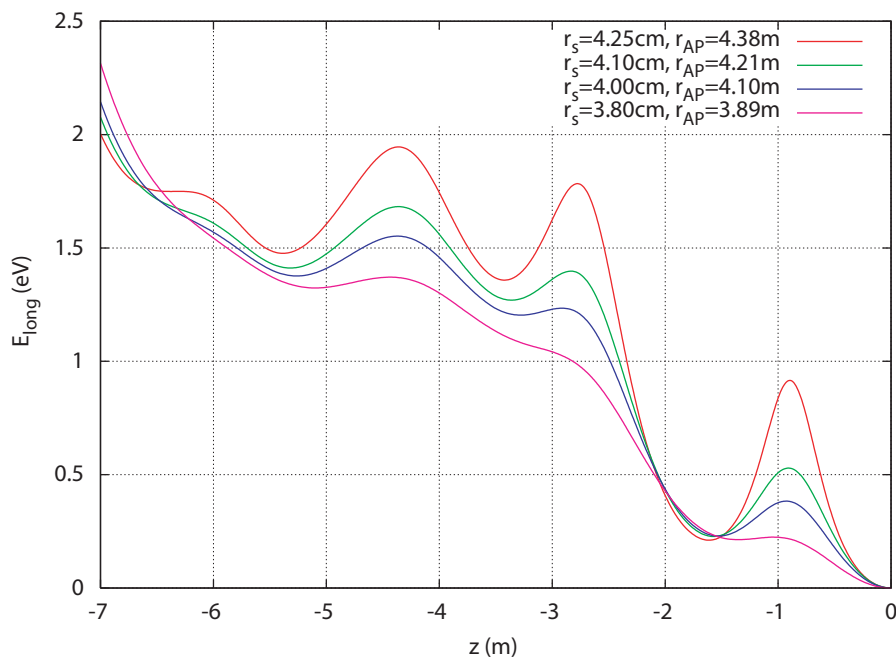


Figure 4.6: Changes in the transmission curves for displacements towards the vessel hull, example for a displacement of module ring 07 with +4 mm

were already implemented as one, shielding the complete gap between the combs where the vessel potential can penetrate through (see reference [Val08]). Residual influence of the holding structure can be seen in longitudinal energy plots as e.g. figure 4.3. In a next step the barrel hoops in the conical part of the spectrometer were replaced by a comb structure with the help of the program *gmain.spec.py*.

By default, the axial distance between the cylindrical modules of 6 mm has been chosen. Increasing this gap to 8 mm while elongating the end caps, showed an increase for the potential depression to 1.40 V and is therefore not advisable. The transmission is not visibly affected by the change.

For the intersection between the cylindrical part of the spectrometer and the cone, the outer wire layer was chosen as reference, as this is technically easier to realise than a continuous inner wire layer. Between the two possibilities, a marginal improvement of ≈ 0.03 V for the potential depression has been seen in the simulations. The transmission seems to be nearly uninfluenced by these changes as the flux tube has a larger distance to the intersection point.

Increasing the gap between the modules in the large cone increases the potential depression by ≈ 0.02 V, a much smaller dependence than in the cylindrical part because of the larger distance towards the analysing plane. No noteworthy influence on the transmission could be seen.

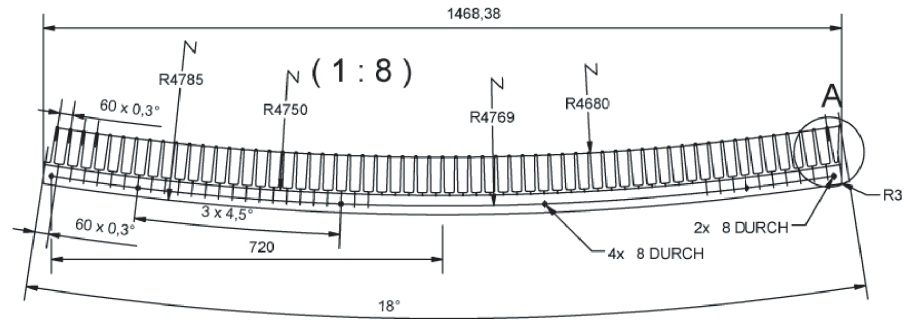


Figure 4.7: Technical drawing of the comb structure in the radial plane

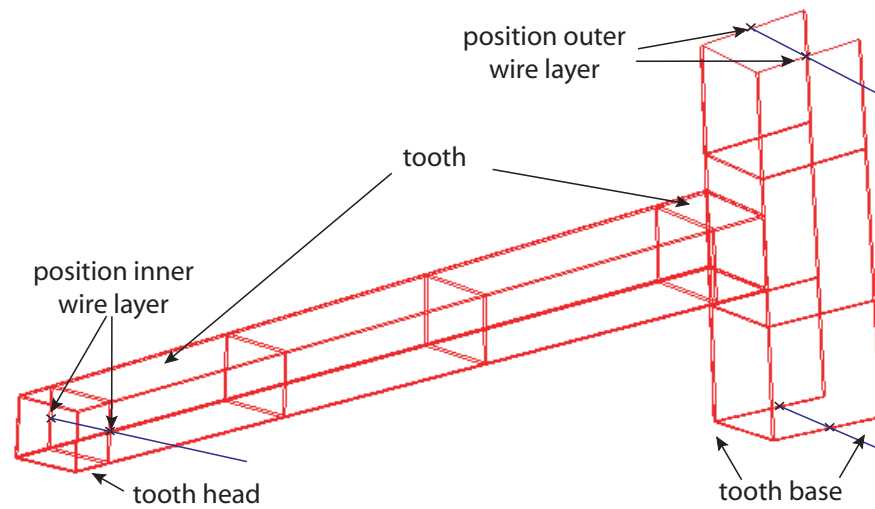


Figure 4.8: A tooth of the comb holding structure in the form as implemented in *elcd3_3* simulations

In the steep cone the length of the teeth increases to

$$l = \frac{0.07 \text{ m}}{\cos \Theta} \approx 0.12 \text{ m}$$

with $\Theta \approx 54^\circ$. Combs of this length will be rather fragile and prone to damages by shocks. Therefore, the two layer structure is not applicable here, as a technical realisation seems hardly feasible. As the surface area of the steep cone only includes $\approx \frac{1}{10}$ of the total spectrometer area, the background expected from this region is low. Therefore only a one layer electrode will be implemented here at a distance of 0.20 m parallel to the vessel hull. Because of the high electric field strength, the diameter of the wires is chosen to be 0.3 mm. The number of wires has been increased to 400 in order to improve the screening. The maximum field strength on the wire surface for all wires in one layer at

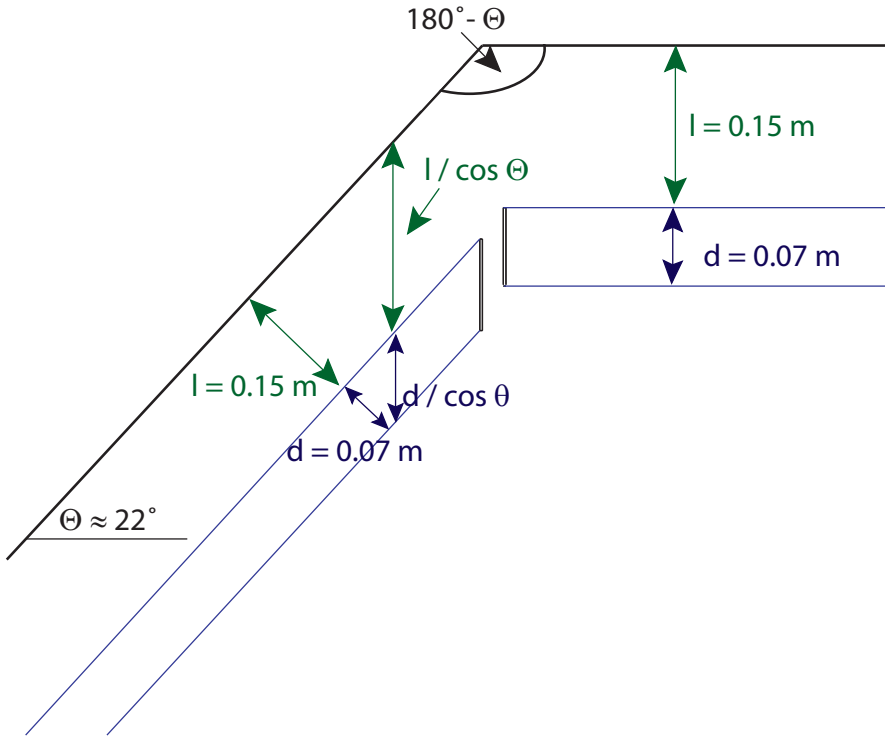


Figure 4.9: Schematic close-up view of the mounting structure in the conical part

an equal potential (neutrino mass measurement mode) can be estimated with formula

$$E_{surf,wire} = \frac{\Delta U}{l} \frac{s}{\pi d}. \quad (4.1)$$

It describes the enhancement of field strength at the surface of a wire with diameter d , within a layer with spacing s between each neighbouring wire in distance l to a full electrode as compared to the field of a planar condensator (see also figure 4.10). The field strength between two planar electrodes is, neglecting fringe effects, constant. The distance between the field lines is constant. Replacing one of the electrodes with a wire layer, the normally equally spaced lines which would cover a surface of length s (the distance between the wires), are now focussed on the wire surface πd . This gives rise to an increase in field strength of a factor $\frac{s}{\pi d}$.

For the module ring 03 with a distance $l = 0.20$ m to the vessel hull, a maximum potential difference $\Delta U = 200$ V, a wire diameter $d = 0.3$ mm and a distance between the wires of

$$s = \frac{2\pi r}{N} = \begin{cases} 0.040 \text{ m} & \text{for } r = 2.526 \text{ m} \\ 0.007 \text{ m} & \text{for } r = 0.436 \text{ m} \end{cases}$$

for the number of wires $N = 400$ the field strength on the surface rises to

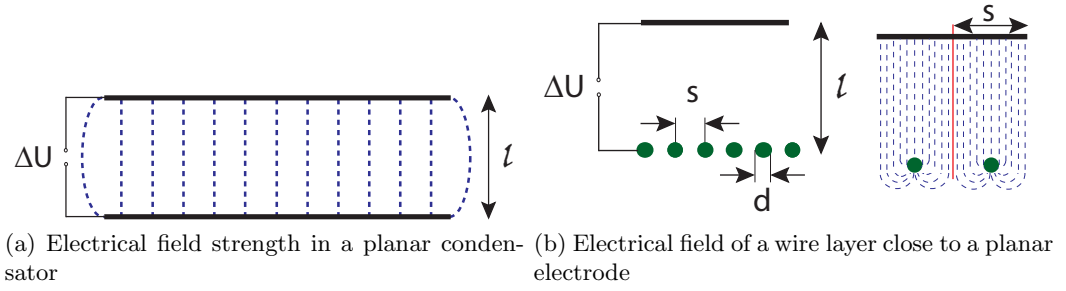


Figure 4.10: Graphic illustration of equation (4.1)

$$\begin{aligned}
 E_{surf,wire} &= \frac{2\Delta U r}{N l d} \\
 &= \begin{cases} 42.1 \frac{\text{kV}}{\text{m}} & \text{for } r = 2.526 \text{ m} \\ 7.3 \frac{\text{kV}}{\text{m}} & \text{for } r = 0.436 \text{ m.} \end{cases}
 \end{aligned}$$

The maximum field strength will be applied to the wires in the dipole mode ($\Delta U = 1 \text{ kV}$) where the wire electrode will be divided into two halves.

At the junction between the applied potentials, wires with a potential difference of 1 kV are placed next to each other. As the potential difference is applied between the wires, equation 4.1 cannot be used here. Therefore, the field strength has to be simulated. As this is not possible for the complete setup, an approximative simulation has been devised. For the relevant radii, a cylindrical setup consisting of a full electrode vessel on 0.5 kV and 2 wires with $Nrot = 4$, one on -1 kV and one on ground potential, has been used to calculate the charge densities (a schematic view of the setup is given in figure 4.11). The electric field is then calculated in close distance ϵ to the wire¹. The electric field strength for several values of ϵ is given in table 4.3.

Table 4.3: Electric field strength on a wire surface simulated of one wire

r	10^{-7}	10^{-8}	10^{-9}	10^{-10}
2.525 m	312.442 kV/m	312.564 kV/m	312.577 kV/m	312.578 kV/m
0.435 m	460.520 kV/m	460.697 kV/m	460.714 kV/m	460.716 kV/m

To test how adding more wires influences the field strength, additional simulations have been done with 3 wires on each potential. The results can be seen in table 4.4

From experience at the Mainz experiment, a benchmark value for field strengths of $400 \frac{\text{kV}}{\text{m}}$ at an electrode surface beyond which field emission started for various wire electrode setups has been derived [Glu08]. This is not reached with the wire electrode in module ring 03, as the lower end is located at a radius significantly larger than 0.435 m and will

¹A calculation directly on the wire surface is not directly possible, as described in section 3.2 and 5.

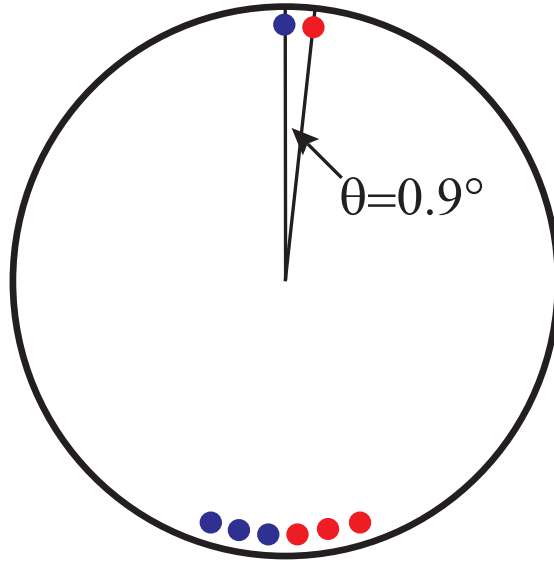


Figure 4.11: Schematic view of setup for electric field strength simulations

Table 4.4: Electric field strength on a wire surface simulated of three wires

r	10^{-7}	10^{-8}	10^{-9}	10^{-10}
2.525 m	278.183 kV/m	278.291 kV/m	278.302 kV/m	278.303 kV/m
0.435 m	406.951 kV/m	407.103 kV/m	407.117 kV/m	407.119 kV/m

therefore possess larger wire spacing than assumed in the table. Module ring 02 will end at a radius of $r \approx 0.435$ m, but as it has only 200 wires, the field strengths will therefore remain below $400 \frac{\text{kV}}{\text{m}}$.

In addition, the manufacturing process requires the angles between the comb teeth to have a maximum of 2 digits as otherwise inaccuracies occur during the automated drilling due to error accumulation. This is fulfilled with $\frac{360^\circ}{400} = 0.9^\circ$.

Module ring 02 was originally planned as a full metal cone electrode, because of field strength considerations. However such a solid electrode does not possess any background shielding, which might cause problems. This is critical for the downstream end of the spectrometer, close to the detector. Furthermore, technical aspects such as the weight and required mechanical precision added to the decision to change it into a wire electrode structure. A total number of 200 wires has been chosen.

The distance between the two module rings in the steep cone has been chosen to be 0.02 m. This distance is of the order of the distance between the wires, as this would otherwise deteriorate the background shielding. The former full metal cone has been extended towards the flange to improve the suppression of the Penning trap there. Its potential has been increased to -18500 V with its mounting structure taking the vessel potential of -18400 V. The potential difference of $\Delta U = 100$ V allows a slight screening of background arising from the comb structure. As inside the vessel no potentials of

more positive value than the one applied on the hull should be used, this value is fixed. Further information on this extension and the modification of the ground electrode can be found in section 6.5.

5 Simulations of the emission characteristics of the pre-spectrometer electron gun

In this chapter simulation results for the electron gun calibration source of the KATRIN pre-spectrometer are presented. The source was conceived by the Troitsk group, unfortunately without providing detailed documentation. Therefore these simulations were done in order to obtain a better understanding of the design and to provide a basis for the analyses.

For the calibration of a MAC-E filter an all-angle emitting point-like source of monoenergetic electrons with known angular emission is needed. It is used to resolve the important properties of the MAC-E filter for the analysis of a measured transmission function. In the first section, the requirements on the electron source are listed. In the next section, the electron gun setup of 2006 at the pre-spectrometer is described¹. A detailed account of the steps done in preparation for the simulations can be found in section three. The simulation of the electron gun and a measured transmission function are compared in the last section.

5.1 Electron source properties required for the calibration of a MAC-E filter

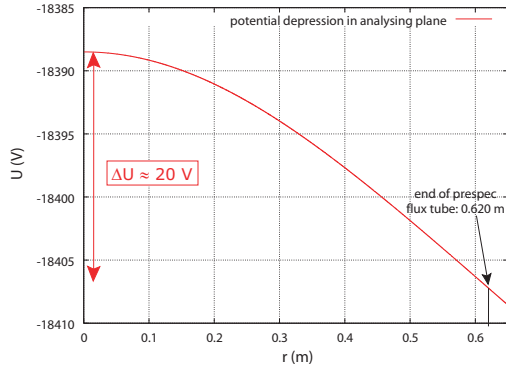
The maximum retardation potential that determines the analysis of the electron energies is located in the analysing plane. Because of the size of the spectrometers (flux tube diameter in analysing plane of the pre-spectrometer 1.24 m, main spectrometer 9.0 m), the potential is not homogeneous over the whole plane, but shows a decrease towards the center (see figure 5.1).

In the analysis of a measured spectrum this must be taken into account. Estimates of the potential depression in the analysing plane can be obtained from simulations (see figure 5.1), but they should be verified by measurements.

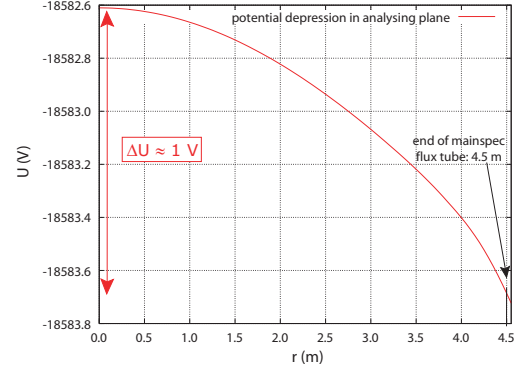
Similarly, the strength of the magnetic field cannot be assumed to be homogeneous across the analysing plane. In the center of the flux tube the magnetic field strength is higher than near the border (see figure 5.2).

Therefore, it is useful to subdivide the flux tube into radial sections and analyse each of them separately. This is done with a segmented detector (see figure 2.9). Its division into

¹In this setup several discharges were noted which led to a flaking of the gold layer. In addition, when replating the gold layer small craters were noticed that might be due to the impact of positive ions. Therefore, the electron gun geometry has been revised [Fra07] and a new tip has been used since.

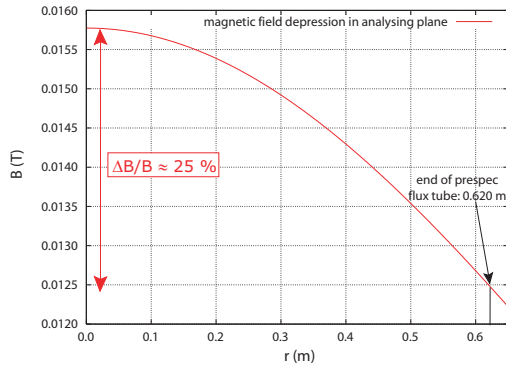


(a) Potential depression for the pre-spectrometer at $z = 0.0$ m

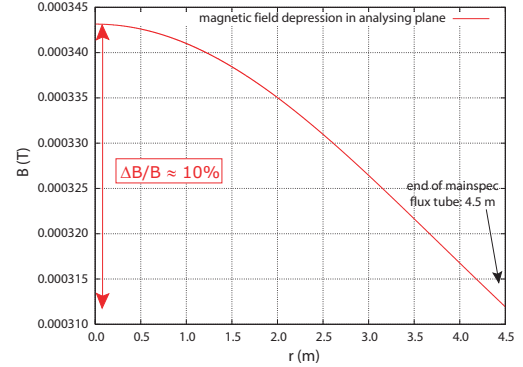


(b) Potential depression for the main spectrometer at $z = 0.0$ m

Figure 5.1: Simulated potential depressions in the spectrometers



(a) Magnetic field strength depression for the pre-spectrometer at $z = 0.0$ m



(b) Magnetic field strength depression for the main spectrometer at $z = 0.0$ m

Figure 5.2: Simulated magnetic field strength depressions in the KATRIN spectrometers

radial parts should be adjusted to the simulated potential depression in the analysing plane to ensure that each radial detector segment covers about the same potential depression ΔU . The additional subdivision in ϕ -direction allows all segments to cover about the same area. In addition, eventual asymmetries in the setup can be detected and evaluated. Each of the sections will be analysed separately, taking into account the potential and magnetic field depression in the corresponding flux tube area.

To measure the transmission function for each detector segment, an electron source with well defined properties is needed. With the electron beam, different regions of the spectrometer shall be tested. Especially the volume close to the surface of the electrodes needs to be tested with electrons of all angles, as small misalignments in this region strongly affect the shape of the transmission function (see section 4.1 for further information). Therefore, the diameter of the beam needs to be small, as otherwise an observed deviation from the ideal spectrum may be due to several causes, which cannot

be distinguished in the analysis.

In order to be able to deconvolve it from the measured spectrum, the electron beam energy should be quasi-monoenergetic. The angular distribution should also be well known as it is needed for simulations.

The β -emission in the tritium source is isotropic and the angles are transformed on the way to the entrance of the spectrometer according to the relation

$$\frac{B_{source}}{B_{entrance}} = \frac{\sin^2 \Theta_{source}}{\sin^2 \Theta_{entrance}}$$

based on the conservation of the adiabatic constant (see equation 2.5). An ideal electron source would mimic the angular spectrum expected for a tritium measurement, thus simulating the transmission expected for the real measurement.

For an isotropic source the number of particles dN emitted into the angular segment $d\Theta$ is

$$\frac{dN}{d\Theta} \propto \sin \Theta. \quad (5.1)$$

In the next sections the electron gun of the pre-spectrometer will be discussed. This electron source is based on the photoelectric effect. Several more sources with different emission mechanisms and properties are developed for the KATRIN experiment, fulfilling different purposes. For calibration, an atomic or nuclear standard is needed. Therefore, a ^{83m}Kr source is being developed in Münster [Ost08] and a solid $^{83}\text{Rb}/^{83m}\text{Kr}$ source in Prague [Zbo06]. A Penning trap electron gun is being developed for ultra precision energy beams at MIT [For07].

5.2 The pre-spectrometer electron gun setup

The main component of the pre-spectrometer electron gun is a gold-plated quartz tip with a radius of $r = 1$ mm (see figure 5.3).

Electrons are emitted from the gold layer by means of the photoelectric effect. UV radiation is supplied by a deuterium lamp with a wavelength spectrum in the range of $185 \text{ nm} < \lambda < 400 \text{ nm}$ ($6.7 \text{ eV} > E > 3.1 \text{ eV}$) [Ham]. The quartz tip is transparent to light of the wavelength $150 \text{ nm} < \lambda < 4000 \text{ nm}$ [Pyr], thus not cutting into the UV-spectrum of the deuterium lamp. The work function of gold was measured to be $(4.83 \pm 0.02) \text{ eV}$ ². Therefore, only electrons with excess energies of up to $E_{max} = 6.7 \text{ eV} - 4.83 \text{ eV} = 1.87 \text{ eV}$ can be released. The effective energy spectrum of the electrons is a convolution of the energy distribution of the UV photons between 4.83 eV and 6.7 eV. As the exact spectrum of the deuterium lamp is not known, the accurate energy distribution of the electron cannot be determined and is not part of the studies described here.

The electron gun tip is placed at a high negative potential, thus accelerating the emitted electrons towards the pre-spectrometer. A lens on ground potential focuses the electron beam. The main components of the electron gun system are also shown in figure 5.4.

²Measurements of the gold work function state different values, this was taken from reference [And59]

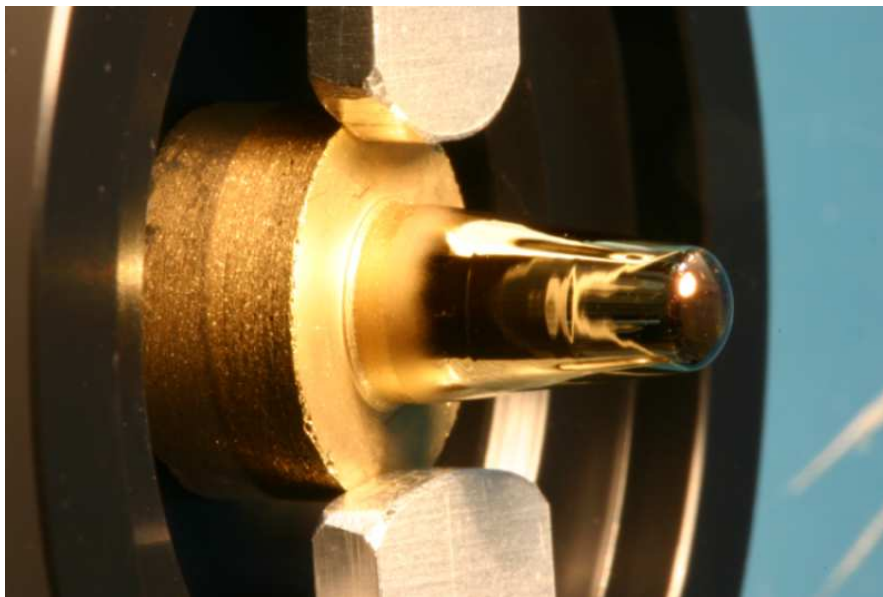


Figure 5.3: A gold-plated electron gun tip

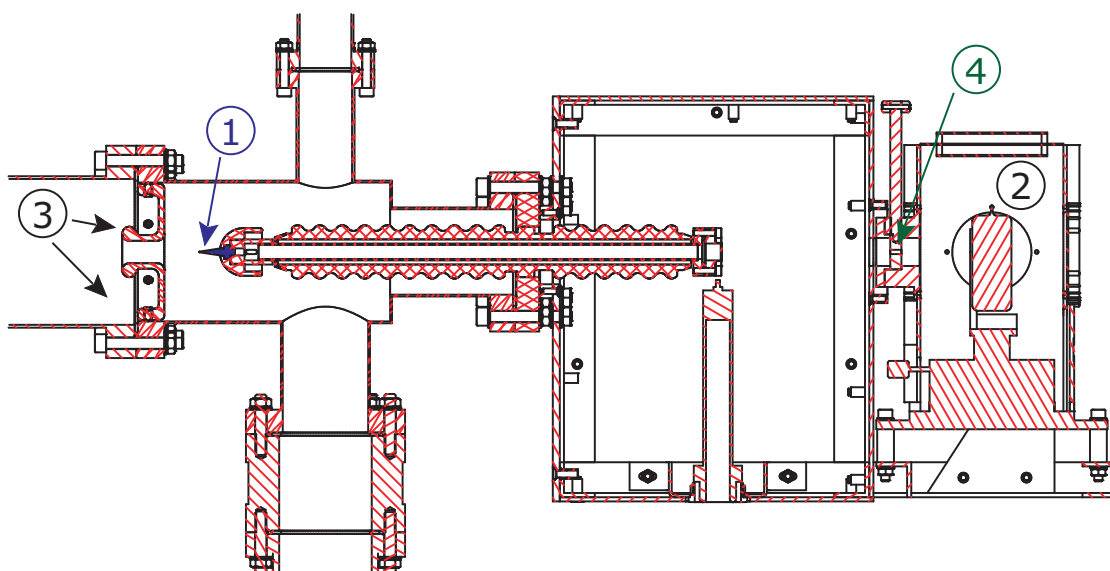


Figure 5.4: Main components of the pre-spectrometer electron gun: 1. electron gun tip, 2. deuterium lamp, 3. electrostatic focusing lens on ground potential and 4. shutter system

During the first measurements with the electron gun setup, it was realised that the area emitting the electrons is very small. In addition to the small spot size the direction of emission is very narrow. This leads to several questions:

-
1. What is the angular emission of the photo-electron gun?
 2. How do the electrons reach the magnet? Is the transport adiabatic?
 3. Can the emission be simulated in order to understand the pre-spectrometer transmission completely?
 4. What is the optimum position of the electrostatic lens?
 5. What is the influence of the special shape of the tip?

In the next sections simulations that answer questions (1) to (3) are discussed. A detailed description of simulations concerning question (5) can be found in reference [Fra07].

5.3 Simulations of the electron gun emission

The programming package *elcd3_2* and the microscopic tracking routine *traj.c* were used for this simulation (see chapter 3 for a detailed description of the programs). The first step was to prepare a geometry suitable for the purpose of the simulation. In order to be able to make statements about the emission characteristics, a systematic analysis has to be carried out. A comparison with real measurements was done after determining the characteristics of the different parts contributing to the transmission function.

5.3.1 Geometry

The aim of these simulations is to understand the emission characteristics of the electron gun. Therefore, electron tracks need to be simulated from the electron gun tip to the entrance of the pre-spectrometer, located at the center of the first magnet at $z = -2.15$ m. The energy range with which the electrons leave the gold surface is known. However it is not possible to start electrons directly on the surface, as the boundary element method is used to calculate the surface charge densities (see section 3.2). As the distance to the electrode surface, in which the potential can be calculated with good accuracy, is also dependent on the discretisation of the surface, the tip of the electron gun needs to be subdivided into very small pieces. The input for the programs consists of polygons. Therefore, the spherical form of the tip has to be approximated. A good approximation is important, since the electric field is strongly influenced by edges (see figure 5.5 for illustration).

The electric potential is different for the two cases when it is either calculated close to the middle of a polygon or close to the edge. To reduce systematic errors, only starting positions in front of the center of line elements are used.

Tests have shown that at a distance of 10^{-8} m to the electrode surface a good accuracy of the potential calculation is given.

To ensure an approximately round surface, the round part of the tip with $r = 1$ mm is subdivided into 1000 elements. For each subelement, the starting position is calculated and stored into a script with which the tracking routine can be started directly.

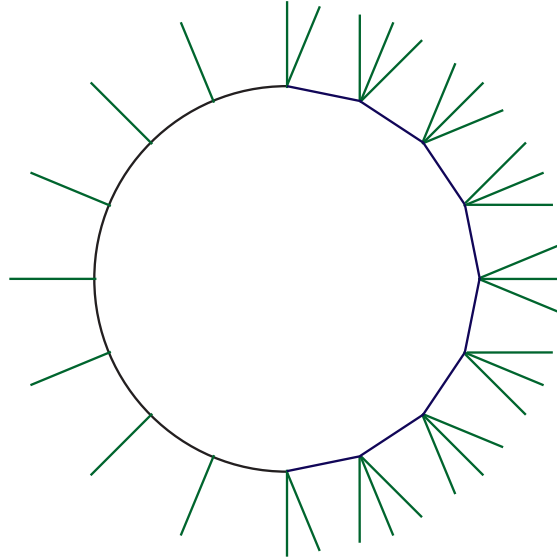


Figure 5.5: Electric field lines for a circle and a polyangular geometry. The electric field lines stand perpendicular to the surface. If a spherical surface is approximated with polygons, the edges cause a rise in field strength. In addition, the electric potential close to the polygons is not consistent with that of a sphere. In order to minimise such discretisation effects, the electrons are only started in front of the middle of a linear segment to avoid systematic errors.

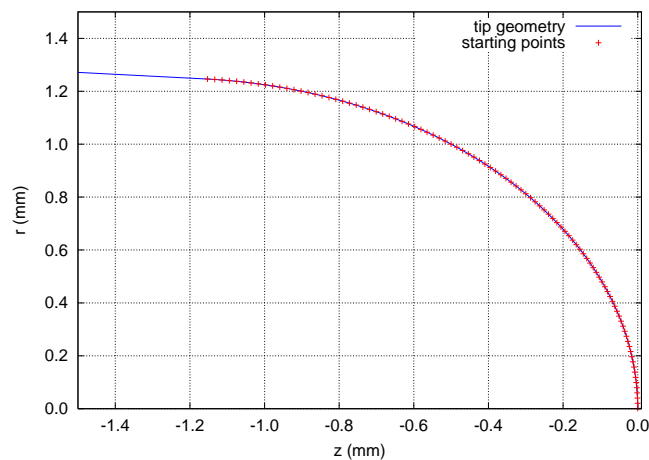
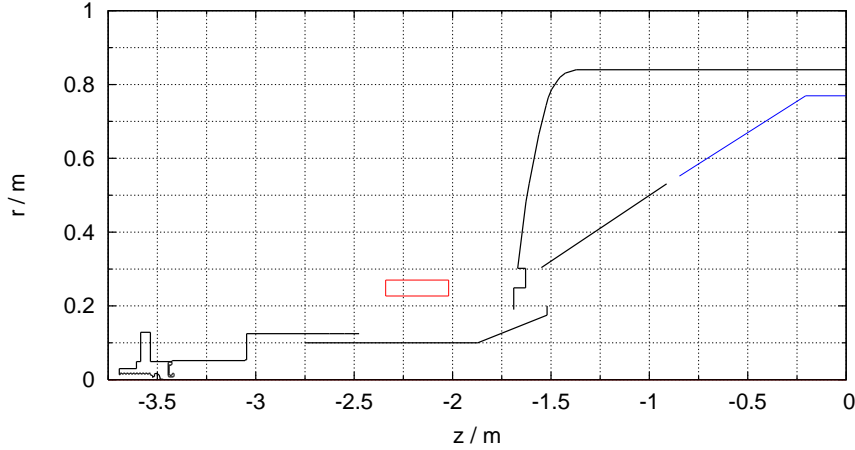


Figure 5.6: Schematic sketch of the egun tip with the starting points.

The approximated tip and the resulting starting points are shown in figure 5.6. The relevant parts of the electron gun setup and the pre-spectrometer are implemented in an input file for *elcd3_2* calculations (see also figure 5.7).

To keep the calculation time low, rotational symmetry is used and the setup is mirrored

Figure 5.7: Electron gun setup for *elcd3_2*

at $z = 0.0$ m. This does not influence the accuracy of the computation, as the entrance region between electron gun and first magnet in the setup is sufficiently far away from the exit region.

5.3.2 Tracking the electrons from tip to magnet

As the exact energy distribution is not known, test electrons were started with discrete excess energies of 0.0 eV, 0.5 eV, 1.0 eV and 1.5 eV to see the effect of the starting energy on the electron tracks. The starting angle between magnetic field and the momentum of the electron is set to zero. This does not adversely affect the conclusions of the simulation because the electron motion in the earliest phase is only determined by the electric field. The angle Θ starts becoming relevant at the point the magnetic field takes over the guidance of the electron. The motion of the electrons was tracked to the center of the entrance magnet. An example track can be seen in figure 5.8.

In the region close to the tip, the motion of an electron is not adiabatic. This region is very small (see figures 5.8 and 5.9). Only after the electrons are accelerated to their maximum transversal energy, the magnetic moment is conserved. In the stronger magnetic field, the gyration radius decreases and the frequency of the motion rises (see figure 5.8). The longitudinal energy E_{\parallel} of the electrons is converted into transversal energy E_{\perp} due to the adiabaticity of the motion (see figure 5.9 and for an explanation of adiabaticity section 2.2 in which the principle of the MAC-E filter is explained).

The angle Θ between the magnetic field and the momentum of the electrons rises with the increase of transversal energy. If the longitudinal energy goes to zero, corresponding to

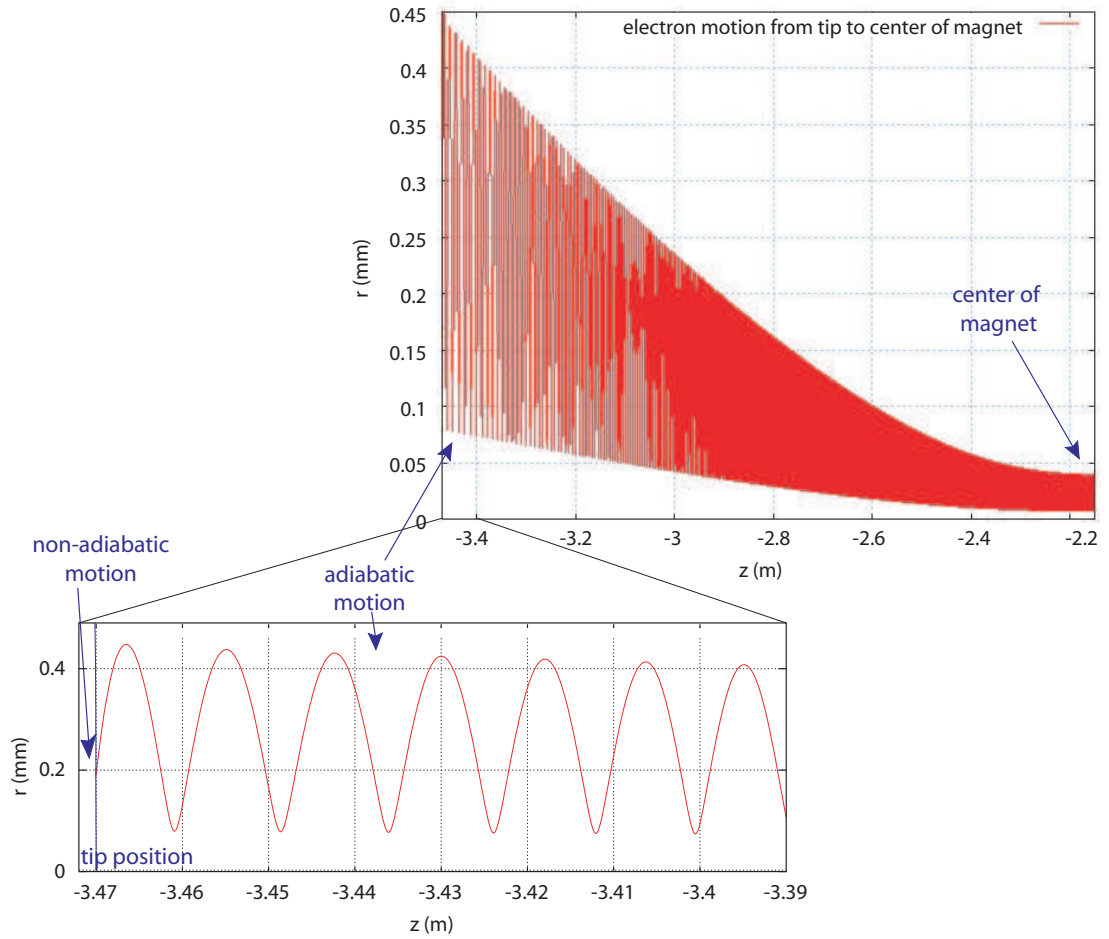


Figure 5.8: Path of an electron from the electron gun tip to the center of the entrance magnet

angles $\Theta \geq 90^\circ$, the electrons are reflected back. An example plot showing longitudinal energy vs z position for a reflected electron can be seen in figure 5.10.

Analysing the electrons reaching the center of the magnet, a dependency between the final angle Θ and the starting radius is obvious (see figure 5.11).

The angular dependency on the radius can be explained by the arrangement of the electric and magnetic field with respect to each other. Located close to the electrode surfaces, the electrons are radially accelerated away from it along the electric field lines. On the scales considered here, the magnetic field lines can be assumed to be almost parallel. Therefore, the electrons on their tracks perpendicular to the spherical surface have larger angles with respect to the magnetic field if their emission point is located at higher starting radii r (see also figure 5.12)

$$\Theta_{start}(r) = \arcsin \frac{r}{R}, \quad (5.2)$$

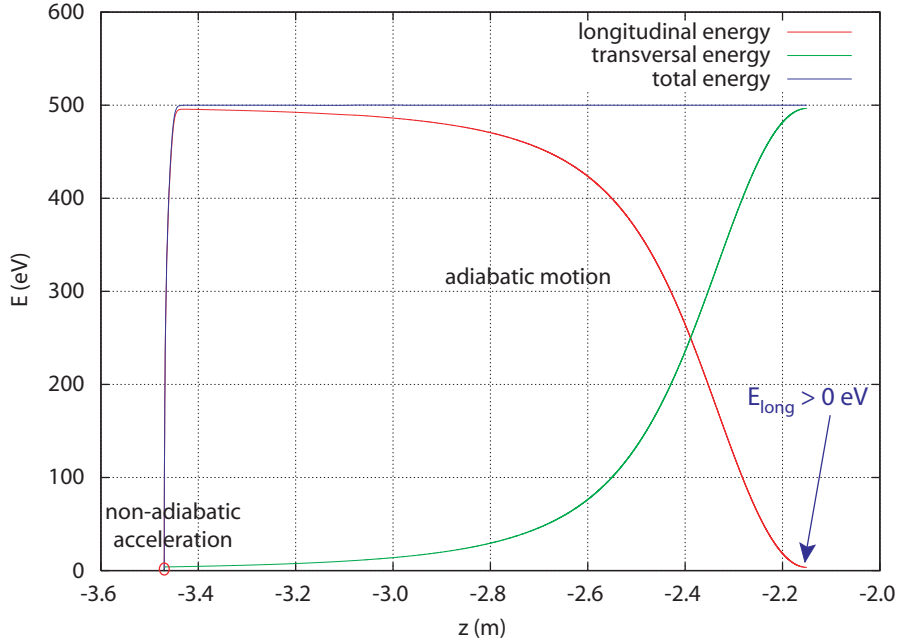


Figure 5.9: Longitudinal, transversal and total kinetic energy for an electron starting at the electron gun tip just reaching the center of the entrance magnet. The electron is first accelerated to an energy of $E = qU_{egun}$, in this case with an acceleration voltage of $U_{egun} = 500$ V. With the increase of the magnetic field B , longitudinal energy is transformed into transversal energy.

with $R = 1$ mm the radius of the tip.

The angle is not only determined by the starting point however, because the acceleration through the electric field is not instantaneous. This can be seen in figure 5.13, in which the starting angle is correlated to the radial emission point. The red line denotes the starting angle Θ_{start} calculated from the angle Θ in the magnet with the magnetic field ratio between electron gun tip and center of magnet under the assumption that the motion is adiabatic (see equation (5.1)):

$$\Theta_{start} = \arcsin \sqrt{\sin^2 \Theta \frac{B_{egun}}{B_{mag}}}.$$

The green line shows the theoretically expected angular emission if no magnetic field is present. The electron moves radially from the surface, following the electric field lines. As these curves do not coincide, the electrons are already guided magnetically, before they have their full energy. If they move in cyclotron motions around the magnetic field lines, the electrons can only gain longitudinal energy, as the gain and loss of transversal energy will add up over a gyration.

The electron motion close to the tip can thus be described in three main steps:

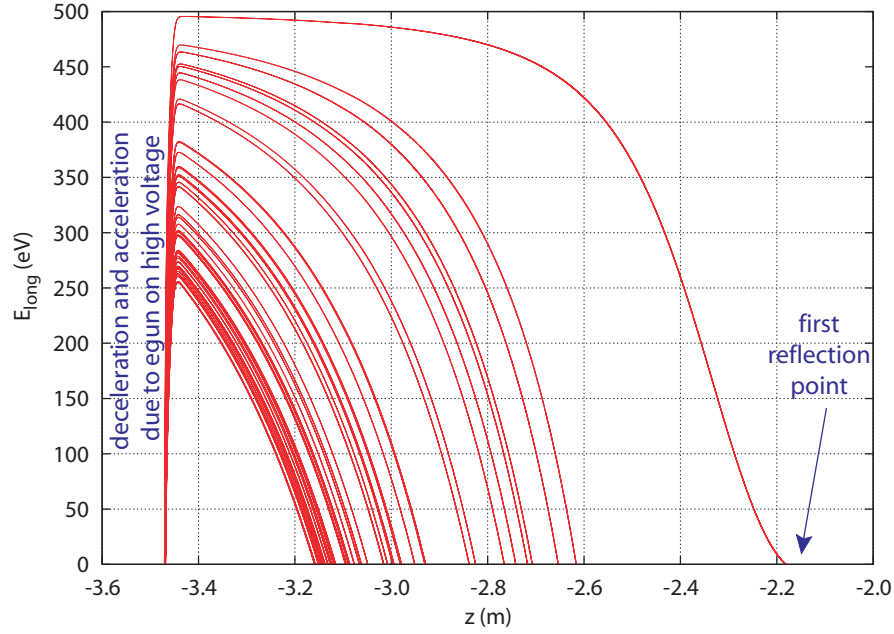


Figure 5.10: Longitudinal energy for an electron starting at the electron gun tip stored in the area between magnet and tip. The electron is started at a radius 0.002 mm larger than that of the electron shown in figure 5.9 that passes the filter. This shows that there is a cut-off value for the allowed starting radius of electrons. The plot shows the longitudinal energy of the electron. After the first reflection close to the maximum magnetic field, the electron is stored between tip and magnet. The voltage on the tip decelerates and re-accelerates the electron. In the reflection process the angle Θ is steepened. The magnetic reflection therefore occurs earlier confining the electron to a smaller volume in space. The region in front of the tip forms an electron trap, confining electrons with large angles.

- When being emitted from the tip the electron has a neglectable energy, $E \approx 0.0 \text{ eV}$. Thus, it is not guided magnetically, but only follows the electric field lines.
- The electron is accelerated by the electric field. If it is emitted with an angle $\Theta_{start} \neq 0.0^\circ$, it gains transversal energy. The electron is then guided magnetically in a cyclotron motion.
- If the electron is guided magnetically, it will not be accelerated any more by the electric field³, as over a cyclotron motion, energy gain and loss average to zero. Thus, from here on the transversal component E_\perp is fixed.

For the described setup only electrons with a starting radius r_s smaller than $r_s = 0.16 \text{ mm}$ reached the center of the entrance magnet. The maximum allowed starting radius r_s slightly depends on the starting energy, as can be seen in table 5.1.

³neglecting magnetron drift

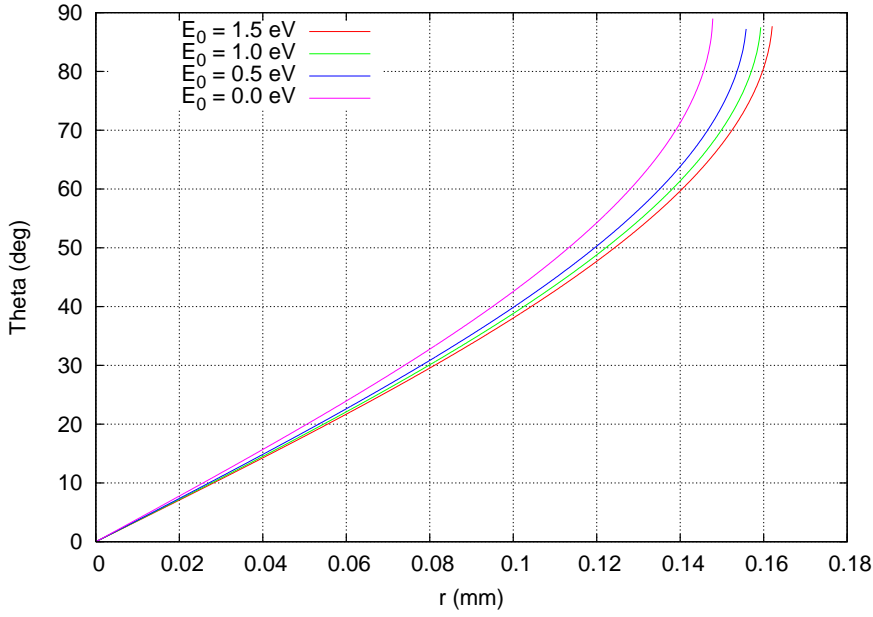


Figure 5.11: Dependency of the angle Θ in the center of the magnet on the starting radius at the tip. The four threads in this graph are results of the four different starting energies 0.0 eV, 0.5 eV, 1.0 eV and 1.5 eV. The plot shows that $\Theta = 90^\circ$ is not reached. This is an artefact of the discretisation. At high angles the slope of the curve is steep. The last 10° are emitted in an r range of $\Delta r = 0.002$ mm. The spacing between the starting points is approximately equidistant in r . Therefore, the simulation just does not include electrons with angles close to 90° . This figure shows the result of a simulation with $U_{egun} = -1$ kV and $B_{mag} = 0.283$ T.

The energy of the electrons at the center of the entrance magnet $z = -2.15$ m is constant for the same starting kinetic energy. The energy spread of the electron beam will be small, as the starting kinetic energy distribution is small due to the narrow excess energy of the UV photons with regard to the work function of gold. Thus we can expect a beam with an energy of

$$qU_{egun} < E < qU_{egun} + 1.87 \text{ eV} \quad (5.3)$$

with a form derived from the emission spectrum of the UV lamp.

The angular dependence on the starting radius simulated for one electrons per radial position can be seen in figure 5.11 (this result was first presented in reference [Val06]). In order to transfer the results of these single electron simulations with a geometry approximated by 2-dimensional polygons to a quasi continuous spectrum emitted by a 3-dimensional structure, several assumptions have been made.

As the simulations show that only a very small part of the sphere ($r \in [-0.2 \text{ mm}, 0.2 \text{ mm}]$) emits electrons that can reach the entrance magnet of the pre-spectrometer, this part can be approximated by a disk with radius r . From the simulations, the final angle

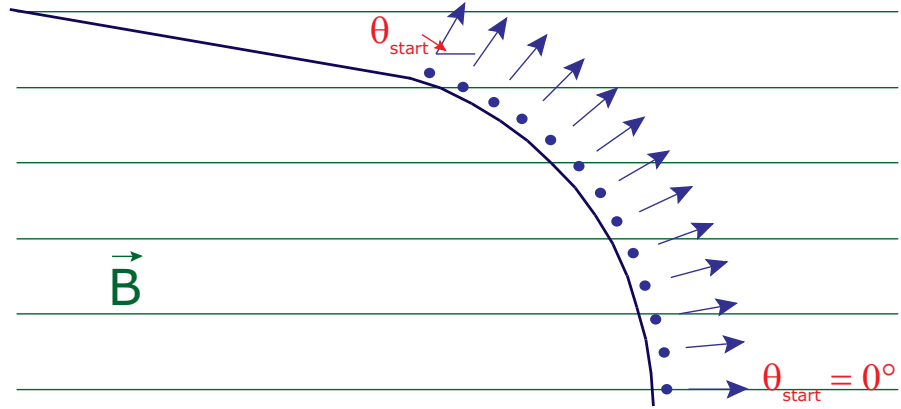


Figure 5.12: Schematic example illustrating the angular dependency of the emission point

Table 5.1: Maximum starting radius of electrons reaching the center of the entrance magnet in dependence of the starting kinetic energy for an acceleration voltage of $U_0 = 1$ kV

starting energy E_s in eV	maximum starting radius r_s in mm
0.0	0.148
0.5	0.156
1.0	0.159
1.5	0.162

Θ at the center of the magnet is known for discrete values of r . To approximate the angular distribution, it is assumed that all electrons emitted with a radius r between $r_i < r < r_{i+1}$ have the same angle as the electron simulated with r_{i+1} . In addition to that, an arbitrary unit area F has been chosen, on which the number of electrons emitted is assumed to be one. The number of electrons emitted with the angle $\Theta(r_{i+1})$ is equal to

$$N(r_{i+1}) = \frac{\pi(r_{i+1}^2 - r_i^2)}{F}. \quad (5.4)$$

Normalizing the electron distribution for an electron gun potential of $U_{egun} = -1000$ V and a magnetic field of $B_{mag} = 0.283$ T at the center of the magnet⁴ with the area $F = 2.56 \mu\text{m}^2$, a distribution including all angles is seen in the pre-spectrometer entrance magnet (see also figure 5.15).

These simulations show that the pre-spectrometer electron gun does not fulfil all requirements posed on a calibration tool for a MAC-E filter.

⁴This analysis has not been done for the nominal magnetic field, but for $B_{mag} = 0.283$ T, as test measurements have been conducted with fields of this value.

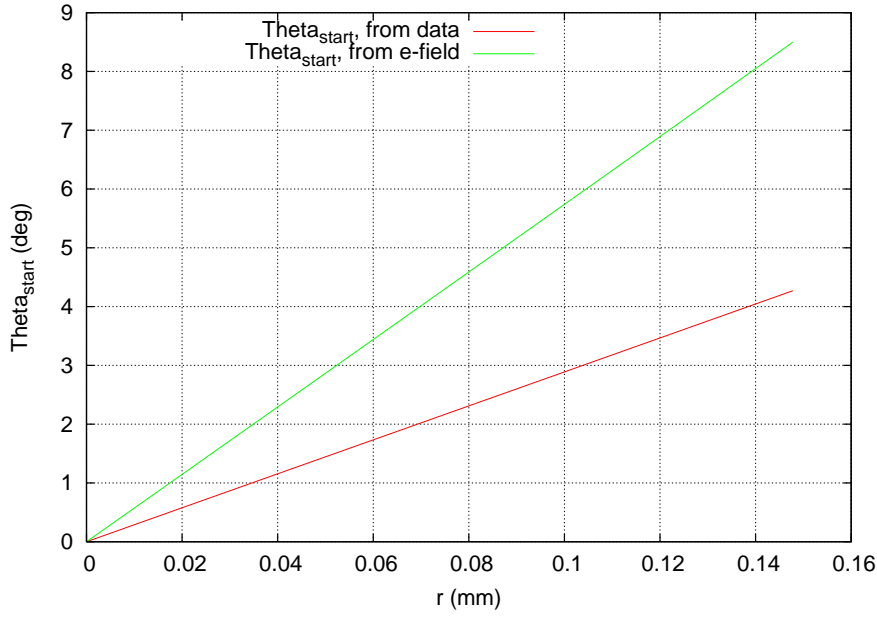


Figure 5.13: Starting angle at the electron gun tip calculated with different models. The red line is computed with the angle the electron has in the magnet under the assumption that energy is transformed adiabatically for an acceleration voltage of $U_{e-gun} = -1000$ V. The green line denotes the theoretical angle to the z -axis expected if only an electric field is applied.

5.3.3 General analysis

To test the accuracy of these simulations, the results have been compared to a real measurement done at the pre-spectrometer.

The measurement 1000S of the transmission function is described in detail in reference [Fra06]. A potential of (-950 ± 4) V was applied to the vessel hull⁵ and the wire electrode was connected to (-999.8 ± 0.6) V to screen electrons emitted from the vessel material. The central magnetic field of the solenoids was 0.283 T. For the measurement, the voltage applied to the egun was varied from (-990.7 ± 0.6) V to (-1005 ± 0.6) V in steps of 1.1 V. The voltage applied on the electrodes had a 50 Hz noise mainly of sinusoidal shape and a peak-to-peak value of 1.5 V. The measured response function is shown in figure 5.16. A measured response function is a convolution of the transmission of the different components:

- angular and energy emittance of the source,
- transport efficiency⁶,

⁵The error denotes the uncertainty of the applied voltage, not its instability during the measurement.

⁶If a transport section like the DPS and CPS (see section 2.3) is located between source and spectrometer- for the pre-spectrometer the electron gun is mounted directly to the spectrometer, therefore no transport efficiency has to be taken into account.

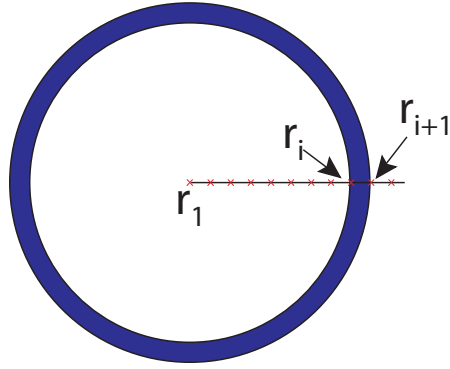


Figure 5.14: Sketch illustrating the conversion from electrons emitted from a line to emission from an area.

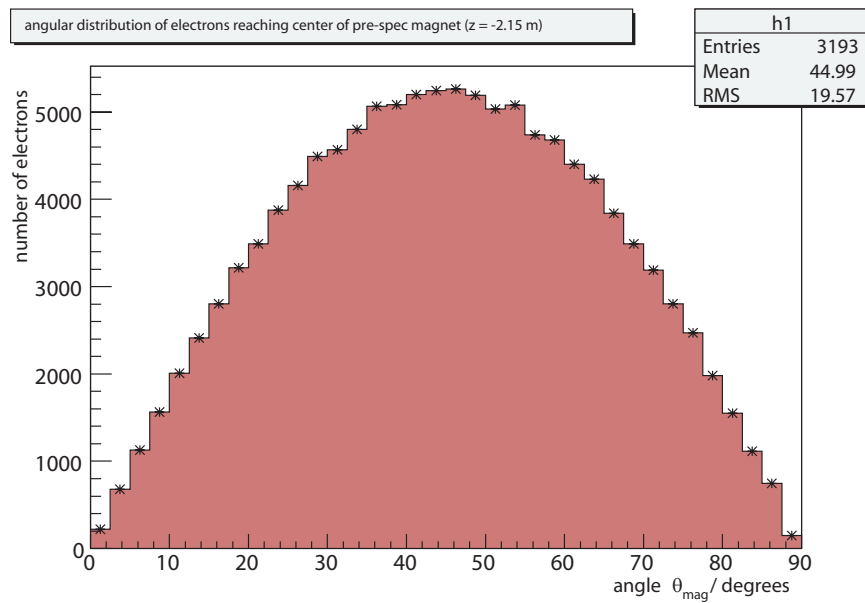


Figure 5.15: Angular distribution of beam electrons at the center of the entrance magnet

- spectrometer transmission⁷ and
- detector efficiency.

Its composition is illustrated in figure 5.17.

At the pre-spectrometer, it is a convolution of the following components:

$$f_{res} = T(U_{egun}, U_0) \otimes \delta E_{source}(U_{egun}) \otimes N(E_{source}, \Theta_{mag}) \otimes \delta U \otimes f_{det}, \quad (5.5)$$

⁷The spectrometer efficiency can be separated into a theoretical transmission function and fluctuations on the potential.

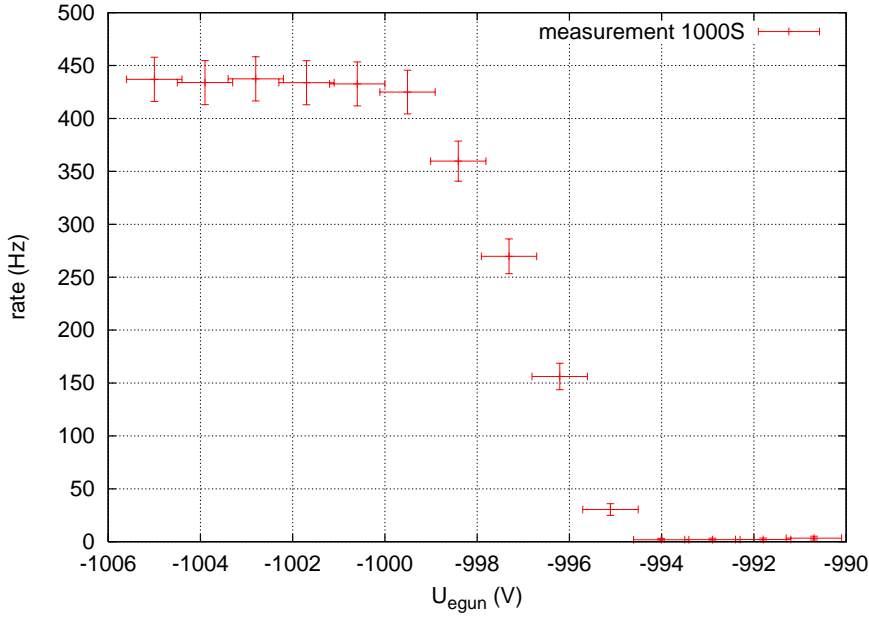


Figure 5.16: Measured response function at the pre-spectrometer for a retardation voltage of 1 kV and an applied magnetic field of 0.283 T inside the magnets.

where f_{res} is the response function, $T(U_0, U_{egun})$ the transmission function of the pre-spectrometer, $\delta E_{source}(U_{egun})$ the energy distribution of the source, $N(E_{source}, \Theta_{mag})$ the relative intensity of the source in dependance of the energy and emittance angle, δU the voltage stability and f_{det} the detector efficiency function. As these functions are all known, we can calculate the expected width of the transmission function.

The width of the transmission function T alone is given by the magnetic field ratio (see equation (2.6)). For a measurement with 1 kV acceleration voltage, a width of

$$\Delta E = \frac{B_{min}}{B_{max}} E_0 = \frac{0.02 \text{ T}}{4.5 \text{ T}} 1 \text{ keV} = 4.44 \text{ eV} \quad (5.6)$$

is expected for an on-axis beam. The energy distribution of the source has a width of 1.87 eV with unknown shape. The 50 Hz noise on the potential during the measurement 1000S could be described by a sine wave with a peak-to-peak value of 1.5 V:

$$\delta U = U_0 \sin(\omega t) \approx 0.75 \text{ V} \sin(2\pi \cdot 50 \text{ Hz} \cdot t). \quad (5.7)$$

For this considerations, the detector efficiency function is negligible. Assuming the source function has box form, all distributions have a finite width and will result to a total width of $\Delta U \approx 7 \text{ V}$.

The energy emittance of the source is known to lie in the range $[qU_0, qU_0 + 1.87 \text{ eV}]$. The angular emittance has been derived in the previous section. The result has to be convolved with the transmission of the pre-spectrometer for the different voltages applied to the electron gun. As the simulation of an angular distribution for each potential is

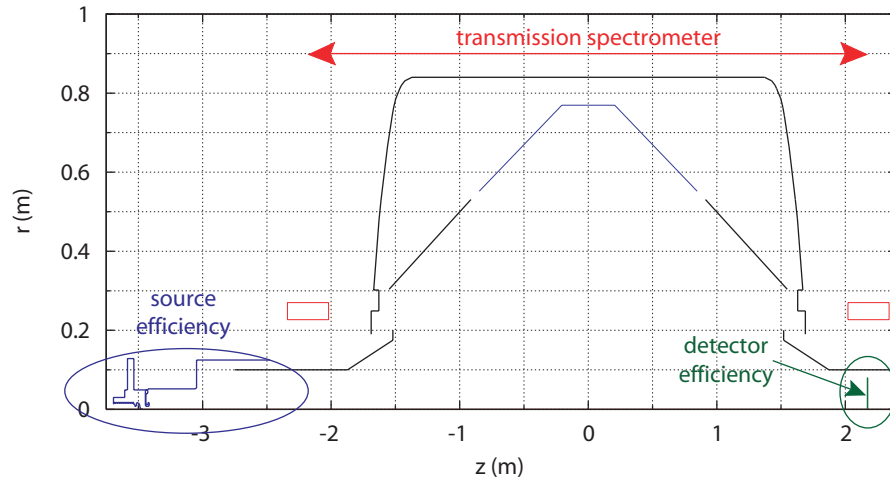


Figure 5.17: The total transmission function is a convolution of the efficiency of the different components, in this setup the source efficiency, the transmission of the spectrometer and the detector efficiency

not practical, the convolution is approached in a different way:

The maximum retarding voltage for an electron with fixed energy and angle to pass the filter is calculated based on the angular distribution inside the entrance magnet. All electrons with smaller angles and the same energy will also pass the spectrometer and will therefore be added to the intensity of the transmission at the exit of the pre-spectrometer. The analytical form of the transmission as a function of the initial angle Θ has been derived in section 2.2, equation (2.9):

$$U_{ret} < \frac{E_{tot}^{kin}}{q} \left(1 - \frac{B_{ana}}{B_{mag}} \sin^2 \Theta_{mag} \right).$$

With equation (2.9) we can determine at which potentials U_{ret} electrons with a certain angle Θ_{mag} and starting energy

$$E_{tot}^{kin} = E_{start} + qU_0 \quad (5.8)$$

pass.

The transmission functions calculated for the angular distribution derived in the previous section have the same width $\Delta U = 4.44$ V for electrons with various starting energy values given by the magnetic field ratio (see also figure 5.18). To take into account the energy distribution of the electron beam, the transmitted electrons calculated for each starting energy are added up to form the total spectrum. This is shown in figure 5.19. The resulting transmission function is spread out and has a width of $\Delta U_{0\% \rightarrow 100\%} = 5.94$ V.

The detection efficiency of the micro channel plate (short MCP) used for this transmission function measurement is dependent on the incident angle. It is positioned perpen-

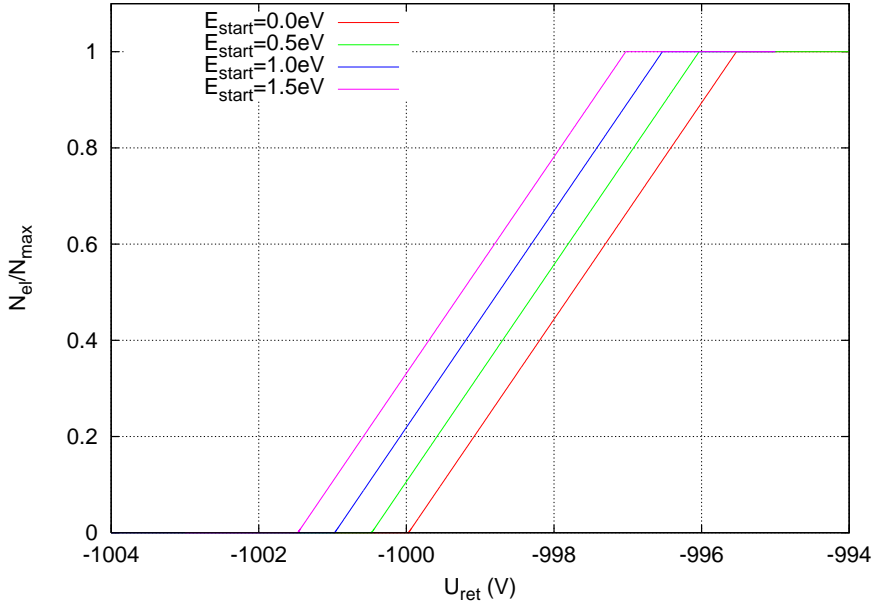


Figure 5.18: Transmission functions calculated with equation (2.9) for different starting energies E_{start}

dicularly to the beam at 200 mm from the middle of the exit magnet. The magnetic field strength decreases at this point to 44% of the nominal field in the magnet. Therefore, the angular distribution at the magnet has to be adjusted for the decrease of the magnetic field strength with the relation

$$\frac{B_{mag}}{B_{det}} = \frac{\sin^2 \Theta_{mag}}{\sin^2 \Theta_{det}}. \quad (5.9)$$

The distribution therefore is cut off at the angle

$$\Theta_{det} = \arcsin \left(\sin \Theta_{mag,max} \sqrt{\frac{B_{det}}{B_{mag}}} \right) = 41.55^\circ.$$

It is shown in figure 5.20.

An MCP efficiency measurement can be seen in figure 5.21⁸. A polynomial of seventh order is fitted to the data:

$$\begin{aligned} f(\Theta) = & (4 \pm 7) \cdot 10^{-11} \cdot \Theta^7 - (1.9 \pm 2.1) \cdot 10^{-8} \cdot \Theta^6 + (3.5 \pm 2.6) \cdot 10^{-6} \cdot \Theta^5 \\ & - (3.4 \pm 1.6) \cdot 10^{-4} \cdot \Theta^4 + (1.9 \pm 0.5) \cdot 10^{-2} \cdot \Theta^3 - (0.63 \pm 0.08) \cdot \Theta^2 \\ & + (9.8 \pm 0.5) \cdot \Theta + (46.8 \pm 1.1). \end{aligned}$$

Correcting the rate for the detector efficiency does not affect the width of the transmission function, but its slope (see figure 5.22).

⁸data taken from [ELOG] entry 83, 06.11.06, M. Steidel, S. Neubauer: Detector Efficiency Weighted by Electron Angle Distribution

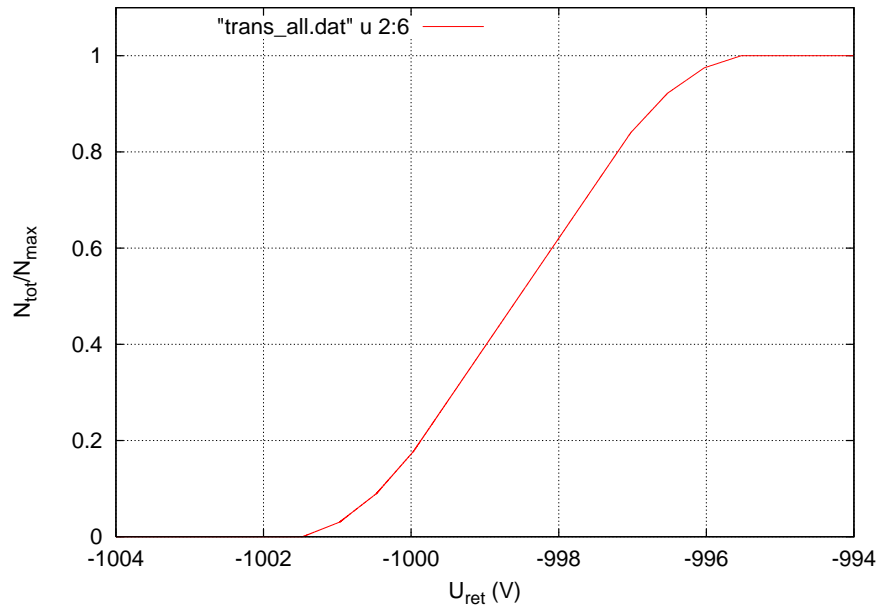


Figure 5.19: Transmission function for all energies added up

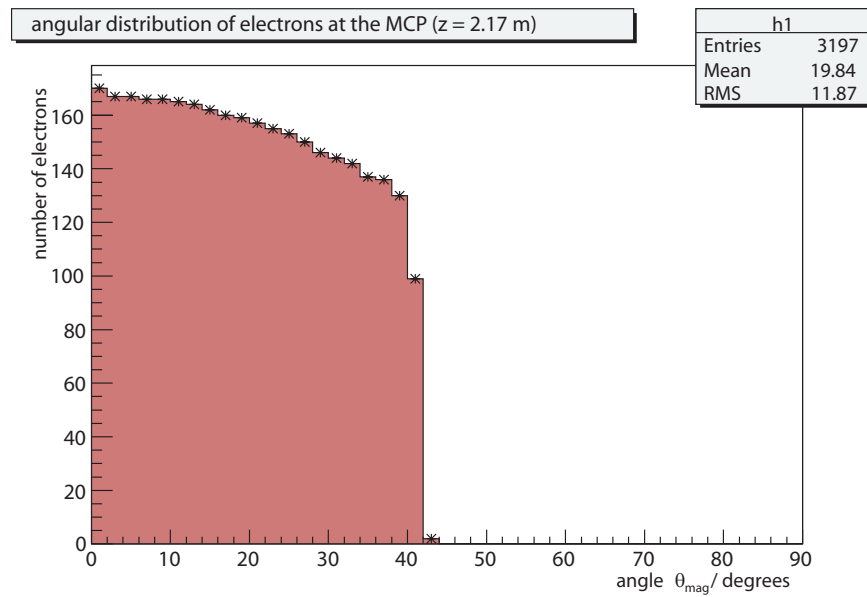


Figure 5.20: Angular distribution of electrons reaching the MCP

The measured and simulated transmission function should have the same width and therefore only differ in the sign of the slope. The simulated function only gives relative values and therefore has to be normalized according to the measured data. The count rate is adjusted to match the measured maximum countrate $N = 435$ Hz. Before su-

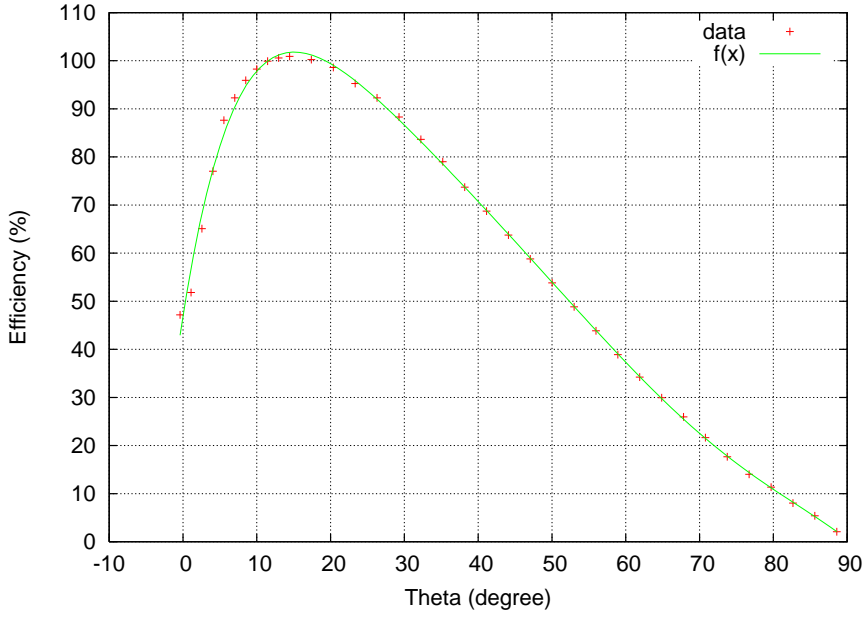


Figure 5.21: Measured MCP efficiency fitted with a polynomial of seventh order

perimposing the two transmission functions, the simulated retarding potential U_{ret} is converted into the e-gun potential by mirroring, and adjusted to the measurement by calibration with the point $U_{egun} = U_{ret}$:

$$\begin{aligned}
 U_{egun} &= -1 \cdot U_{ret} + U_{egun=ret,sim} + U_{egun=ret,measured} \\
 &= -U_{ret} - 1001.5 \text{ V} - 994.0 \text{ V} &= -U_{ret} - 1995.5 \text{ V}.
 \end{aligned}$$

The resulting transmission function seems to match the measured one relatively well (see figure 5.23).

To complete the electron gun measurement analysis, the 50 Hz noise with amplitude 0.75 V has to be taken into account. Therefore the starting energy E_{tot} in formula (2.9) will be convolved with the function $\delta U = 0.75 \text{ V} \cdot \sin(2\pi \cdot 50 \text{ Hz} \cdot t)$ to approximate the noise contribution.

The width of the transmission function rises to $\Delta U = 7.44 \text{ V}$. As this value also takes into consideration very small deviations that are not measurable in a real experiment, the width is normally given between the values at which the transmission has reached values of 10% and 90% respectively. This gives a width of $\Delta U_{10\% \rightarrow 90\%} = 3.87 \text{ V}$. The superposition of the two curves seems to be very good (see figure 5.24).

5.4 Summary

The simulations of the pre-spectrometer electron gun give evidence of an electron distribution with all angles in the center of the pre-spectrometer entrance magnet. This is

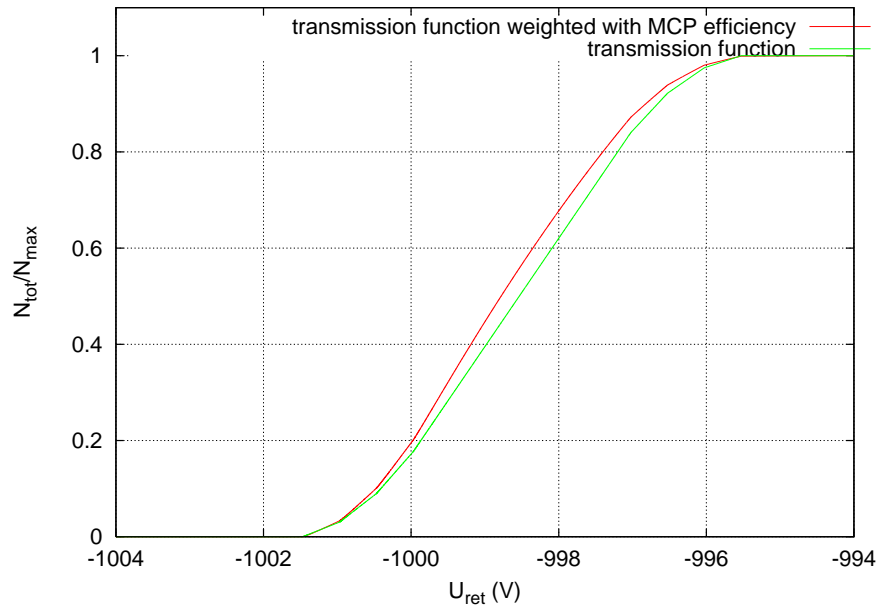


Figure 5.22: Comparison between simulated transmission function weighted with and without MCP efficiency

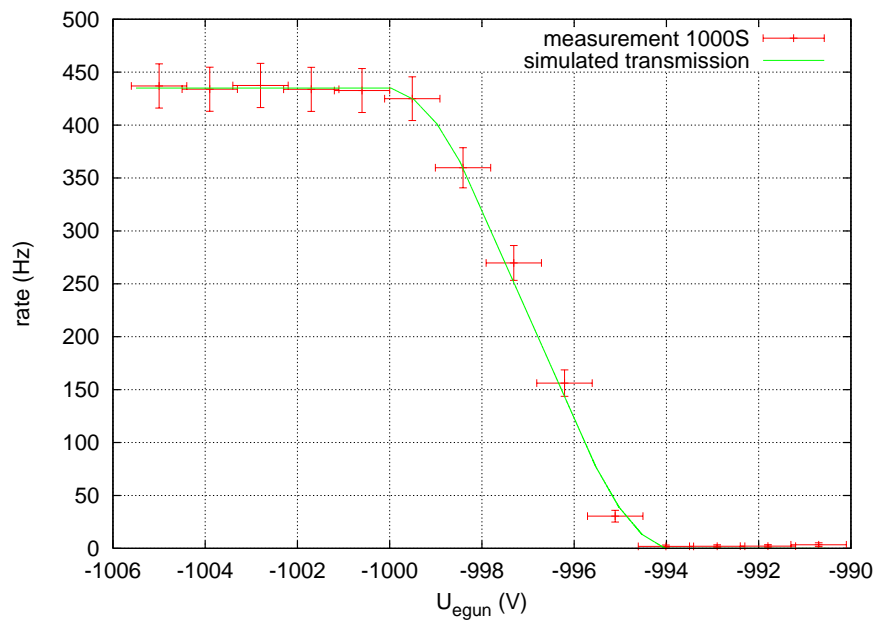


Figure 5.23: Comparison of measured and simulated transmission function. The simulated U_{ret} is adjusted to U_{egun} with the fix point $U_{\text{egun}} = U_{\text{ret}}$ and normalized to the total transmission rate 435 Hz.

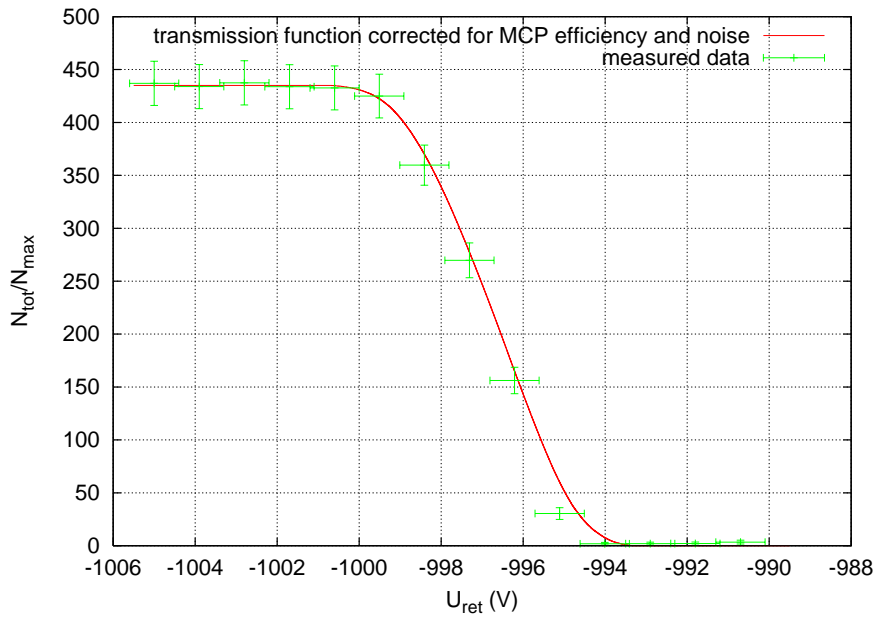


Figure 5.24: Comparison of measured and simulated transmission function, taking into account the noise $U_{noise} = 0.75 \text{ V} \cdot \sin(2\pi \cdot 50 \text{ Hz} \cdot t)$.

supported by a transmission measurement at 1 keV retarding potential which could be reproduced.

As the electron gun only emits a small part of its electrons at high angles, it is not the best calibration source for the main spectrometer. As already mentioned in section 4.1, the high angle electrons of the outer flux tube are the ones most sensitive to displacements of the wire electrode. To be able to test this an isotropic source would offer the best spectrum. A possible source is the condensed Krypton source that is currently being prepared for measurements at the main spectrometer. For details see references [Ost08, Smo08].

6 Discharges and Penning traps

Due to its high precision and stability requirements it is vital for the KATRIN experiment to avoid background sources if possible and to reduce the remaining background to a minimum level. In this chapter an internal background source will be discussed, the electric discharge. It can be caused through different mechanisms. The relevant mechanisms are described in the first section. The importance of these discharges for the KATRIN experiment will be discussed in the second section by showing their impact on the predecessor experiments in Troitsk and Mainz.

First experimental tests at the KATRIN pre-spectrometer revealed electrical discharges. The experiments and their interpretations as well as measures taken to avoid further voltage breakdowns will be discussed in the third section. It is already known that the section between the pre-spectrometer and main spectrometer hosts a Penning trap. A short overview of the actions that will be taken to ensure that this will not lead to an increase in background is given in the fourth section. The last section discusses possible Penning traps in the main spectrometer and gives an overview of possible measures to avoid them.

6.1 Discharge mechanisms

Discharges in vacuum depend strongly on the environmental conditions, e.g. the pressure, the residual gas composition, the strength and shape of the applied electric and magnetic fields. Therefore they can be divided into different types, depending on the main cause of the ignition of the electric discharge. The Townsend discharge occurs in electric fields applied to a system with bad vacuum, whereas vacuum discharges play a role at much lower pressures. The Penning discharge appears in good vacuum in systems with crossed magnetic and electric fields.

6.1.1 Townsend discharge

The Townsend discharge was first explained by J.S. Townsend in 1903. It occurs in an electrode setup without the presence of magnetic fields under rather bad vacuum conditions. If the electric potential applied to the electrodes rises above a critical value – the so-called sparking or breakdown potential – the insulation of the vacuum breaks down and a current passes between the electrodes [Tow10].

The basic process is dependent on the geometry of the setup, the composition of the residual gas and the pressure. Some of the first discharge curves were provided by F. Paschen in 1889. He was the first to state that for all electrode systems the sparking

potential U can be expressed as a function of the pressure p and the distance d between the plates (Paschen's law, see also figure 6.1) [Pas89].

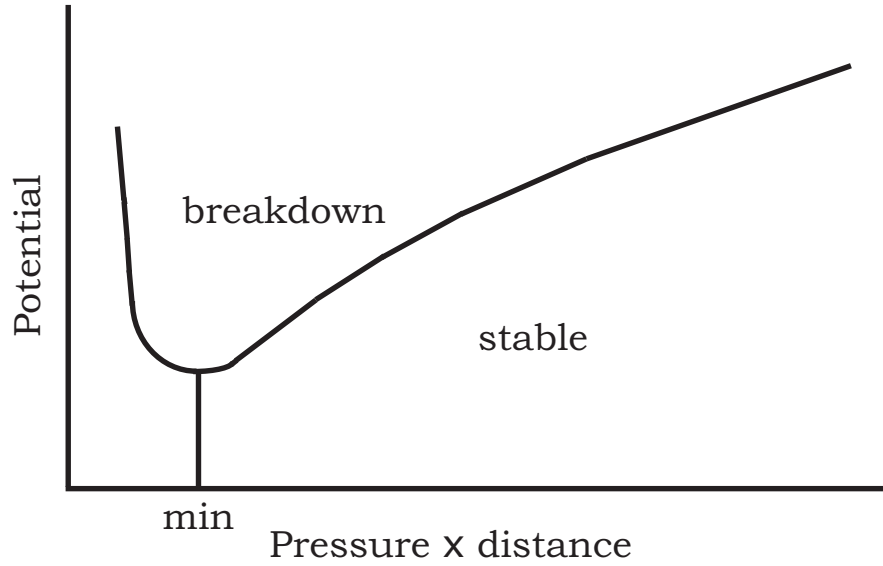


Figure 6.1: The Paschen curve $U(p \cdot d)$: breakdown voltage U in dependence of the product of pressure p and distance d (figure adapted from [Tow10])

The discharge mechanism depends on the number of secondary electrons and positive ions produced by collisions in the gas. If N_{ini} is the number of initial electrons, emitted through radiation and radioactivity from the cathode, the number of electrons at a distance d to the cathode can be expressed in terms of the primary Townsend coefficient α :

$$N(d) = e^{\alpha d} N_{ini}. \quad (6.1)$$

α gives the average number of electron-ion pairs which are produced by one electron, scaled by the distance in the direction of the electric field. It is therefore dependent on the applied potential U and the pressure p as well as properties of the gas. Generally, it can be described by the following expression [Dav06]:

$$\alpha = \begin{cases} A \cdot p e^{-\frac{Bp}{E}} & \text{for } E < E_i \\ \frac{1}{\lambda} & \text{for } E \geq E_i, \end{cases} \quad (6.2)$$

with parameters A and B , which depend on the electric field range and gas type. λ is the mean free path between collisions of the electron with atoms, E_i the electric field needed to accelerate the electrons to gain the ionisation energy on the pathlength λ . In general, the mean free path is defined as

$$\lambda = \frac{1}{n\sigma}, \quad (6.3)$$

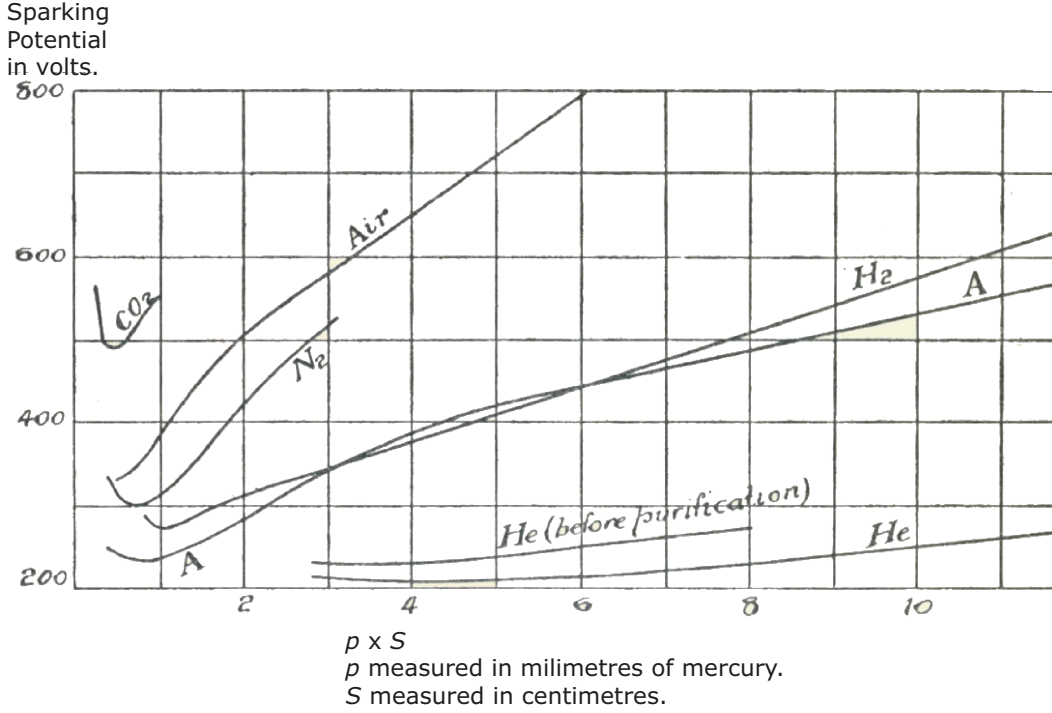


Figure 6.2: The breakdown potential of different gases in dependence of the product of pressures p and electrode spacing S (figure taken from [Tow10])

with n being the number of atoms per unit volume and σ the electron collision cross section with this type of atoms which is energy dependent. α is only dependent on the mean free pathlength, if every collision with an atom is an ionisation collision. If the electrons have one or more elastic collisions between two ionisation processes, the first Townsend coefficient is described by an exponential function.

The ions produced in the collisions are accelerated towards the cathode. Their number $N_+(d)$, after crossing the distance d in direction of the electric field, is equal to

$$N_+(d) = (e^{\alpha d} - 1)N_{ini}. \quad (6.4)$$

Upon collision with the cathode, new electrons are emitted from the surface. The secondary Townsend coefficient γ gives the mean number of new electrons created by one positive ion, thus a total of

$$N_{e,tot} = \gamma(e^{\alpha d} - 1)N_{ini} \quad (6.5)$$

electrons are now available. In order to initiate a steady discharge process, this number has to be at least equal to the number of initial electrons N_{ini} [Tow10, Glu07b]:

$$\gamma(e^{\alpha d} - 1) \geq 1. \quad (6.6)$$

The Paschen curve varies for different gases, as it is dependent on the ionisation energy E_i and the cross section σ . The general relation between the breakdown potential U , the pressure p and the distance d is the same for most gases, as shown in figure 6.2. An important feature is the minimum of the breakdown potential. For low pressure only a few high energy collisions take place in contrast to many low energy collisions for high pressure. This results in a minimum for the sparking potential if on the mean free path length the electron is accelerated to gain just enough energy for an ionising collision. In the KATRIN spectrometer the pressure will be reduced to $\approx 10^{-11}$ mbar. This results in a tiny first Townsend coefficient α . Therefore $\gamma(e^{\alpha d} - 1) \ll 1$ and the Townsend discharge does not occur in the above described form. Nevertheless, the avalanche mechanism was first explained by Townsend and is a fundamental part of the other discharges, which motivated its inclusion in this chapter.

6.1.2 Vacuum breakdown

The vacuum breakdown process takes place in setups with good vacuum, applied electric field and without magnetic field. In this case, therefore, it is not collisions with residual gas molecules that cause the ignition. The surface quality of the electrodes is the determining factor in this discharge process.

For plane electrodes, electrons can be emitted by a tunneling process, also called field emission. The driving force is the applied field strength. The resulting current is described by the Fowler-Nordheim formula [Fow28]:

$$J \propto E^2 e^{-\frac{K}{E}}, \quad (6.7)$$

with K being a constant with the dimensions V/m.

According to this equation, the resulting current should be small for field strengths E below 1 GV/m. However, experiments show, that high currents can be emitted at much lower values. This is due to irregularities on the surface. Micro tips induce a much higher local field strength, leading to the emission of electrons at potential values for which according to theory it should be impossible on smooth surfaces.

Vacuum breakdown generally results in high leakage currents between insulated electrodes and a rise in pressure. As the emission of particles is continuous, this breakdown process does not cause abrupt discharges. The continuous current due to the field emission process can lead to local heating of the surface it hits, thus even melting or evaporating small amounts of material. This process can lead to a leveling of the surface thus ending the discharge again as the field strength is reduced. On the other hand, the evaporation of material can lead to conditions which are favourable for the Townsend discharge.

To avoid vacuum discharges, the surfaces have to be leveled. Electropolishing is advisable for UHV surface preparation as the resulting outgassing rate is lower than for a surface prepared by mechanical polishing. The resulting surface quality is also preferable with regard to high voltage stability.

A possibility to enhance surfaces after implementation into a vacuum system is to condition them. In this process field emission under bad vacuum conditions is used to generate an avalanche mechanism. The emitted electrons ionise atoms that sputter the cathode surface, thus evening out the micro tips. Anode and cathode need to be interchanged to attend to all surfaces. For the Mainz experiment (see also section 6.2.2) voltages of ± 30 kV were applied to the spectrometer for 10-20 min. During this time the pressure was elevated to a level of 10^{-7} mbar [Mue02].

6.1.3 Penning discharge

Systems with good vacuum and crossed magnetic and electric fields can lead to a different type of discharge, the Penning discharge. An example for crossed magnetic and electric field lines can be seen in figure 6.3.

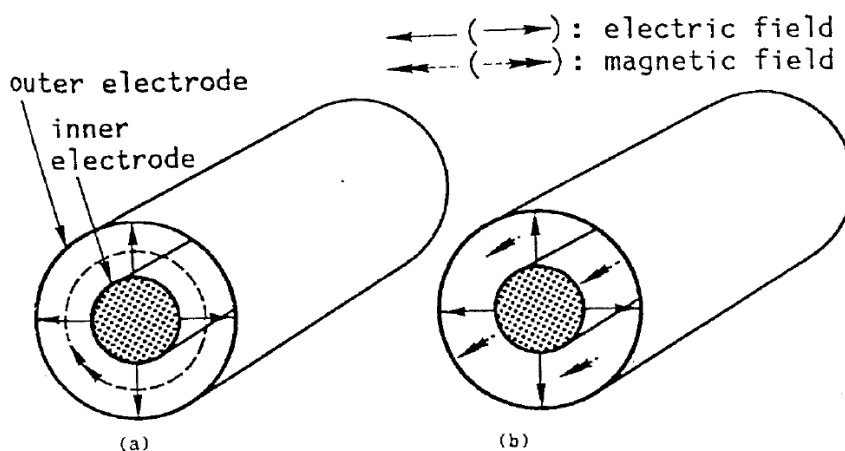


Figure 6.3: Example for crossed magnetic and electric fields in a coaxial cylindrical electrode, a) azimuthal magnetic field, b) axial magnetic field (figure taken from [Har89])

As the storage of electrons is of most interest for the KATRIN experiment, the traps in this section are all explained for negatively charged particles. To make considerations for positive particle traps, cathode and anode have to be interchanged.

For a Penning discharge, the magnetic field needs to be strong enough to ensure a magnetic guidance of the electrons. By guiding the particles on cyclotron tracks, the magnetic field effectively extends their pathlength through the vacuum and therefore increases the collision probability with residual gas (see figure 6.4).

Thus, this breakdown mechanism can be compared to the Townsend discharge, as the magnetic field has a similar effect as an increase of pressure.

Vacuum breakdown processes increase the probability of a Penning discharge as it provides a source of charged particles. At low magnetic field strength the vacuum breakdown even dominates the discharge processes (see figure 6.5), as the field strength is not high enough to guide the particles in small cyclotron motions. The mean free path length λ

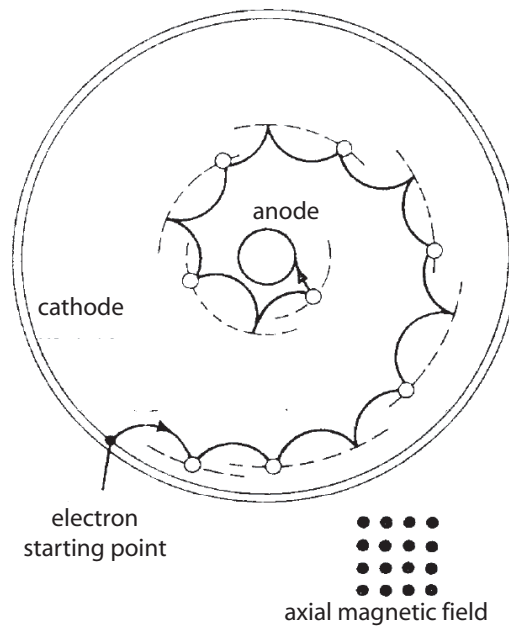


Figure 6.4: Electron motion in a coaxial cylinder with radial electric and axial magnetic field. The total motion can be subdivided into three components: Firstly, the electrons are accelerated from cathode to anode by the electric field. This motion perpendicular to the circular form of the electrodes is overlaid with a cyclotron motion around the field lines resulting in the cycloid motion with the small radius and the magnetron motion responsible for the drift with larger radius (figure taken from [Hae53]).

still exceeds the length of the trajectory, therefore, α is too small to start a Townsend avalanche. For high magnetic field strength the particles are guided in a cyclotron motion around the magnetic field lines. Secondary and field emission provide the primary particles, but the ignition is mostly due to the avalanche mechanism.

For a Penning discharge it is important in which order the magnetic and electric fields are turned on as the B over E curve shows hysteresis for the breakdown potential (see figure 6.5). This is due to the different effects playing a role in the Penning discharge process.

The magnetic and electric fields together can form a particle trap called Penning trap, if the magnetic field lines connect cathode electrodes, but cross inbetween an area with more positive potential (for illustration see figure 6.6). Electrons can be stored in this region, after losing some of their energy through collisions or non-adiabatic energy transformation.

The ignition of a Penning trap is caused by the Townsend avalanche mechanism. Due to the long path length inside the Penning traps ionisation collisions with the residual gas take place. Secondary electrons are created which are also confined in the trap. The positive ions are accelerated towards the cathode and create additional electrons

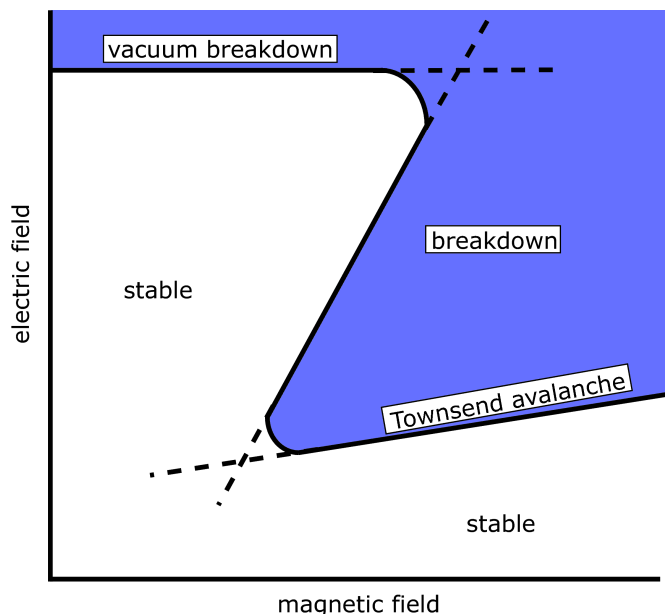


Figure 6.5: Schematic diagram indicating breakdown conditions in dependence of magnetic and electric field for a Penning discharge (figure adapted from [Har89])

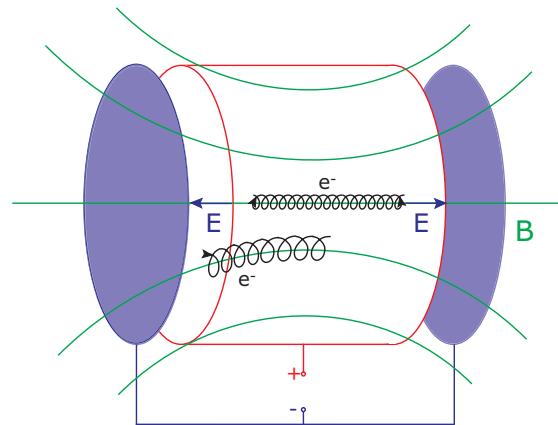
by secondary emission. If the number of secondary electrons is higher than the number of initially trapped electrons, the discharge is self-sustained. This mechanism is quite similar to the Townsend discharge described in section 6.1.1.

If enough electrons are stored in a Penning trap, a plasma can be created. It is negatively charged, as the trapping of positive ions created in collisions is not stable.

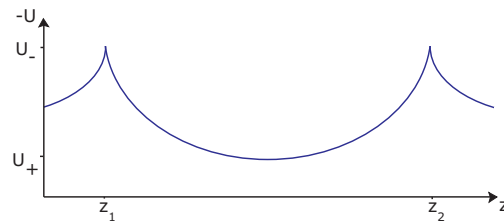
Penning traps are commonly used in atomic physics for particle storage. In 1989 H. G. Dehmelt received the Nobel Prize for his work on developing an ion trap technique. In a typical Penning trap as Dehmelt designed it (see figure 6.7a) a magnetic guiding field in axial direction leads to a cyclotron motion around the axis, thus confining the particle in radial direction. To constrain the motion in axial direction, a quadrupole electric field is applied, reflecting the particles back into the center of the trap. The resulting motion is a sum of three different components; an axial oscillation because of the electric field, the cyclotron motion around the magnetic field lines and the magnetron motion due to the $E \times B$ drift (see also figure 6.7b).

The ignition of a Penning discharge strongly depends on the pressure in the system (see figure 6.8).

The magnetic field lines of a Penning trap do not need to cross the cathode material as they do in the trap in figure 6.7a, but can also go from anode to anode, just passing areas with negative potential inbetween. These traps are called vacuum-vacuum traps (for an example see figure 6.9), the location of the trap is not enclosed by electrodes. Cathode-cathode traps are directly fed from the electrode surfaces by field emission. In contrast to that, the electrons guided on the field lines belonging to the vacuum-vacuum



(a) Schematic view of possible trap



(b) Potential along a field line crossing the trap

Figure 6.6: Guided along magnetic field lines electrons will be stored in the central region of this setup as they are reflected from the negative endings to the positive potential region

traps first have to cross a potential barrier before they reach the trapping region.

Particles can be emitted from Penning traps through collisions or a change in the storage conditions.

Important for the discharge of a Penning trap is the stability of the storage conditions and the depth of the trap. If the potential well is in the order of $\Delta U \approx 100 \text{ V}$, the avalanche mechanism cannot be started as the electrons do not have enough energy for ionisation processes. If the magnetic field is too low, the trapping is also not stable. Electrons escape the guiding magnetic field lines easily. This can be seen in experiments: As soon as the magnetic field is high enough for stable storing, an ignition of the Penning trap takes place (see also figure 6.5).

In the KATRIN MAC-E filters two types of Penning traps can exist: Penning traps within the flux tube and outside of it. If the Penning traps are located inside the flux tube the electrons ejected from them just need enough energy to reach the detector. These traps have to be prevented carefully as they always lead to a rise in the background

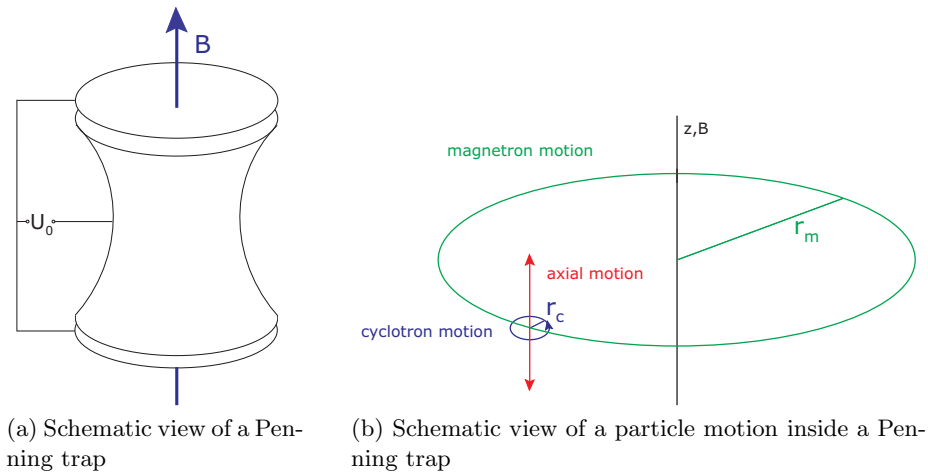


Figure 6.7: A Penning trap for ion spectroscopy

rate. On the other hand, electrons coming from traps outside the flux tube need to have a radial velocity to reach the magnetic flux tube and then also enough energy to reach the detector. This means that Penning traps outside the flux tube are expected not to give rise to as high background as the ones inside. But these traps are still dangerous as the electron plasma inside could penetrate into the flux tube area due to plasma instabilities or space charge effects, thus increasing the background rate. In addition, these Penning traps can cause discharges, leading to instabilities in voltage and pressure.

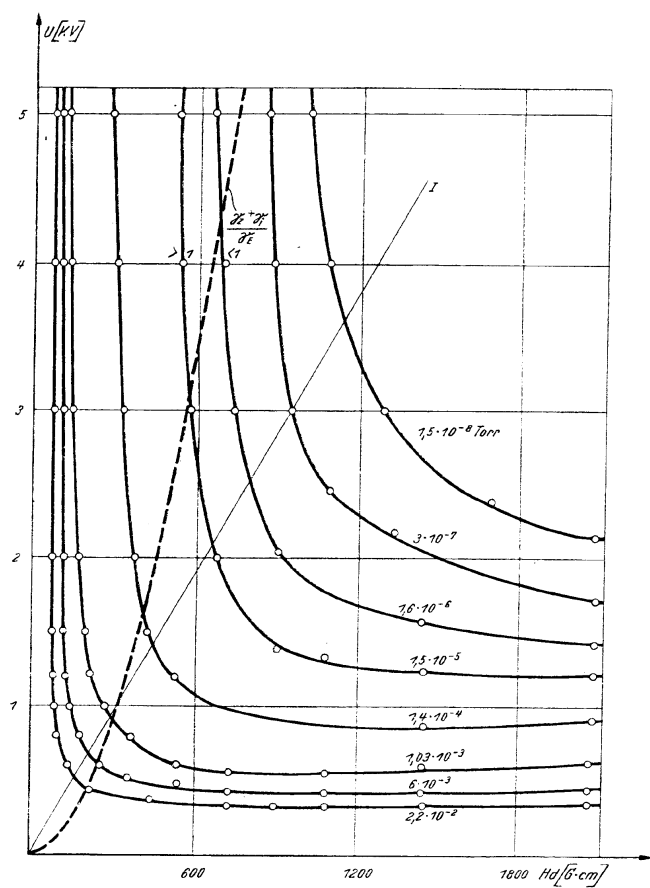
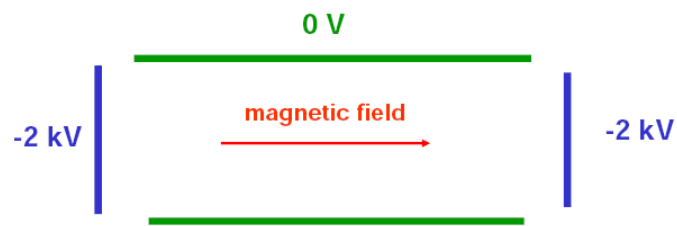


Figure 6.8: Experimental ignition curves for various pressure values between 10^{-2} and 10^{-8} Torr (figure taken from [Hae53])

Cathode-to-cathode Penning trap:



Vacuum-to-vacuum Penning trap:

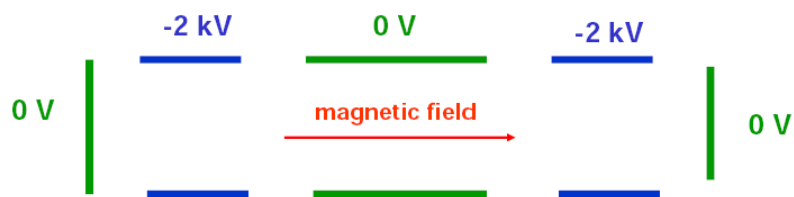


Figure 6.9: Two kinds of Penning traps: a) the magnetic field lines go from cathode to cathode, b) the magnetic field lines go from anode to anode, nevertheless there is a Penning trap between two electrodes on negative potential. Figure taken from reference [Glu07b].

6.2 Discharge experience in predecessor experiments

Before the KATRIN experiment was planned there were two predecessor experiments searching for the neutrino mass by measuring the endpoint of the tritium β -decay with a MAC-E filter. Their experience can be used to avoid mistakes in the KATRIN setup. In this section a brief overview of these experiments, the Troitsk and the Mainz neutrino mass experiments, with regard to Penning traps will be given.

6.2.1 The Troitsk experiment

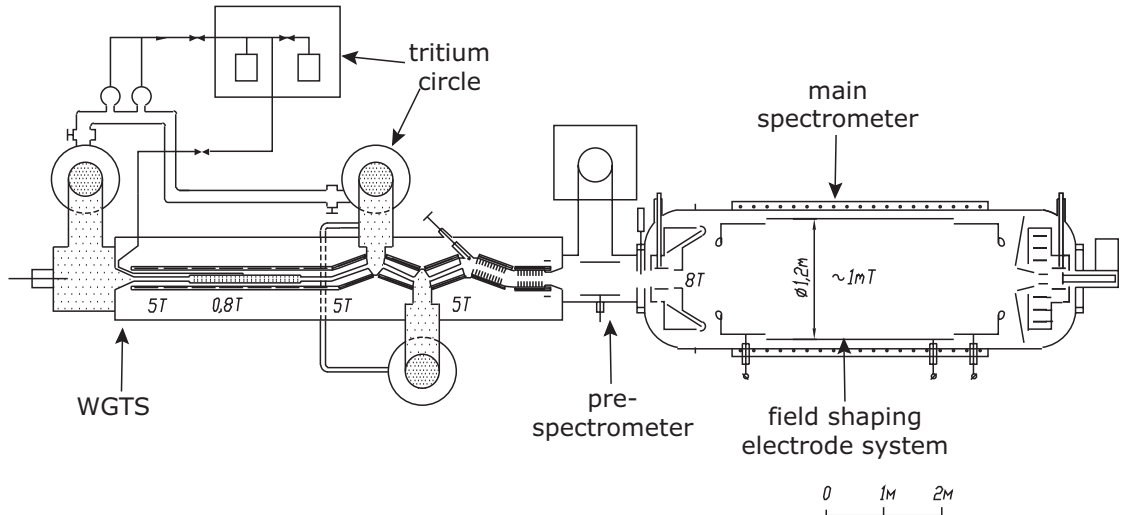


Figure 6.10: Schematic view of the Troitsk experimental setup (picture taken from [KAT04])

The neutrino mass experiment at the INR Troitsk (Russia) has taken data from 1994 to 2002 (around 290 days of data taking). By combining the data of several runs a value of

$$m_{\bar{\nu}_e}^2 c^4 = (-1.0 \pm 3.0_{\text{fit}} \pm 2.1_{\text{sys}}) \text{eV}^2, \quad (6.8)$$

was obtained [Lob01], resulting in an upper limit of

$$m_{\bar{\nu}_e} c^2 < 2.5 \text{eV} \quad (95\% \text{ C.L.}). \quad (6.9)$$

One of the main characteristics of the Troitsk experiment is the gaseous source (WGTS, see figure 6.10) and the idea of a tandem setup with pre- and main spectrometer.

The WGTS has a length of 3 m and a diameter of 50 mm. The strong magnetic field focuses the decay electrons in a beam that is bent several times to allow better differential pumping. The electrons are guided smoothly by the magnetic fields around the edges

while atoms or molecules will hit the tube hull at the bend. This will also be used for the differential pumping section in the KATRIN experiment.

The Troitsk main spectrometer has a length of 7 m with a diameter of 1.5 m and is connected to ground potential. For creating the electric field additional electrodes are built in. In the first experimental setup a complex electrode system (comparable to the one in the Mainz I setup) was used. Starting the experiments, multiple discharges happened, thus making effective measurements impossible with this setup. The complete design of the inner electrode, including the ground electrode, was refined. The electrode geometry has been simplified to a cylinder. Penning traps with depths of ≈ 1 kV still exist inside the spectrometer. Therefore, discharges take place, but they are random and their signal can be distinguished on the detector. To obtain stable measurement conditions, the pressure in the Troitsk main spectrometer had to reach at least a level of $5 \cdot 10^{-10}$ mbar, as the remaining Penning trap would ignite at pressures of $1 \cdot 10^{-9}$ mbar [Kaz07].

The pre-spectrometer was designed to filter out for low-energy electrons, thus reducing the effective electron rate entering the main spectrometer and therefore also some of the background effects (see 2.2.2).

The Troitsk setup never worked as originally planned because of continuous discharges between the two MAC-E filters. A Penning trap is located in this region. The magnet marking the exit of the pre- and the entrance of the main spectrometer provides a strong magnetic guiding field. Both filters have strong negative electric potentials that increase in direction of the exit and entrance respectively, where ground electrodes are located. Thus electrons that crossed the pre-spectrometer filter, but have too low energy to pass the main spectrometer, are reflected back into this region. Having lost longitudinal energy through collisions or cyclotron radiation, some of the electrons cannot cross the potential barrier of the pre-spectrometer, but are confined in the region between the two MAC-E filters. During a measurement the number of electrons confined here rises until they lead to a discharge. The Troitsk experiment could only avoid these discharges by applying ground potential to the pre-spectrometer, thus effectively deleting it from the electromagnetic setup.

With the Troitsk experiment an unexpected line in the β -decay spectra was detected, which could not be confirmed by the Mainz experiment. For the analysis this step in the transmission function was fitted, which leads to unknown uncertainties in the systematic error. In order to investigate the reason for this phenomenon and to avoid possible systematic problems in the KATRIN experiment, the Troitsk collaboration reinvestigates their old experimental configuration by simulations and conducts additional experiments with an improved spectrometer.

6.2.2 The Mainz experiment

From 1994 to 2001 tritium data was taken at the Mainz neutrino mass experiment. Its setup consists of a solid state tritium source with a single MAC-E filter and a detector. The final result [Kra05] states

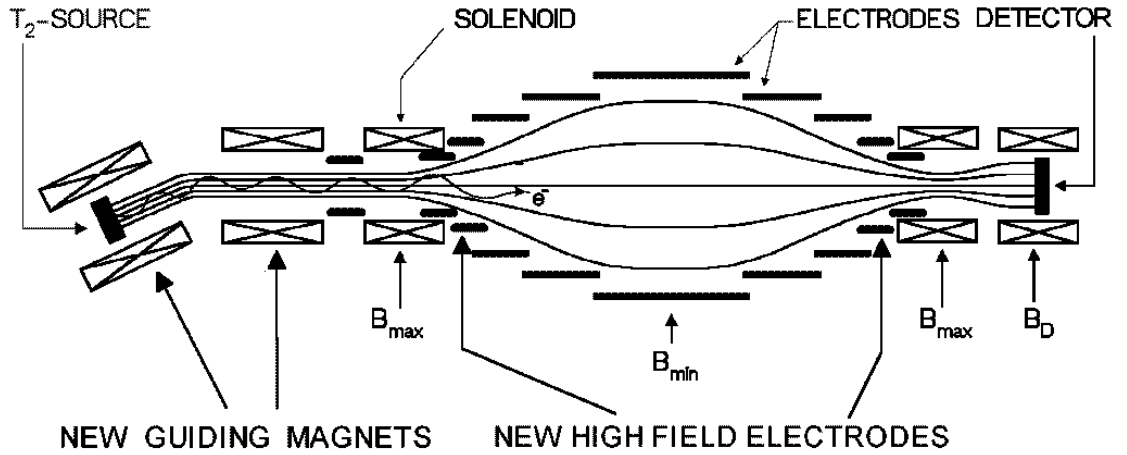


Figure 6.11: Schematic view of the improved Mainz setup with a bend between source and spectrometer to suppress background (picture taken from [KAT04])

$$m_{\bar{\nu}_e}^2 c^4 = (-0.6 \pm 2.2_{\text{stat}} \pm 2.1_{\text{sys}}) \text{ eV}^2, \quad (6.10)$$

yielding an upper limit on the neutrino mass of

$$m_{\bar{\nu}_e} c^2 < 2.3 \text{ eV} \quad (95\% \text{ C.L.}). \quad (6.11)$$

In the course of the years, the setup was upgraded in several steps. Its main feature in comparison to the Troitsk setup is the quenched - condensed tritium source, a solid state molecular tritium film frozen on HOPG. The spectrometer consists of a vessel on ground potential with an electrode system to form the field. The electrode configuration and source section have been improved.

To describe the experiment and its experience with Penning traps, we divide the setup in stages according to the measuring phases. Here, only the electrode configuration is of interest. For further information on the stages of the Mainz neutrino mass experiment, references are given in each section.

The different Mainz setups were reinvestigated with the tool *fieldlinepot.c* with which the electric potential along a magnetic field line can be tracked. Plotting the negative potential against the z coordinate, a potential well will indicate a possible Penning trap. The results will be compared to experience at the experiment in order to improve the understanding of the Penning traps and to roughly estimate some guiding values for ignitions of Penning traps.

Mainz I

In the first test runs of the Mainz I setup with a magnetic field of 6 T and a potential of 20 kV a background rate of $\approx 10^5$ Hz was detected. To reduce this rate, the magnetic

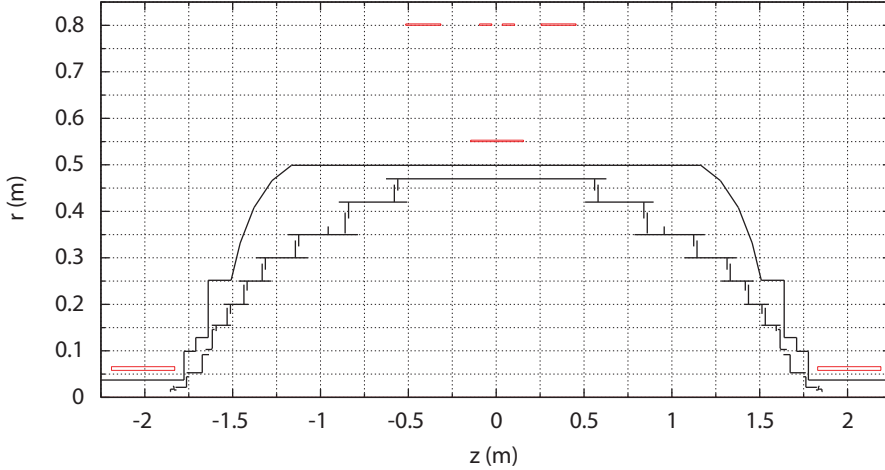
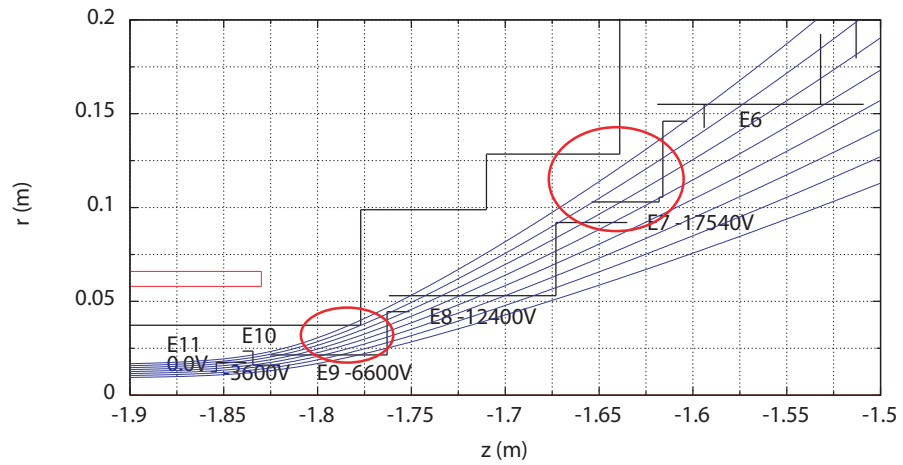


Figure 6.12: Schematic view of the Mainz I setup

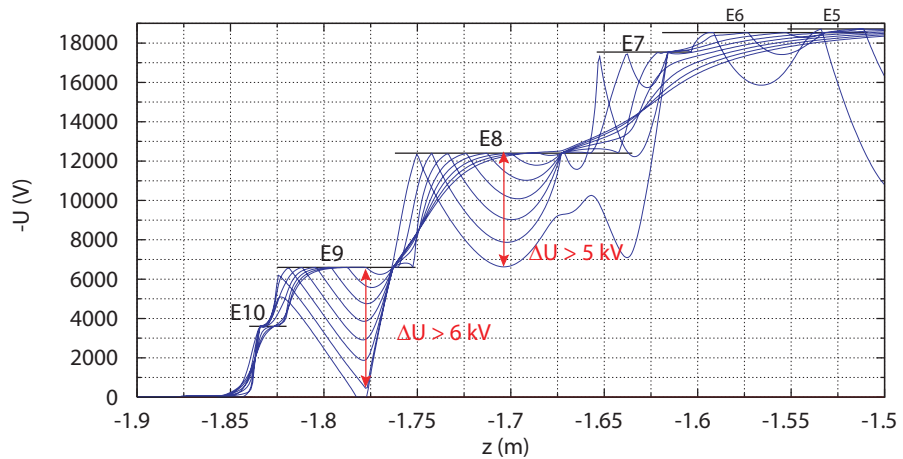
field was decreased to values of 2 T, leading to a rate of 100 mHz. A low background level could also be measured directly after turning on the electric field [Pic90, Pic92]. This behaviour is an evidence for Penning traps located inside the spectrometer. Better rates of about 17 mHz were achieved in the measurement runs of 1994 by avoiding tritium contamination by a cryotrap and decreasing the pressure to levels of 10^{-11} mbar [Bor00]. Opening the spectrometer for replacing some high field electrodes to suppress the trans- U_0 peak¹, residuals of sparking discharges (seen as discolored ringstructures around the electrodes) were found on electrode rings E9, E10 and E11 and on the spectrometer wall close to electrode ring E7 [Bor00]. The position of the electrodes can be seen in figure

¹In the Mainz I measurements two peaks dominated the background: The first peak was seen at the energy of $E = qU_0$ with U_0 being the effective retarding potential and therefore was induced by low-energy electrons emitted from the electrodes or collisions of residual gas molecules in the spectrometer volume. They were then accelerated to the detector where they could be seen around qU_0 . A second peak was detected at slightly higher energies and therefore called trans- U_0 peak. An investigation of the peak in [Gol95] led to the assumption that it is due to secondary electrons emitted from the surfaces: Primary electrons emitted from surfaces collide with another electrode, losing their energy by bremsstrahlung. Their maximum energy is given by the potential difference between the electrodes. The X-rays can then release secondary electrons by photoelectric effect or in an Auger process. If the excess energy E_{ex} after the emission is high and most of the energy resides in the radial motion, these electrons are not guided adiabatically to other surfaces. They can reach the flux tube and are accelerated towards the detector where they would be seen with energies $E = qU_0 + E_{ex}$. For stainless steel the KLL-Auger electrons of chromium lie in the energy range to be emitted by the bremsstrahlung produced between E8 and E9 ($\Delta U = 7.06$ kV) or the characteristic X-ray radiation of nickel and therefore are a candidate for the background. Changing the material of the electrode to e.g. titanium, which has a characteristic X-ray spectrum that cannot cause the Auger electrons from chromium would suppress the Trans- U_0 peak as only electrons with small excess energies would be created and directly guided adiabatically onto other surfaces [Sch01]. In addition the electrode configuration was changed to host more rings thus making the reduction of the potential difference between them possible. The energy of bremsstrahlung will be decreased. No trans- U_0 peak was observed with the Mainz II setup.

6.13a.



(a) Zoom to the relevant electrodes for Penning traps



(b) Potential along the magnetic field lines shown in 6.13a

Figure 6.13: Location and depth of Penning traps in the Mainz I setup

Simulations done within the scope of this thesis show a deep potential well with $\Delta U > 5 \text{ kV}$ between electrode E7 and E8 and an additional one at the electrode ring E9 (see figure 6.13b). In this region the field lines run close to the vessel hull (see figure 6.13a). This is consistent with the experience mentioned above, thus supporting our use of the program *fieldlinepot.c* for locating particle traps.

Further information on the Mainz I measuring phases can be found in references [Pic90, Wei93, Gol95].

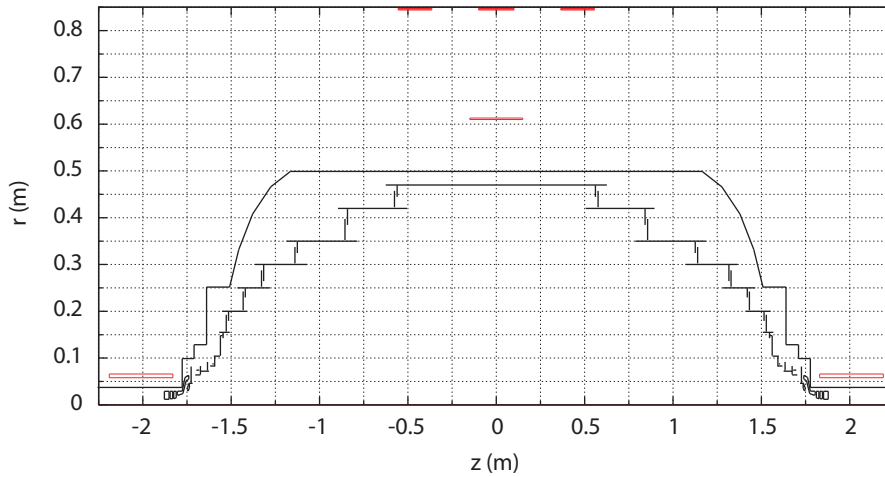


Figure 6.14: Schematic view of the Mainz 2 setup - electrode rings E7 - E11 (located at $|z| > 1.6$ m) from the Mainz I setup were replaced with a new designed ringstructure

Mainz II

Between 1995 and 1997 the Mainz I setup was first opened for electropolishing to remove tritium contamination and improve the high voltage stability. In addition, the high field region was redesigned to avoid the Trans- U_0 peak [Bor00]. A schematic view of the Mainz II electrode structure is given in figure 6.14, details are visible in figure 6.15a.

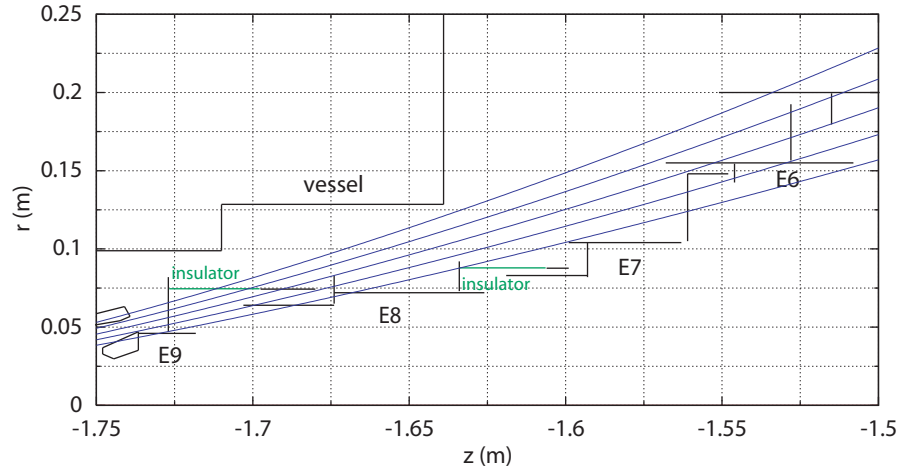
In the measurement phases in 1997 and 1998 discharges still occurred. They could be seen in particular in a breakdown of the voltage applied on the electrodes E8 and a high background level. To avoid this, a high frequency pulsing potential with a frequency of 1.1 MHz and an amplitude of 65 V was applied on electrode E8 for 3 s between 20 s of data taking. The background rate could be reduced by this method, but only if the environmental conditions were not ideal. If the background level in the setup was already low (≈ 15 mHz), no further improvement could be obtained [Ulr00, Sch01].

The interpretation of these simulations is not unambiguous, as the charging properties of the insulators between electrode rings E7, E8 and E9² are not known and could therefore not be implemented into the program. It is possible that the insulators do not influence their surrounding potential at all. Other possibilities would be that the surface of the insulators becomes charged with some undefined potential or zero potential.

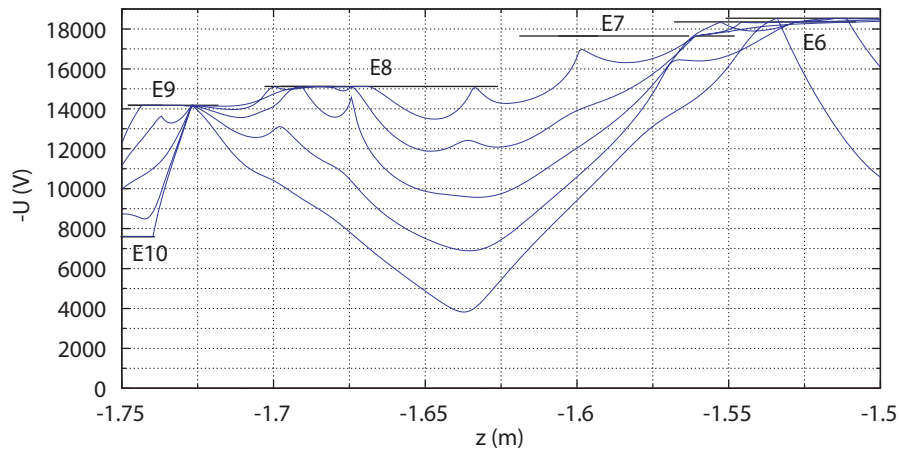
For these simulations the insulators were assumed to have no influence on their surrounding electric field and were therefore not implemented at all. A potential well with depth $\Delta U \approx 10$ kV is then present in the setup (see figure 6.15b). The depth of the Penning trap has to be considered with caution, because it is unphysical to assume that the ground potential is not shielded at all by the insulator.

An additional simulation was done under the assumption that the insulator surface

²In the setup the insulators are separated into small segments along the whole circumference. For these considerations they were treated as whole rings.



(a) The relevant electrodes for Penning traps



(b) Potential along magnetic field lines

Figure 6.15: Location and depth of Penning traps in the Mainz II setup without the insulator between E8 and E9

charges up according to the neighbouring electrodes. Therefore, the insulator surface was divided into small parts and a differential potential was assigned, starting from -15.119 kV (E8), ending with -14.180 kV (E9).

Comparing the results of the simulations without and with insulator, the difference seems to be negligible. The depth of the Penning trap remains $\Delta U \approx 6$ kV.

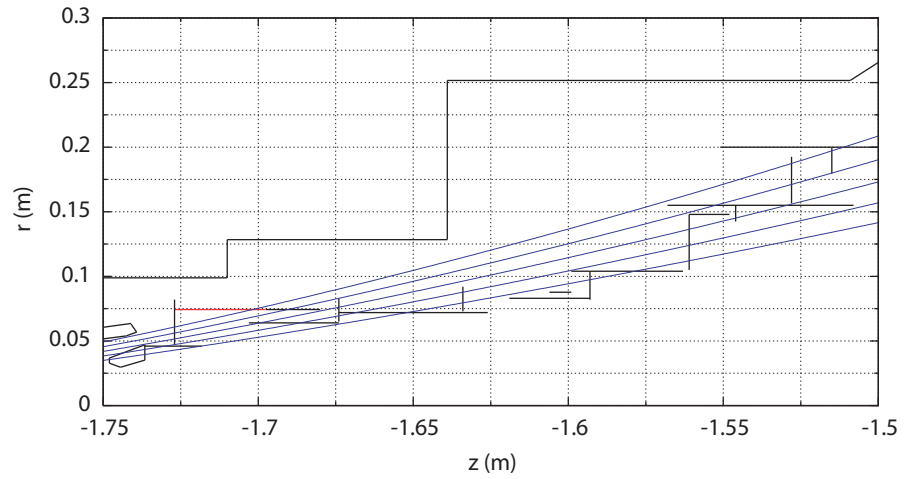
The high-frequency pulsing on electrode ring E8 seems to disrupt the particles' trajectories, thus emptying the trap. Thorough simulations to investigate the influence of the high frequency pulsing on the trapping were not done.

Further information on the Mainz II setup and results can be found in references [Bor00, Bor02, Ulr00, Sch01]

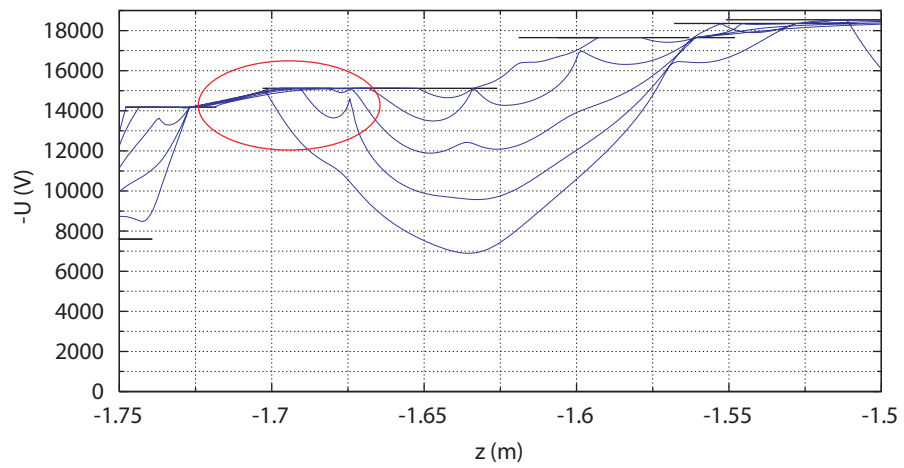
The Penning traps found for the Mainz I and II setups seem to be rather severe, but

are all suppressed as they are located outside the electrode system. The measurements worked as the surrounding conditions were strictly controlled: the general pressure level was reduced to a level of 10^{-11} mbar. All electrodes were electropolished before assembly and each measurement was preceded by conditioning. In addition the full magnetic field was not used.

The Mainz II setup was the last configuration taking data for neutrino mass limit measurements. Since then the setup has had several upgrades for test measurements with respect to the KATRIN setup. The configurations built after Mainz II were used to test ideas for background reduction. In the Mainz III configuration a wire electrode was installed for a first study of the screening effect described in chapter 2.2.4 [Fla04]. In addition, the extraction of stored particles by applying a dipole potential was tested [Mue02].



(a) Zoom to the relevant electrodes for Penning traps



(b) Potential along magnetic field lines

Figure 6.16: Location and depth of Penning traps in the Mainz II setup with the insulator between E8 and E9 on a differential potential

Mainz III

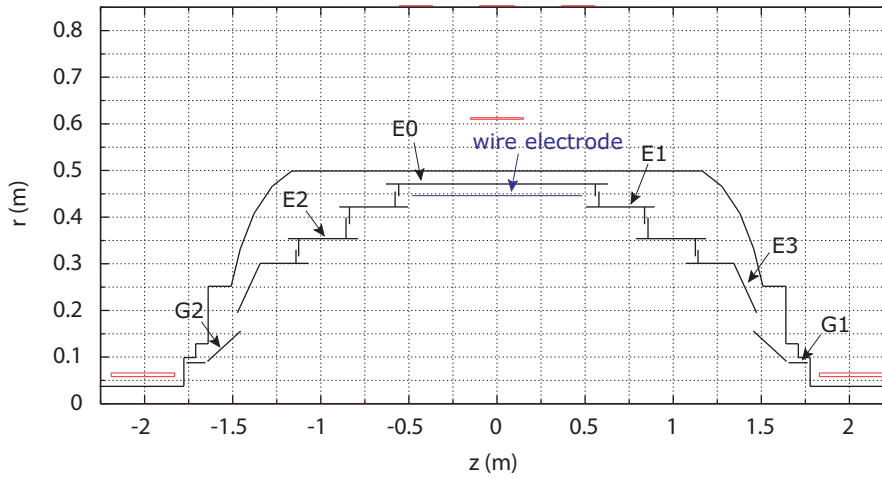


Figure 6.17: Schematic view of the Mainz III setup - the high field region of the spectrometer was replaced with a simplified structure and a wire electrode shields the central region of the spectrometer

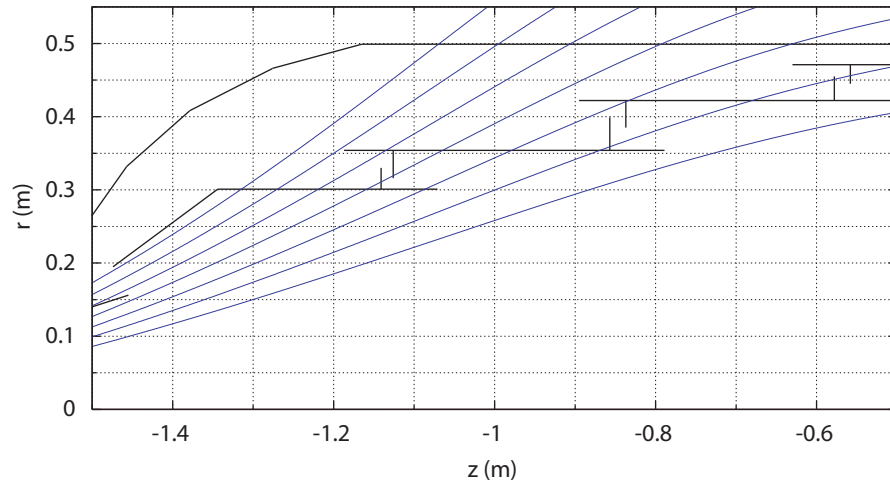
For this setup the whole structure starting from electrode E4 to E13 was removed. Two additional ground electrodes were added to the system. The central electrode E0 was screened with a wire electrode. The geometry of electrode ring E3 and ground electrode ring G2 were adjusted to shield possible sparking from E3 by G2 (see figure 6.17).

The background for the standard configuration (electrodes E0 - E3 on -18.5 kV, the wire electrode on -18.6 kV and the electrodes G1 and G2 grounded) was reduced to a level of 5 mHz, less than one third of the level reached with the Mainz I and Mainz II setups [Mue02].

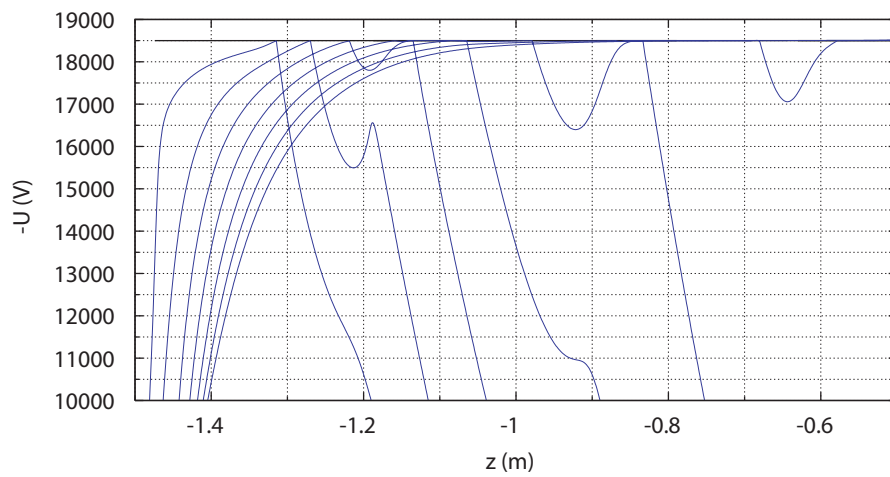
Several small traps with a depth of $\Delta U > 2$ kV were found inside the spectrometer (see figure 6.18). As the low background level suggests that any remaining traps are not stable, we can derive guiding numbers for approximate ignition conditions.

Applying high potential differences on the electrodes G1 and G2 the background increases rapidly. Therefore the potential on these electrodes should be limited to $|U_{G1}| < 4$ kV and $|U_{G2}| < 12$ kV [Mue02]. Simulations employing these limit values already show the development of small Penning traps with a depth of $\Delta U \approx 1$ kV (see figure 6.19). Rising the potentials of the electrodes G1 and G2 will deepen the traps, thus making the ignition of a Penning discharge possible and giving rise to an increase in background.

The simulations of the Mainz experiments help understanding the relevant mechanisms that are important for discharges. They set limits on the magnetic field strength necessary for particle storing as well as the maximum depth Penning traps may have without causing severe problems.

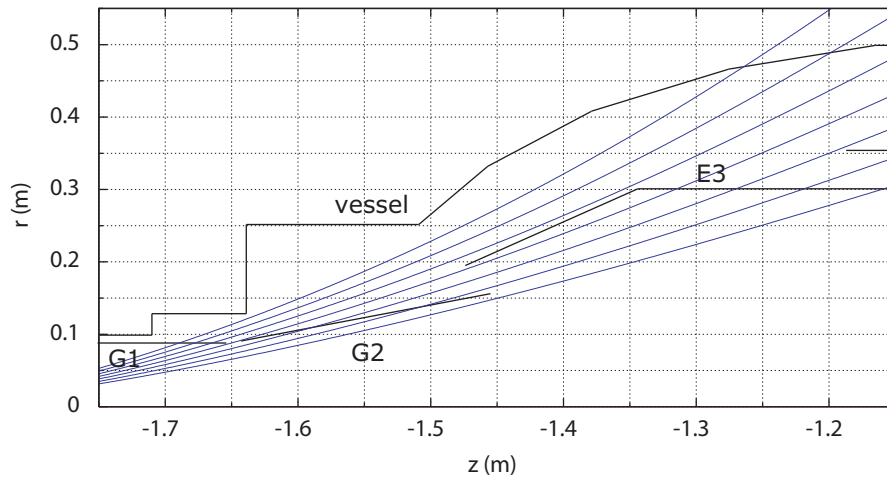


(a) Zoom into region with potential wells

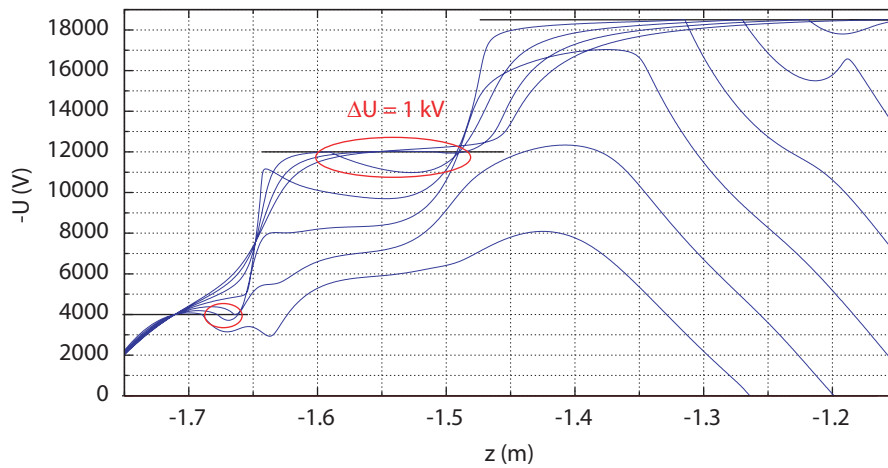


(b) Potential along field lines

Figure 6.18: Potential wells in the low magnetic field region, Mainz III, standard configuration



(a) Zoom into ground electrode region



(b) Potential along field lines

Figure 6.19: Penning traps for a setup with G1 on -4 kV and G2 on -12 kV for Mainz III

6.3 Unstable conditions related to particle trapping in the pre-spectrometer of the KATRIN experiment

6.3.1 Experiments

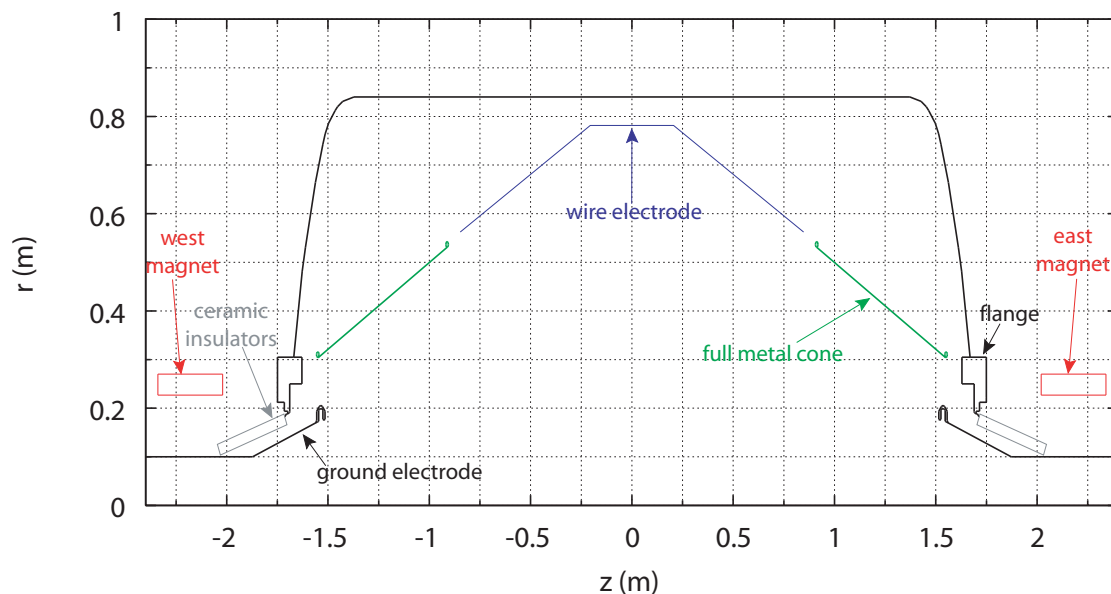


Figure 6.20: Schematic view of the pre-spectrometer setup as of 2006/early 2007 in the r - z plane

Electromagnetic test measurements at the pre-spectrometer setup in 2006 (see figure 6.20) were impeded because the voltage could not be risen to the design value without causing discharges. These manifested as a high background level measured at the detectors³, breakdown of the applied electric potential, high leakage currents and even a rise in the pressure reading. After fixing some devices with undefined potential, the strength of the discharges was reduced⁴, but the effect could not be entirely avoided. As these measurements were all done without magnetic field, this led to the assumption that the background is caused by vacuum discharges. Some surfaces inside the pre-spectrometer have micro tips. The application of high potentials to these surfaces will lead to high field strength at the tips thus making the emission of electrons possible. If the number of electrons emitted from the cathode is high enough, they can cause an avalanche rise of the number of charged particles, thus causing discharges⁵. This can be seen in a

³An MCP detector was built in at the detector side of the pre-spectrometer. For testing purposes a silicon PIN diode was connected to the source side of the spectrometer. These detectors were not always used, as they are endangered by the high background rates. Therefore the valves connecting them to the spectrometer volume could be closed.

⁴M. Leber, [ELOG], entry 98, 23.11.2006, Comparison of breakdowns before and after fixing ground cable

⁵The number of positive ions from the anode is smaller, since the tunnel efficiency is also determined

breakdown of potential, high leakage currents and a rise in pressure reading. To prevent this, thorough conditioning of the surfaces has to be done. This includes baking the vacuum vessel to get rid of residual gas intruded into steel as well as the application of high potentials of both polarities on the electrodes for a longer time at higher pressure. The electrons emitted from the cathode will ionise atoms which are accelerated towards the negative electrode. They sputter off the micro tips, thus deburring the surface. A baking of the pre-spectrometer will also improve the vacuum.

Investigations showed that the vessel surface close to the conical electrode was responsible for the increased background measured at the detectors. This could be determined because the strength of the discharges rose with the applied voltage on the vessel. It was also sensitive to the potential difference between the cone electrode and the vessel. Positive potential differences ($U_{cone} > U_{vessel}$) lead to higher background rates while a negative voltage difference ($U_{cone} < U_{vessel}$) can screen the background^{6,7}. The emitted electrons can be screened with a slightly more negative wire electrode ($\Delta U = -200$ V). Also a high positive potential difference (+1.5 kV) between wire electrode and vessel will reduce the background rate^{7,8}. Detailed discussions with engineers pointed to the connection between the flange and the ceramic insulator that was soldered [Wol07]. As the materials do not connect easily the resulting joints are porous and therefore not ideal for high potentials and vacuum (see figure 6.21).



Figure 6.21: Soldering joint at the ceramic insulator

In addition the ground electrode was made of titanium⁹, which is difficult to process. Therefore some bad welding seams are located at the ground electrode (see figure 6.22). For irregular surfaces the emission of ions by electron collisions is more probable. There-

by the mass of the particle $T \propto e^{\frac{m}{h} \int_{x_0}^{x_1} (U(x) - E) dx}$. Therefore, they can be neglected for first considerations.

⁶M. Leber, [ELOG], entry 110, 01.12.2006, First separation of tank and wires from cones

⁷M. Leber, [ELOG], entry 111, 01.12.2006, Second Measurement Tank vs Cones

⁸M. Leber, [ELOG], entry 115, 05.12.2006, effect of inner wires on detector rates

⁹The ground electrode was made of titanium to avoid the trans- U_0 -peak, which can arise from X-rays inside the spectrometer, see also section 6.2.2.

fore, these seams can possibly lead to an increased background and the surface of the ground electrode should either be shielded with a glass insulator or the ground electrode should be replaced.



Figure 6.22: Welding seam at the pre-spectrometer ground electrode

Further problems arose at the pre-spectrometer when the magnetic field was turned on in addition to the electric potential¹⁰. While ramping up the magnets the total signal rate increased, leading to a rise of pressure and a breakdown of the potential.

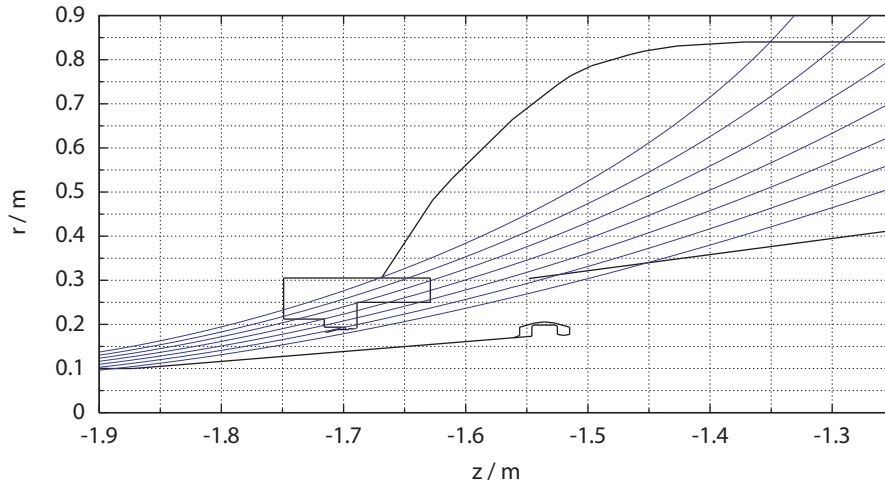
These ignitions with magnetic and electric fields at the same time indicate that a Penning trap might be present inside the spectrometer.

Searching with the tool *fieldlinepot.c* (see section 3.1.3) for magnetic field lines with potential wells in the pre-spectrometer, a Penning trap with depth > 5 kV was revealed at the entrance region of the pre-spectrometer (see figure 6.23b) [Glu06d]. Electrons guided along field lines from the flange to the full metal cone or vessel hull see the more positive potential (0 V) of the ground electrode (see figure 6.23a). Losing energy through collisions, they are confined to the region with more positive potential. As the soldering at the flange is not good, this surface can feed additional electrons into the trap via field emission.

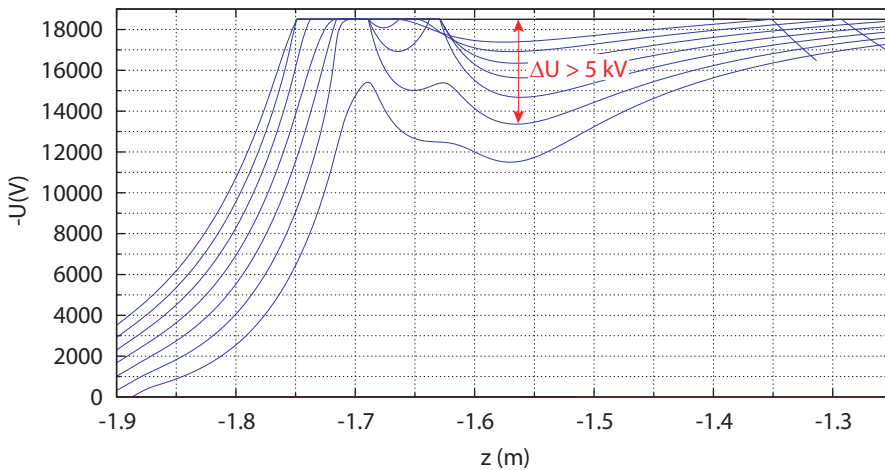
Additional experiments in 2006 and 2007¹¹ supported the theory of a Penning trap

¹⁰M. Leber, [ELOG], entry 103, 28.11.2006, HV breakdown when magnets turned on

¹¹Detailed information is archived in reference [ELOG]: Entries concerning the Penning trap studies



(a) Fieldlines going from the flange to the cone electrode or the vessel (cathode to cathode) crossing the area influenced by the ground electrode potential (anode)



(b) Potential along the field lines shown in figure 6.23a

Figure 6.23: Magnetic field lines showing a Penning trap in the KATRIN pre-spectrometer. The sharp bends denote where the field lines leave the pre-spectrometer and are therefore not interesting.

existing in the pre-spectrometer as seen in the simulations.

From chapter 6.1.3 we know that values for an ignition of a Penning discharge should be reproducible if the conditions are the same. The ignition curve U over B can show different ignition thresholds depending on the order in which the fields are being applied (see figure 6.5). In addition, the Penning discharge is strongly dependent on the pressure in the setup (see figure 6.8). Therefore, measurements of the U over B dependencies and their connection to the system pressure can give evidence of a trap.

The fact that reduced background levels were measured for configurations which showed no Penning traps in simulations supports this theory.

Based on a few selected measurements, partly performed within this thesis, evidence for a Penning trap inside the pre-spectrometer will be given and the correspondence between simulations and measurement will be investigated. The magnetic field in these measurements is given by the current running through the supraconductive coils with 157 A corresponding to the nominal field of 4.5 T. Different measurement conditions were created by using only one coil (east or west) or using both coils to create the magnetic field. For the presented measurements the same potential was applied to the vessel, conical and wire electrodes.

Dependence of ignition on system pressure

During the measurements the pressure reading in the pre-spectrometer varied over nearly four orders of magnitude between $7.7 \cdot 10^{-10}$ mbar after two days of continuous pumping and a few times 10^{-6} mbar while a breakdown takes place. To keep the setup conditions in a comparable range, the starting pressure was reduced to values of the order of 10^{-9} mbar.

Table 6.1: Different measurements hinting for a dependence of ignitions on system pressure. A discharge was noted, if the pressure rose to 10^{-6} mbar and the leakage current went into current limitation. The last column notes special circumstances under which these measurements were done.

magnet used	voltage [kV]	pressure [mbar]	magnet current [A]	date	details
east	-10	$5.0 \cdot 10^{-09}$	3.5	07/01/18	ignition after 1 min with small discharges 6 prec. discharges
east	-10	$1.5 \cdot 10^{-09}$	6.1	07/01/19	spontaneous discharge first discharge of day
east	-15	$1.6 \cdot 10^{-09}$	4.5	07/01/19	third discharge of day
east	-15	$8.1 \cdot 10^{-10}$	7	07/01/22	first discharge of day after 2 days pumping

In the course of the test experiments indications of a strong influence of the pressure on the ignition (see table 6.1) as well as evidence for no dependency at all could be found (see table 6.2). In order to interpret these measurements correctly, the environmental conditions have to be evaluated.

Taking into consideration the 'history' of the setup, the predecessor discharges seem to have an influence on the ignition voltage and currents. This can be caused by a roughening of the surfaces due to the short term currents between them. New micro tips may have developed leading to a decrease in the field emission barrier.

The pressure dependence could not be shown unambiguously.

Table 6.2: Different measurements hinting for a dependence of ignitions on system pressure. The last column notes special circumstances under which these measurements were done. Fixed field denotes here, which field was kept constant while the other was ramped to obtain data for the ignition of a discharge.

magnet used	voltage [kV]	pressure [mbar]	magnet current [A]	date	
west	-30	$1.5 \cdot 10^{-09}$	4.6	07/01/18	first discharge of day
west	-30	$8.5 \cdot 10^{-10}$	4.7	07/01/15	first discharge of day
west	-10	$7.0 \cdot 10^{-09}$	15	07/01/17	fixed electric field
west	-10	$1.8 \cdot 10^{-09}$	15	07/01/17	fixed magnetic field
				measured in direct succession	

Measurements of ignition curves for different magnetic fields

As seen in figure 6.5, a dependency of the potential on the magnetic field is expected for the breakdown. This was tested at the pre-spectrometer for different magnetic field configurations and is shown in figure 6.24. As these curves show only a few measurements under not exactly the same conditions, the interpretation has to be approached with caution. In addition, the measurement covered only a small potential and magnetic field range. Therefore, no prediction of the behaviour at different field strengths can be done. The main conclusion derived from these measurements is that there is a hard separation between stable conditions and breakdown. The order of the field application influences the breakdown ignition (see figure 6.24, 1,2 in contrast to 2',1').

Measurement of simulated 'Penning trap' and 'No-Penning trap' setups

With the help of simulations electric and magnetic field configurations can be chosen for which no Penning trap should be present in the pre-spectrometer. Several of them have been tested. As an example, a measurement of a setup with a Penning trap and - after a slight change - without Penning trap will be presented here.

By applying a positive (instead of the usually negative) potential on the vessel, the cone and the wire electrodes while using both magnets for a symmetric magnetic field, one creates a Penning trap in the center of the pre-spectrometer. Field lines starting in the area of the ground electrodes at zero potential pass the middle of the spectrometer, where the potential is more positive (see figure 6.25a and 6.25b). A Penning trap is present here and electrons will be stored in it. With a potential of +10 kV applied on the electrodes a trap depth of 10 kV is expected from the simulations. This seems to be a deep trap leading to the assumption that the discharge will be quite strong.

Using only one magnet to provide the magnetic guiding field only small Penning traps remain in the setup (see figures 6.26a and 6.26b).

A measurement confirming the assumptions based on the simulations was conducted on

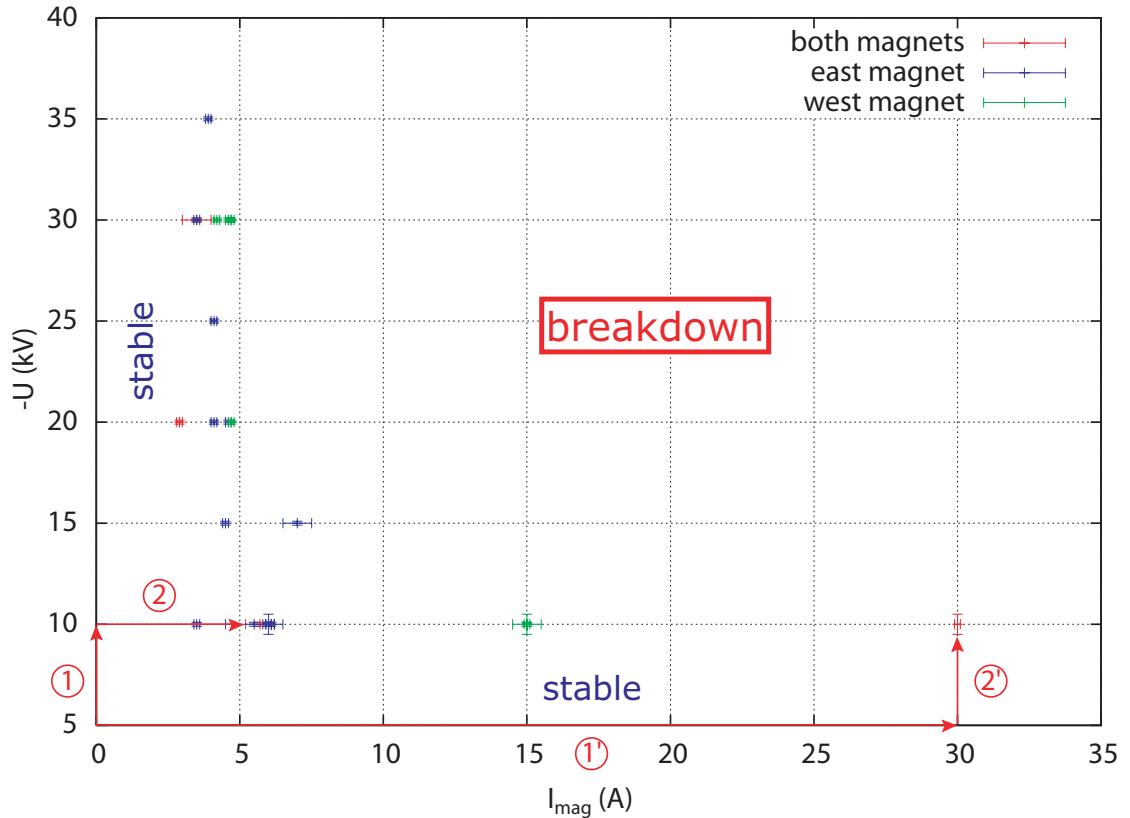
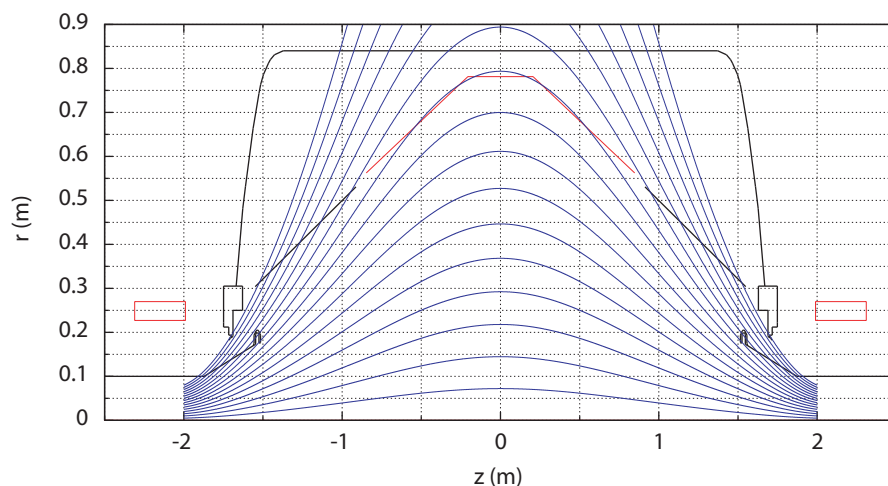


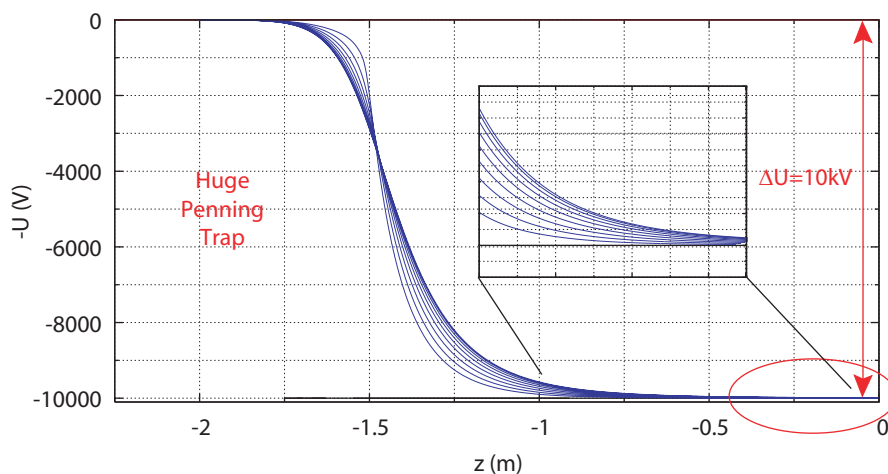
Figure 6.24: Dependency of the ignition voltage on the magnet current for different pre-spectrometer magnetic field configurations (schematic curve see figure 6.5). The breakdown was defined by voltage instability, leakage currents rising to the current limit of the voltage supply and rise of the pressure reading to 10^{-6} mbar. The red arrows mark an example for the dependence of the ignition on the application order: For a potential of 10 kV the ignition takes place at a magnetic current of 5.7 A in both magnets (1, 2). If the magnet current is ramped up first to 30 A the setup gets highly unstable when the potential reaches 10 kV (2', 1').

07/01/24¹². Vessel, cone and wire electrode were connected to one power supply and elevated to +10 kV. Ramping up both magnets, a continuous discharge was reached with a current of 24.5 A in the coils. Reducing the current in magnet one (east) leads to a decrease in pressure reading and leakage current, but a stable setup was only reached a few minutes after the current was completely turned off. This measurement supports the Penning trap simulations described above.

¹²see [ELOG], entry 146, F. Fränkle, F. Glück, K. Hugenberg, K. Valerius: further tests with positive potential



(a) Magnetic field lines in the pre-spectrometer



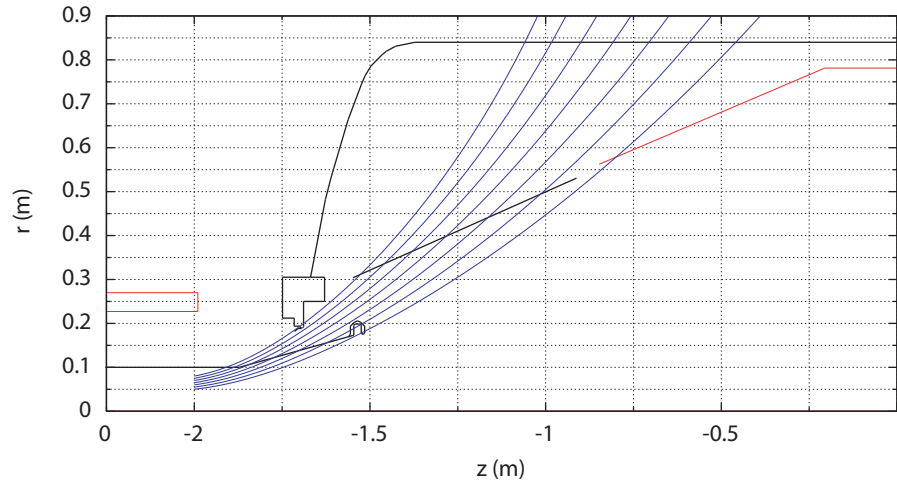
(b) Potential along the magnetic field lines

Figure 6.25: Magnetic field lines inside the pre-spectrometer for a symmetric magnetic field configuration (both magnets) and positive potential on vessel, cone and wire electrode

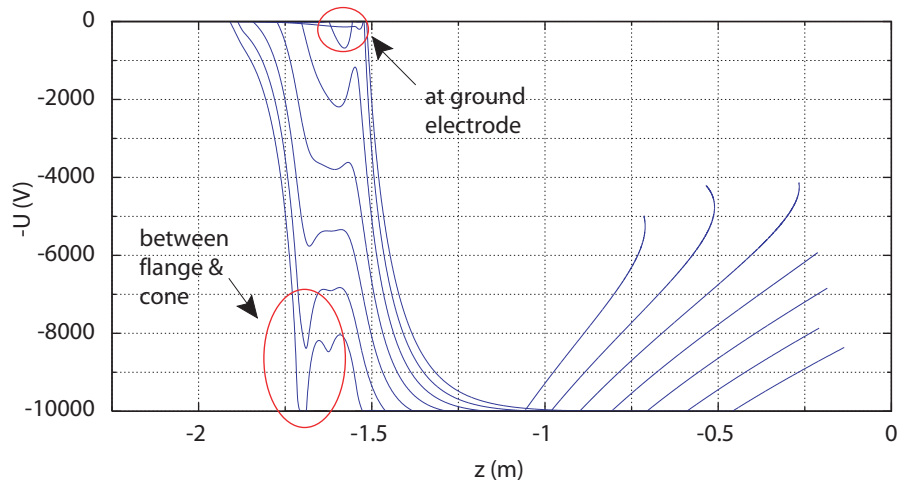
Conclusion

The combination of all experimental results is a clear indicator for a Penning trap in the pre-spectrometer. Simulations can successfully explain the behaviour of the setup and allow to design additional electrodes for Penning trap suppression.

An overview of the experiments done up to march 2007 with the pre-spectrometer to investigate its Penning trap is given in reference [Glu07c].



(a) Magnetic field lines in the pre-spectrometer for an asymmetric magnetic field



(b) Potential along the magnetic field lines

Figure 6.26: Magnetic field lines inside the pre-spectrometer for an asymmetric magnetic field configuration (only one magnet) and positive potential on vessel, cone and wire electrode

6.3.2 Simulations for an additional electrode to avoid a Penning trap inside the pre-spectrometer

These simulations were conducted together with K. Valerius and F. Glück. A detailed overview can be found in reference [Glu07a]. In this section only an overview of the important simulation steps is given.

To avoid Penning traps in the pre-spectrometer, the region in which the Penning trap would be located has to be shielded from the penetrating potential of the ground electrode. An additional electrode should therefore be installed inside the pre-spectrometer.

In view of the difficulties of changing an already existing electrode setup, several technical requirements have to be considered in the design process:

- The device must be mountable through the $\varnothing 500$ mm flange. Therefore, a radius of $r \leq 250$ mm should not be exceeded.
- The wire and cone electrodes are already installed inside the pre-spectrometer. To avoid damaging them, the shielding electrode should have a safety margin towards the full cone.

For the electromagnetic configuration the following details have to be taken care of:

1. Electrode surfaces should not be placed in direct vicinity to the flux tube, as they emit low energy secondary electrons. A safety margin of 20 mm should therefore be kept to avoid direct transportation from the electrodes to the detector. Furthermore, without safety margin, a misplacement would directly affect the transmission.
2. The field strength in different parts of the setup should be considered. It is more vital for cathode surfaces, as the electrons have a higher probability to pass the potential barrier than the positive ions (see also section 6.1.2). The field strength at the anode may therefore be slightly higher.
3. In the KATRIN setup the pre-spectrometer is used to pre-filter the electrons. Therefore, its transmission properties are not too important, as the interesting decay electrons pass the filter with excess energies of ≈ 100 eV. Too early retardation is therefore allowed for the pre-spectrometer in the neutrino mass measurement, if it still lets the relevant electrons pass. For test measurements with the stand alone pre-spectrometer the transmission should be relatively good with no early retardation.
4. No Penning trap should be left inside the pre-spectrometer, as even small traps can possibly give rise to background.

The flange provides a possibility to mount the shielding electrode. The geometry there should be taken into consideration as well as a possible beneficial shielding effect if the electrode is extended to the bad soldering joint at the flange (see figure 6.27).

Being directly mounted to the flange, the shielding electrode will also be placed on vessel potential. To shield the influence of the ground electrode, it needs to geometrically extend further into the pre-spectrometer vessel.

In the configuration found for the pre-spectrometer, the additional electrode extends from $z_s = -1.709$ m, $r_s = 0.179$ m to $z_e = -1.427$ m, $r_e = 0.2415$ m. The ends are equipped with additional rings, thus avoiding high field strengths due to sharp edges (see figure 6.28 and the technical drawing A.2). The ring at the mounting point has a diameter of $d = 10$ mm, the end ring has been chosen to $d = 8$ mm as the field strengths there are not as severe. The new ground electrode will end at $z_e = -1.620$ m and $r_e = 0.155$ m. The end is shielded by a ring with diameter $d = 10$ mm. The starting

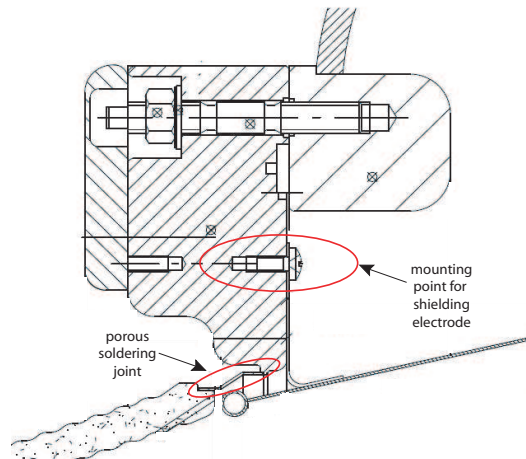


Figure 6.27: Technical drawing of mounting point for the additional electrode (detail of figure A.2 provided by H. Hucker, FZK)

point of the ground electrode remains unchanged. The simulated maximum field strength of ≈ 1000 kV/m at the cathode and ≈ 1100 kV/m at the anode is only slightly higher than the ones for the reference setup, in which field emission was assumed to take place at the bad soldering joint. As the additional electrode shields the bad soldering joint at the ceramic, this field strength does not seem critical. The titanium ground electrode has to be replaced with a shorter version, because the shielding electrode is not long enough to completely screen potential penetration from the ground electrode¹³. This has the advantage of dispelling at the same time the problematic welded seam. The new ground electrode was made of stainless steel.

If equal potentials are applied to all electrodes ($U_{vessel} = U_{cone} = U_{wire} = -18.5$ kV) a Penning trap with depth 180 V remains (see figure 6.29a). An additional trap can be seen at the mounting point of the shielding electrode (see figures 6.28 and 6.29a for details). This trap is assumed to be uncritical, as it is shielded. The probability for electrons to reach the flux tube is little. In addition, the trap volume is very small. Therefore, it is not sure whether stable storing can take place there. Due to the additional electrode the electrons are retarded too early (see figure 6.29b).

As even a shallow Penning trap might give rise to an increase in background, a particle trap should be completely avoided for neutrino mass measurements. This is possible if a more negative potential is applied to the cone. This will lead to a total removal of the Penning trap (see figure 6.30a, but also give rise to too early retardation of the electrons. For test measurements the transmission should be enhanced. This can be done by applying a more positive potential on the cone, thus avoiding too early retardation at

¹³A longer shielding electrode was not advisable without using larger radii, as otherwise problems with the transmission of the complete flux tube occur. In addition the distance to the wire electrode would become too small.

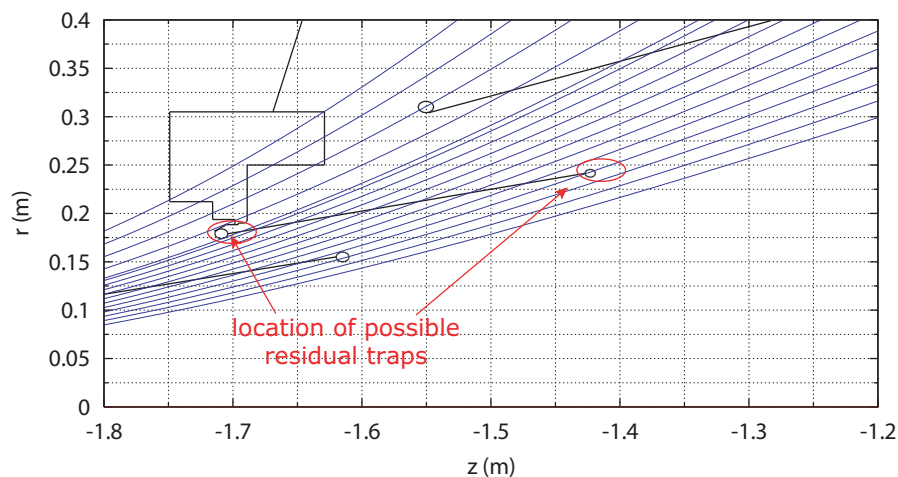
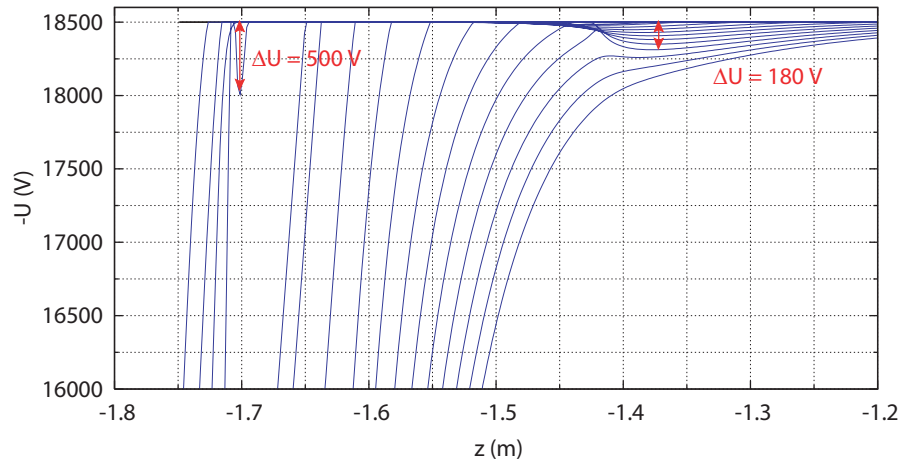


Figure 6.28: The new pre-spectrometer setup with shielding electrode and replaced ground electrode. The location of possible Penning traps is marked

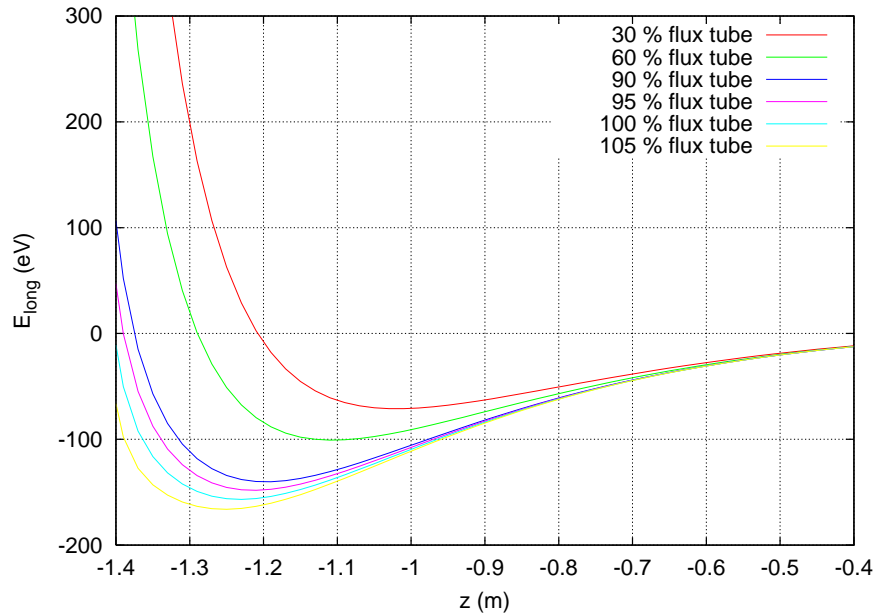
the cost of a larger Penning trap inside the spectrometer (see figure 6.31).

An overview of the different pre-spectrometer modi, design requirements for the shielding electrode, simulations and the resulting configuration that was built into the pre-spectrometer in September 2007 can be found in [Glu07a] and [Val08].

First measurements concerning the remaining Penning trap and the background level resulting from different trap depths are presently being carried out. Their results are important for the design of the main spectrometer electrode system. Updates on these measurements can be found in [ELOG] and will be reviewed in reference [Val08].

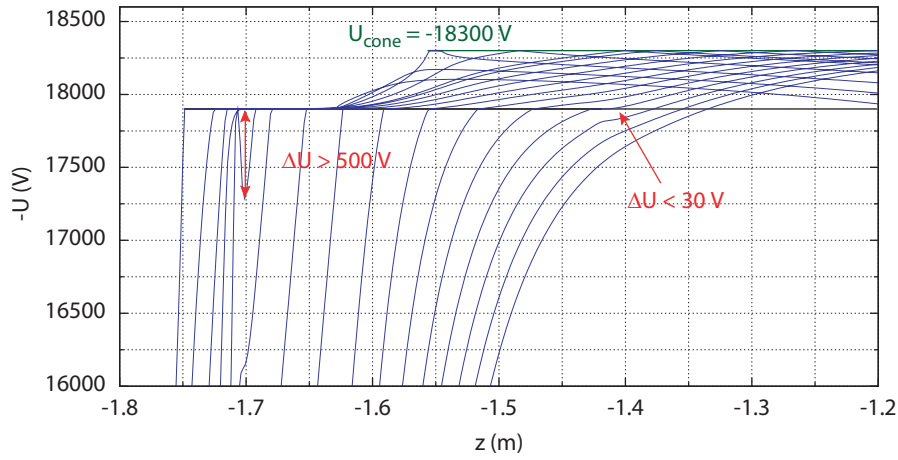


(a) Potential along magnetic field lines

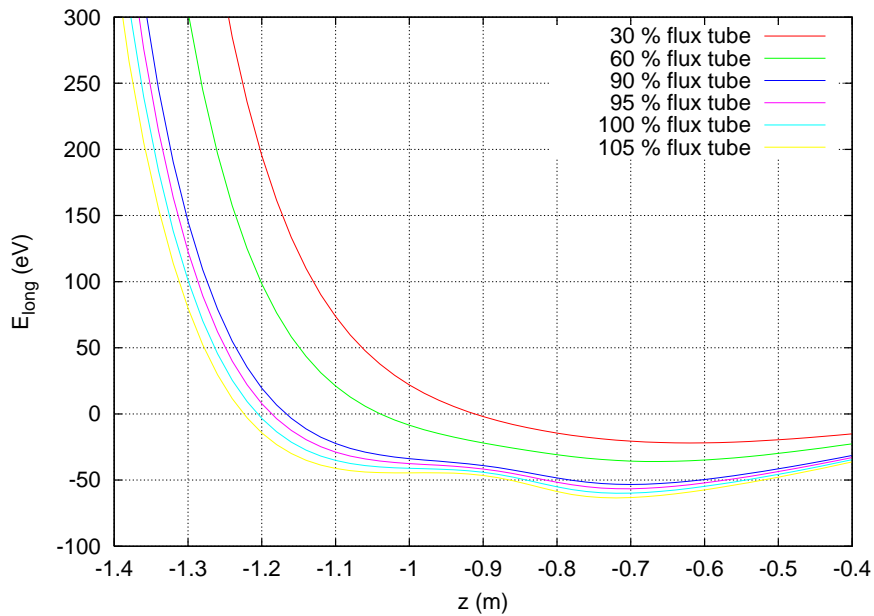


(b) Transmission in adiabatic approximation, please note that only the cut-out from -1.4 m to -0.4 m is shown here

Figure 6.29: Characteristics of the pre-spectrometer in the normal measurement mode $U_{vessel} = U_{cone} = U_{wire} = -18.5 \text{ kV}$. The negative values of the transmission are not important, as the pre-spectrometer is just used as a rough filtering tool. The interesting electrons will pass the spectrometer with excess energies of $\approx 200 \text{ V}$ and are therefore not concerned by the too early retardation.

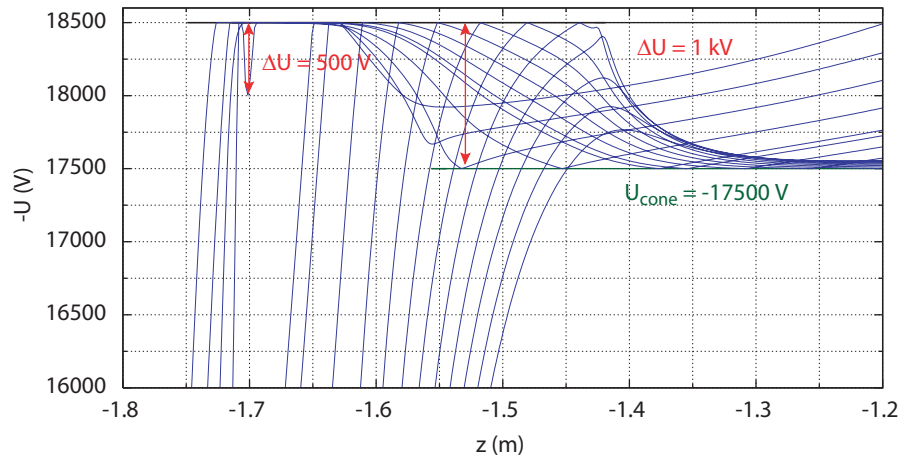


(a) Potential along magnetic field lines

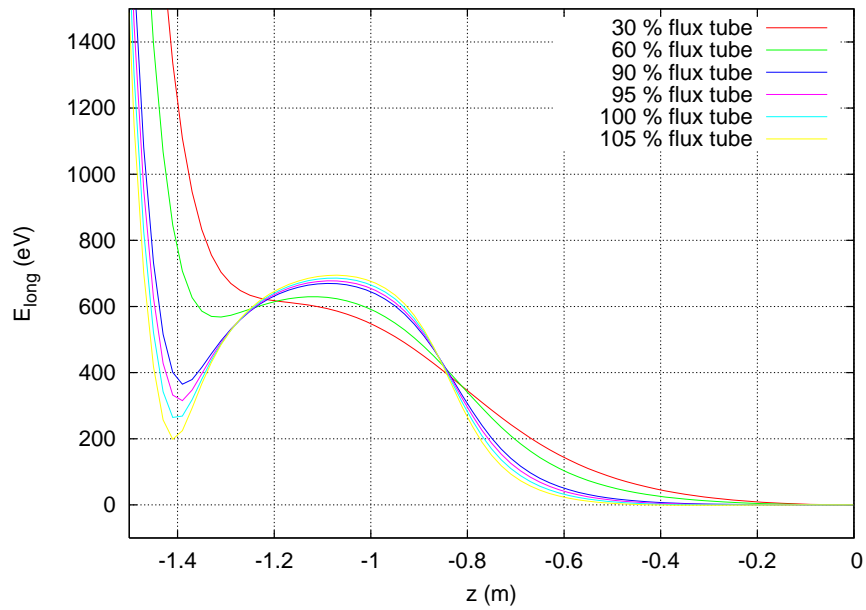


(b) Transmission in adiabatic approximation, please note that only the cut-out from -1.4 m to -0.4 m is shown here

Figure 6.30: Characteristics of the pre-spectrometer in the neutrino mass measurement mode: $U_{wire} = -18.4 \text{ kV}$, $U_{cone} = U_{vessel} - 400 \text{ V} = -18.3 \text{ kV}$. The negative values of the transmission are not important, as the pre-spectrometer is just used as a rough filtering tool. The interesting electrons will pass the spectrometer with excess energies of $\approx 200 \text{ V}$ and are therefore not concerned by the too early retardation.



(a) Potential along magnetic field lines



(b) Transmission in adiabatic approximation, please note that only the cut-out from -1.4 m to -0.4 m is shown here

Figure 6.31: Characteristics of the pre-spectrometer in the optimized transmission mode: $U_{wire} = U_{vessel} = -18.5 \text{ kV}$, $U_{cone} = U_{vessel} + 1 \text{ kV} = -17.5 \text{ kV}$.

6.4 The Penning trap between pre-spectrometer and main spectrometer

Similar to the Troitsk experiment (see section 6.2.1), the KATRIN experiment exhibits a Penning trap between the two MAC-E filters. Two different possibilities have been investigated in order to suppress this trap¹⁴ or empty it before the discharges happen¹⁵. The KATRIN collaboration is confident that it is possible to avoid the discharges between the spectrometer.

6.5 Penning traps in the main spectrometer

Because of the problems Penning traps caused throughout the pre-spectrometer experiments, a thorough investigation of the main spectrometer was started. The important regions for Penning traps are the entrance and the exit region. Here high electric fields coincide with strong magnetic fields thus making it the ideal region for particle storage [Glu06c]. For the preliminary design of the wire electrode system a Penning trap with a depth of 4.7 kV was found at magnetic field lines connecting the flange and the vessel hull, passing the positive potential of the ground electrode. To avoid it, simulations for an improved electrode configuration with a suppressed trap were done.

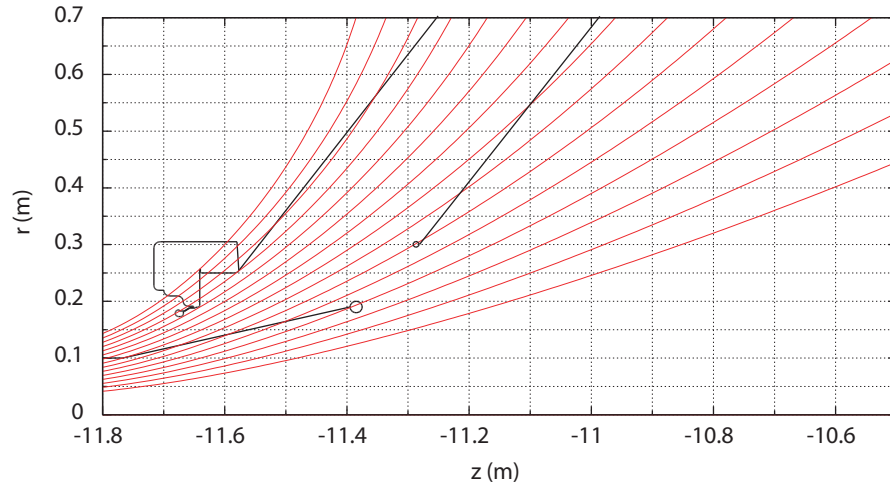
6.5.1 Design requirements

In the search for a suppression of the Penning trap the following points should be fulfilled:

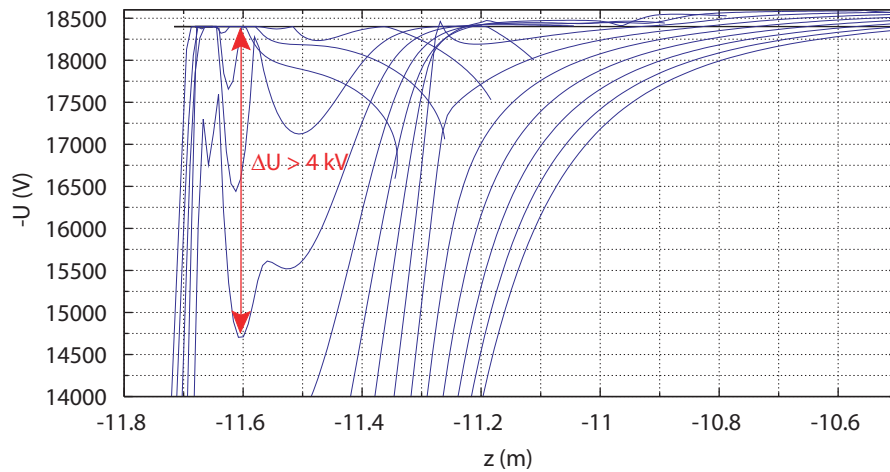
- The trap should be avoided completely or its depth reduced to values not causing background. The pre-spectrometer will investigate the allowed trap depth. Therefore the results of these measurements need to be taken into consideration and the design will only be finalized after the experiments are finished.
- To avoid leading secondary electrons directly from electrode surfaces to the detector, a safety margin of 20 mm should be kept to the maximum flux tube.
- High field strength should be avoided. At the anode it must be smaller than 1.5 MV/m, at the cathode < 1 MV/m (these values are limits obtained from experience at the pre-spectrometer, see section 6.3). This poses some requirements on the distance between ground electrode and shielding electrode: for a potential of nearly 20 kV applied over the gap between them, this gap should have an extent

¹⁴In the first design phase a transport section was foreseen between the two spectrometers. In addition to ensuring the adiabatic transport between pre-spectrometer and main spectrometer, the stored electrons were partially cooled down in this region by energy loss through synchrotron radiation. This does not suppress the Penning trap and its ignition completely. For further information on this see [Ess04].

¹⁵For the current setup with no transport section between the two spectrometers, a wire sweeper is designed. Inbetween the measurements a wire is guided through the section with the traps, perturbing the stored electrons and thus emptying the trap. For further information on this see [Val08]



(a) Magnetic field lines in the entrance region of the main spectrometer



(b) Potential along the magnetic field lines

Figure 6.32: The Penning trap inside the main spectrometer for an earlier design of the electrode system

of at least $\approx 30 - 40$ mm. The curvature of the electrode endpoint influences the field strength and has to be adjusted.

- The total flux tube needs to be transmitted.
- The potential depression in analysing plane (the deviation from $U(r) = \text{const} \equiv U$, see also section 2.2.3 for further explanation) should be kept as low as possible.

To suppress the Penning trap, an additional electrode has to be implemented. Therefore, the design of the entire region (ground electrode, shielding electrode and module ring 02) had to be revised.

Since the main spectrometer will use the same ceramics as the pre-spectrometer, a shielding of the soldering should be taken into consideration. Therefore, the design of the shielding electrode is modeled on the geometry chosen for the pre-spectrometer. Here two possible designs will be presented:

6.5.2 Models for a shielding electrode fitting through the flange

In accordance to the pre-spectrometer, the possibility to move in the shielding electrode through the flange is considered for mounting. Therefore, the maximum radius of the shielding electrode has to be kept in mind for the design.

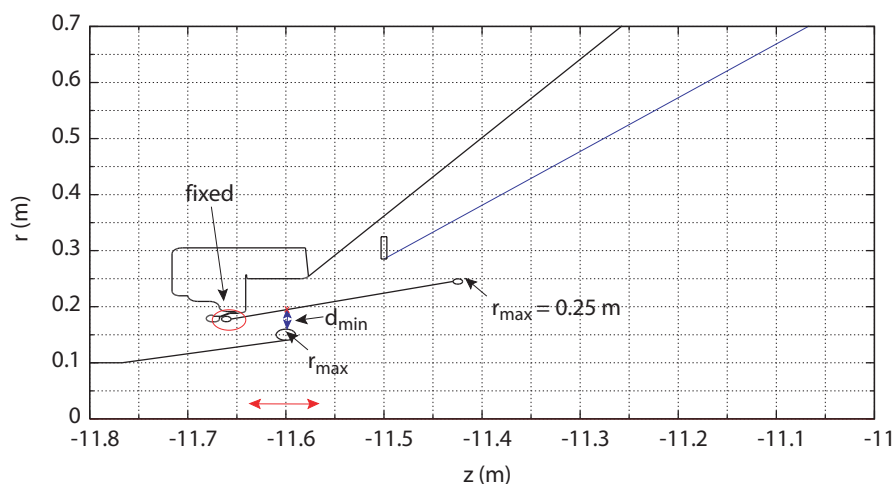


Figure 6.33: Example geometry for the high field region $r < 0.25$ m

The design process can be divided into the following steps:

1. The ground electrode:
Choosing a ground electrode position that has at least 20 mm radial distance to the flux tube as safety margin for mounting
2. The shielding electrode:
Adjusting a shielding electrode with a minimum distance d_{min} to the ground electrode (here $d_{min} = 40$ mm) to avoid too high field strength and to obtain a Penning trap deepness below 100 V. In addition a safety distance to the flux tube should be kept to prevent electrons emitted from the surface from being transported with the flux tube directly to the detector
3. Module ring 02:
Choosing the endpoint with a minimum distance to the shielding electrode of ≈ 60 mm (for mounting), adjusting for ideal Penning trap suppression and easy mechanical insertion

As the Penning trap is located in magnetic field lines leading from the flange to the vessel hull, the basic design of the shielding electrode needs to shield these lines from the positive potential of the ground electrode. In order to remove the trap, the electrode has to have a potential close to the vessel potential to prevent the creation of additional traps. Due to its mounting point at the flange in very close vicinity of the hull, the best solution would be to short-circuit them.

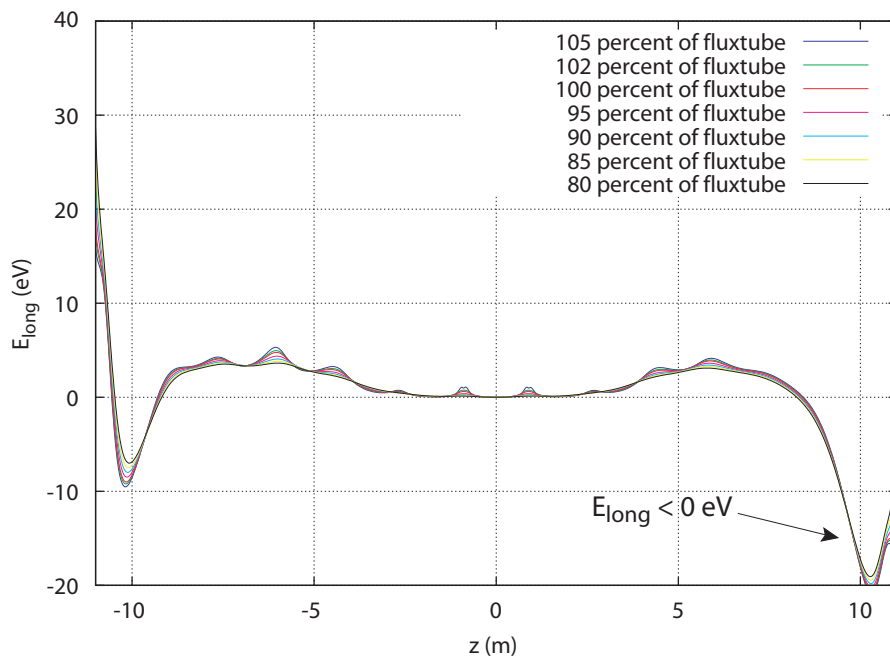
Testing different ground electrode positions, the maximum position of the shielding electrode can be found by the following considerations (see also figure 6.33 for the details): The endpoint of the shielding electrode at the flange is fixed. Using the maximum radius of the ground electrode and assuming a minimum distance d_{min} between ground electrode and shielding electrode to avoid too high field strength, one obtains a second point which the shielding electrode has to pass. The suppression of the Penning trap becomes better for a larger distance between the endpoints of the shielding electrode and the ground electrode. The maximum length of the electrode is then restricted by the flange radius $r = 0.25$ m. Test simulations have shown that this alone does not suppress the Penning trap sufficiently. Therefore, additional measures have to be taken. The module ring 02 has to be extended towards the shielding electrode to suppress the Penning trap completely. The high potential on this electrode decelerates the electrons earlier and thus causes transmission problems. Therefore, the module ring 02 is not parallel to the vessel hull, but one endpoint is shifted closer towards the vessel (see figure 6.33).

In this setup the electrons are retarded too early. To avoid problems the potential of module ring 03 can be adjusted to -18.5 kV (see figure 6.34). Detailed simulations to transmission properties are discussed in reference [Zac08].

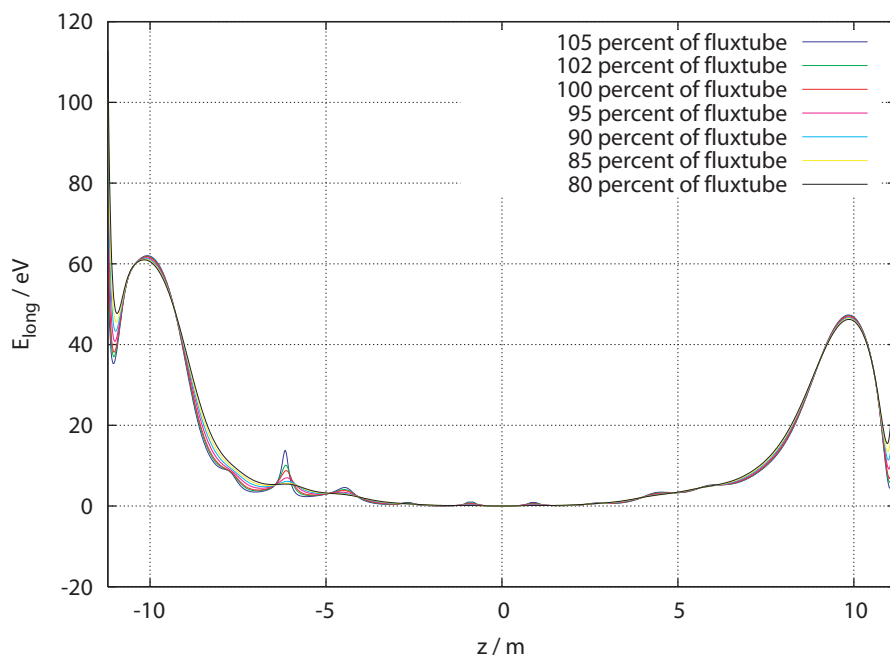
With this configuration the Penning trap can be reduced to a depth of ≈ 200 V (see figure 6.35b).

This shallow trap can still cause background. Applying a more positive potential to the shielding electrode can reduce its depth (see figure 6.36). This theoretical consideration is very hard to realise technically, as the distances at the mounting point are very small and thus prone to high field strength.

As the module ring 02 is positioned very close to the vessel hull, a special holding construction has been designed. It needs to be attached to the vessel in a distance of 10 mm.

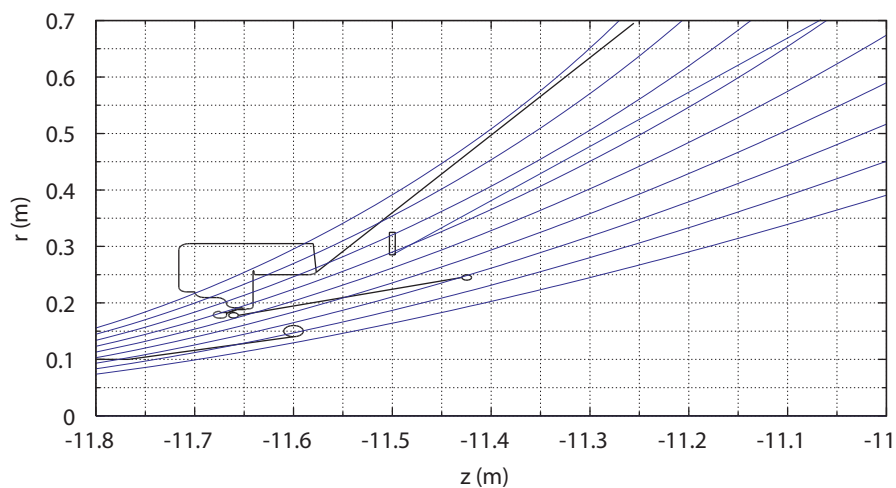


(a) Transmission properties of the new setup for module ring 02 on -18600 V

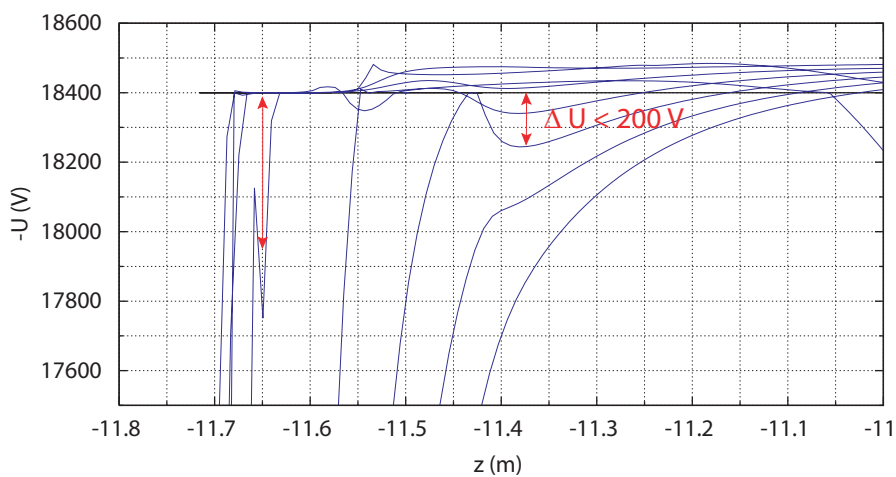


(b) Transmission properties of the new setup for module ring 02 on -18500 V

Figure 6.34: Transmission properties of the new geometry

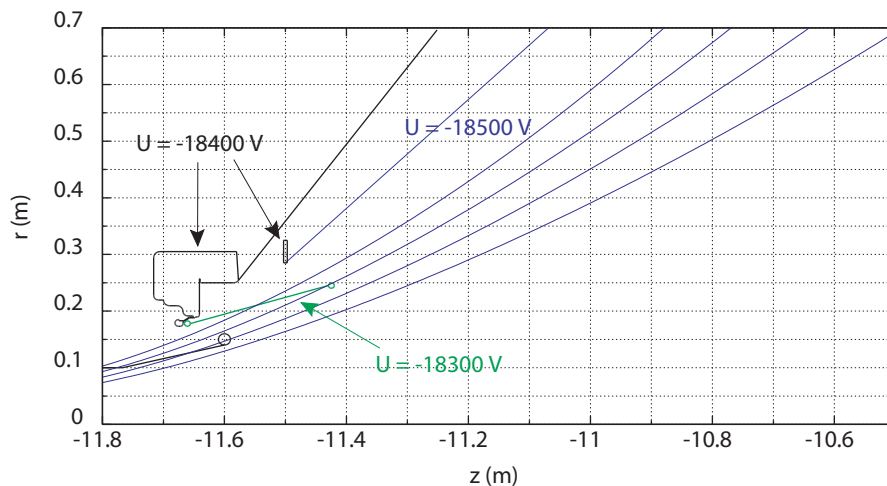


(a) Magnetic field lines in the entrance region of the main spectrometer for an improved setup

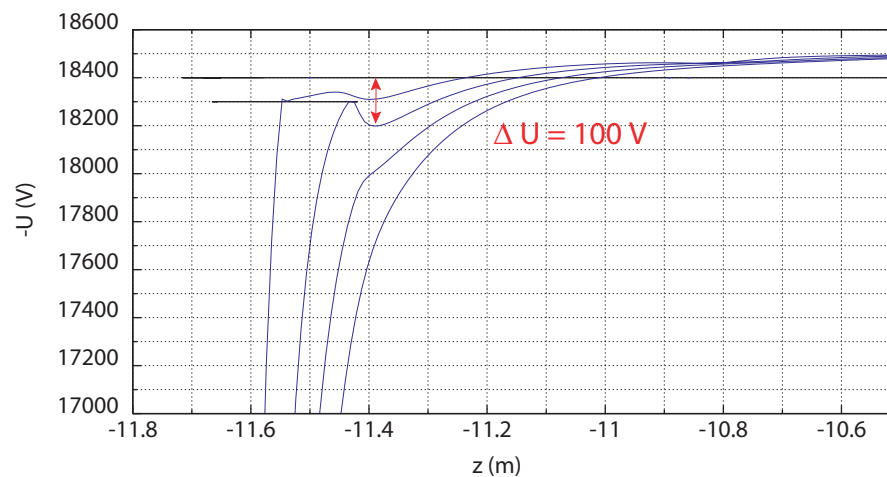


(b) Potential along the magnetic field lines

Figure 6.35: The Penning trap for a geometry with $r < 0.25$ m. The small trap on the left side in 6.35b is due to the ring at the end of the electrode to avoid high field strength. In consultation with the technicians, form and radius of the ring therefore need to be optimised.



(a) Magnetic field lines in the entrance region of the main spectrometer for the shielding electrode on $U = -18300$ V.



(b) Potential along the magnetic field lines for the shielding electrode on $U = -18300$ V.

Figure 6.36: The Penning trap for a geometry with $r < 0.25$ m and a potential of -18300 V applied to the shielding electrode.

6.5.3 Models for a shielding electrode exceeding the flange diameter

The setup proposed above is not possible as measurements of the outer vessel hull have shown it to be in total ≈ 60 mm shorter than specified in the technical drawings (see figure A.1). The mounting structure for module ring 02 has been designed with a safety distance of 10 mm to the vessel hull. This design is therefore not possible and has to be revised. As the geometry has already been optimised, no possibility is seen to reduce the Penning trap while keeping the radius of the shielding electrode $r < 250$ mm. Therefore, new simulations have been started for a design with a radius exceeding 0.25 m. This will not pose major problems for the mounting as for the wire electrode installation an intervention system will be erected inside the vessel. It might also be used for the installation of the shielding electrode.

First measurements at the pre-spectrometer testing dependencies of background on the Penning trap depth hint that the count rate is very sensitive to any residual Penning traps [Glu08]. No quantitative estimate can up to now be made for the critical depth of the Penning trap. Therefore, finalising the design of the shielding electrode has been postponed until a solid bound can be set for the allowed residual depth. Thus, this section will only show that the suppression of the main spectrometer Penning trap to a 10 V level is possible.

For these simulations it was assumed that the end point of the shielding electrode will be fixed at the flange in the same way as it was done in the pre-spectrometer (see figure 6.27). If a quantitative setup is chosen, the exact mounting point should be optimised in close cooperation with the engineers.

The geometry of the shielding electrode can again be designed in several steps, this time with fewer restrictions:

1. Fixing a possible position of the ground electrode with regard to the flux tube.
2. Deriving the slope of a possible shielding electrode: the shielding electrode and ground electrode need to have a minimum spacing d_{min} to avoid high field strength. This point and the mounting point give a line which the shielding electrode will follow.
3. Choosing a possible z-coordinate of the inner ending point. The corresponding r -coordinate is then given by the calculated slope. The position of this point relative to the maximum flux tube needs to be controlled.

The new setup can therefore be defined by several parameters, which can also be seen in figure 6.37:

- The position z_{GE} of the ground electrode:
Previous simulations have shown that it is useful to keep the radius of the ground electrode small, as it is then easier to suppress the Penning trap. In addition, the suppression of too early retardation is easier for smaller radii. As the minimum radius is fixed by the distance to the flux tube, the position of the ground electrode will be characterised by its z -coordinate z_{GE} .

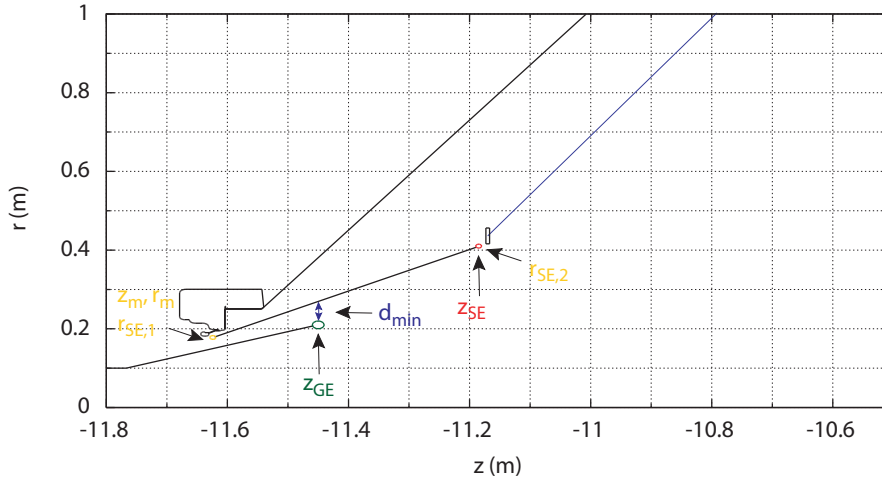


Figure 6.37: Possible setup in the high field region. The parameters noted are the main variables in the simulations.

- The minimum distance d_{min} between ground electrode and shielding electrode:
To avoid field emission between the two electrodes with a potential difference of $\Delta U = 18.6 \text{ kV}$, a distance of at least 30 mm is needed. This value can also be chosen higher.
- The end point z_{SE} of the shielding electrode:
As the minimum distance d_{min} to the ground electrode already gives the slope of the shielding electrode, its endpoint can be characterised only by its z -coordinate. It determines the effective distance between the ground electrode and shielding electrode endpoints, which is a factor for the effectiveness of the trap suppression.
- The radius $r_{SE,1}$ of the shielding electrode end ring:
As seen in figures 6.29a, 6.30a and 6.31a a potential Penning trap is positioned at this ring inside the pre-spectrometer. If this causes discharges (which still has to be investigated), a trap like that has to be suppressed. A possibility is to resize the ring or change its form. This has to be done in close collaboration with the engineers to find out which of the configurations are technically feasible.
- The radius $r_{SE,2}$ of the shielding electrode end ring:
This radius can possibly affect the residual Penning trap. The expected effect is small, but nevertheless should be investigated.
- The exact position of the shielding electrode mounting point z_m, r_m :
This position can be adjusted slightly. Its effect on field strength should be studied.

As no restriction is posed on the shielding electrode¹⁶, systematic tests can be done with several parameters. Up to now, only z_{GE} and z_{SE} were investigated with some detail.

¹⁶neglecting the possible weight of the full metal electrode

The effect of the parameters d_{min} , $r_{SE,1}$, $r_{SE,2}$, z_m and r_m are expected to be low and will therefore only be tested as soon as limits are set for the other parameters.

Varying the parameters z_{GE} and z_{SE} shows that the Penning trap suppression is correlated to the position of the ground electrode and directly depends on the distance Δz between the two electrodes (see table 6.3).

Table 6.3: Penning trap suppression in dependence of z_{GE} and z_{SE} for a minimum distance of $d_{min} = 40$ mm. These values were determined ocularly from figures like 6.38b. Therefore, they are not to be taken as precise values. In addition, only a limited number of field lines have been tracked. This often leads to missing the maximum depth.

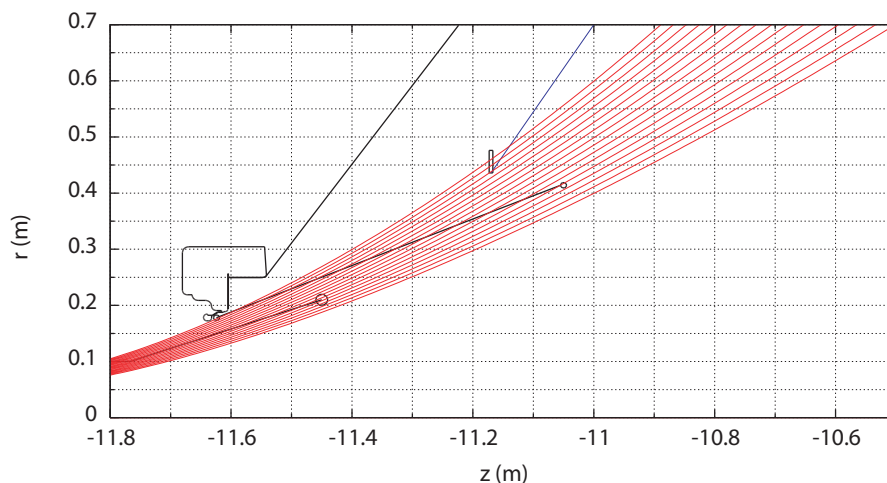
z_{GE} (m)	z_{SE} (m)	Δz (m)	ΔU (V)
-11.50	-11.30	0.20	≈ 170
-11.50	-11.25	0.25	≈ 100
-11.50	-11.20	0.30	≈ 45
-11.45	-11.25	0.20	≈ 170
-11.45	-11.20	0.25	≈ 110
-11.45	-11.15	0.30	≈ 70
-11.40	-11.20	0.20	≈ 290
-11.40	-11.15	0.25	≈ 150
-11.40	-11.10	0.30	≈ 80
-11.35	-11.15	0.20	≈ 270
-11.35	-11.10	0.25	≈ 180
-11.35	-11.05	0.30	≈ 110

As the magnetic field configuration has changed, the next calculations for a $r > 0.25$ m have been done with the new setup. In this configuration stray fields from the CPS and the terrestrial magnetic field have been added, which were compensated by the air coil settings. In general, the size of the Penning trap was reduced and the transmission improved. More information on the configurations can be found in section B.

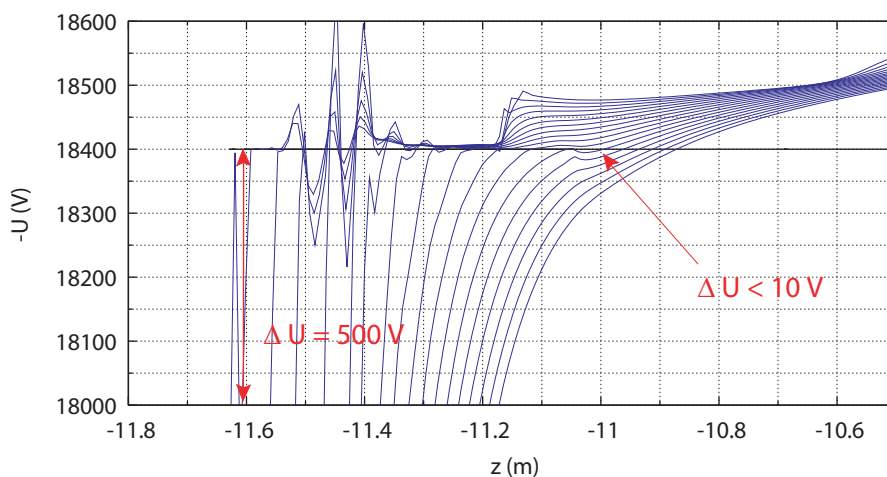
With the example configuration¹⁷ shown in figure 6.37, the Penning trap at the end of the shielding electrode can be reduced to a depth of $\Delta U < 10$ V (see figure 6.38b). The residual trap at the beginning of the shielding electrode has a depth of $\Delta U = 500$ V. It can be optimized by changing the radius of the end ring. Results of the tests at the pre-spectrometer will give a lead how this trap influences the background.

At $z = -11.05$ m the flux tube has a radius of 0.3362 m. Therefore, the distance between the electrode and the magnetic field lines leading directly to the detector is large enough. In this configuration, problems still exist with the transmission of electrons on outer tracks with high angles, but they can be solved by applying a more positive potential to the module ring 03. Simulations are on the way and will be described in reference [Zac08].

¹⁷Parameters: $z_{GE} = -11.45$ m, $r_{GE} = 0.21$ m, $z_{SE} = -11.05$ m, $d_{min} = 0.03$ m, $r_{SE,1} = r_{SE,2} = 0.005$ m and $r_{GE} = 0.010$ m, leading to $r_{SE} = 0.414$ m



(a) Magnetic field lines in the entrance region of the main spectrometer



(b) Potential along the magnetic field lines

Figure 6.38: Possible new electrode configuration. The oscillating structure seen in 6.38b results from a bad discretization of the surface of the shielding electrode. The boundary element method cannot calculate accurate potentials directly on the surfaces there, as they are too large (see also section 3.2).

6.5.4 Conclusion

By adding a shielding electrode to the KATRIN main spectrometer electrode configuration, the Penning traps in the entrance and exit regions can be suppressed. The design has to take into consideration several additional conditions to suppress other background effects, such as field emission. The final design can be pinpointed only after the measurements at the pre-spectrometer with regards to background caused by Penning traps are done.

Up to now only the parameters z_{GE} and z_{SE} have been investigated. Before fixing a configuration, the parameters d_{min} , $r_{SE,1}$, $r_{SE,2}$, z_m and r_m should also be optimised. It has been shown that the initial trap can be suppressed, but still problems exist at the mounting point of the shielding electrode. On a very small area a deep trap can be located, if field lines cross the end ring and the flange, seeing inbetween the positive potential from the ground electrode. This ring structure is implemented to suppress too high field strength. Different solutions have to be considered. There is the possibility for bending this part of the electrode to a circle (see figure 6.39), but this method may not have the required accuracy. Therefore, this design has to be discussed with the engineers.

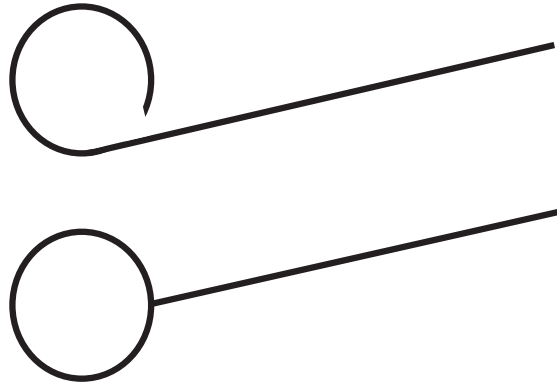


Figure 6.39: Possible end rings for the shielding electrode to avoid high field strength.

7 Summary and outlook

The KATRIN experiment aims to determine the mass of the electron anti-neutrino $m_{\bar{\nu}_e}$ with a sensitivity of $0.2 \text{ eV}/c^2$ (90 % C.L.). This will be done by a precision measurement of the tritium β -spectrum in a small energy interval below the endpoint. The spectrometer works on the principle of magnetic adiabatic collimation with an electrostatic filter. In the scope of this diploma work, questions concerning background and calibration of MAC-E filters were studied within electromagnetic design simulations.

In order to suppress background, a wire electrode will be built into the main spectrometer of the KATRIN experiment, electrostatically reflecting electrons emitted from the vessel hull by radioactivity or cosmic muons. A double wire layer structure was designed to achieve a maximum shielding effect while keeping the amount of additional material inserted into the spectrometer at a minimum. For the installation of these wires, a modular structure was designed. The wires are positioned by comb-like structures, two of which will be connected to form a module. In the cylindrical part and for the big conical part 20 modules will form a ring. Five rings cover the whole cylinder, three rings cover each of the big cones. Tolerance simulations have been conducted to test the consequences of inaccurate mounting of separate modules. The resulting limits show that electrons passing the filter on outer tracks of the spectrometer with high angles are very sensitive to any abrupt changes in the potential. Therefore adjacent module ends are not allowed to have any offset with respect to each other. This result has led to a redesign of the original mounting structure. Now neighbouring modules are mounted on the same rail structure, thus preventing offsets.

To test the accurate mounting of the wire modules and to measure the exact electromagnetic properties of a MAC-E filter, electron sources are needed. As displacements between the modules will mainly be seen by electrons with large angles, the source should provide these. An electron gun based on the photoelectric effect has been built for the pre-spectrometer. Its properties have been simulated within the course of this diploma work. UV-photons are radiated on a hemispherical quartz tip plated with gold on which a potential U_0 is applied. Electrons are emitted from the gold layer by the photoelectric effect and accelerated along the electric field lines to energies of $E = qU_0$. As they have nearly no energy in the beginning, the magnetic field cannot guide the particles. Only after acceleration through the electric field the electrons have transversal energy and will thus move in a cyclotron motion around the magnetic field lines. No more transversal energy can be gained from the electric field. The transport to the magnet is from that point on adiabatic. The angular emission spectrum of the electrons reaching the center of the entrance magnet was derived: The e-gun provides electrons with all angles, but the form of the spectrum is not isotropic. Only few electrons have higher angles. Therefore a source based on this principle is not ideal as a calibration tool for the main

spectrometer. The angular spectrum was used to simulate a measurement that has been conducted at the pre-spectrometer with this source. Simulation and measurement were in concordance.

During the run of this diploma work the influence of changes in design details has been investigated and some structures have been refined. Special emphasis has been put on the steep cone. Module ring 03 will now hold only one wire layer with a total of 40 wires per module. Module ring 02 was originally planned as a full-material electrode. To avoid background, it has also been changed into a wire electrode with a total number of 200 wires. The field strength between wires in these modules is found to lie below $E = 400 \text{ kV/m}$, a threshold for field emission determined by predecessor experiments. Combining high electric and strong magnetic fields, the spectrometer section of the KATRIN experiment enables the formation of particle traps. These lead to an increase of background and unstable vacuum and electric potential conditions. Therefore they should be suppressed whenever possible. Measurements at the pre-spectrometer have revealed a Penning trap existing in the entrance region between flange and cone. It was discovered due to strong discharges depending on the magnetic and electric field configurations. Simulations have been performed in co-operation with K. Valerius and F. Glück to design an additional electrode that suppresses the trap. Additionally the form of the ground electrode has been modified. The new electrodes have been built and installed in the pre-spectrometer. Measurements concerning the behaviour of the residual traps are presently being carried out and deliver promising results.

Simulations searching for Penning traps inside the main spectrometer have been conducted in this diploma work. The preliminary setup of the electrode system hosted a Penning trap with a depth of $\Delta U \approx 5 \text{ kV}$ at the entrance region of the spectrometer between flange and vessel hull. Different configurations for an additional electrode shielding the trap have been investigated. Under the condition that the shielding electrode should be removable through the spectrometer flange, a design has been found with which the Penning trap can be suppressed to $\Delta U \approx 200 \text{ V}$ or even smaller values if the potential applied to it is lowered. If the size of the shielding electrode would be allowed to exceed the flange radius of $r_{flange} = 0.25 \text{ m}$, configurations with very low trap depth can be found. As the investigations at the pre-spectrometer are not finished yet, a decision on the final design is still pending.

After the pre-spectrometer measurements are finished, the design of the main spectrometer shielding electrode will be completed. Special attention has to be paid to the outer ring of the electrode which is used to shield the end of the electrode from high field strength. Here locally small, but very deep Penning traps are found.

Once the electrode design is completed, the adiabaticity needs to be tested in simulations. This requires some additional development effort on the simulation software, namely making the program *traj.c* compatible for *elcd3_3* simulations in high magnetic fields. Another option are test simulations with a comparable setup in *elcd3_2*.

A Technical drawings

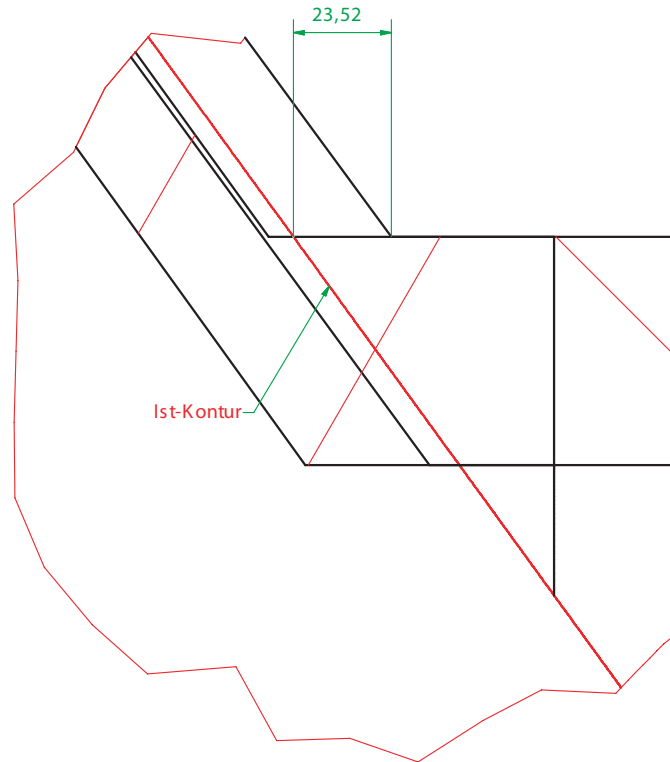


Figure A.1: Lasertracking measurement of points on the vessel hull were fitted with cones to the form of the spectrometer (red line). This lead to the assumption that the spectrometer varies from the technical drawing. In this figure the difference between the fitted cone (red) and the initial technical drawing (black lines) for the exit side of the main spectrometer is shown. These measurements pointed to a slight asymmetry in the setup, the detector side has a difference of 24.5 mm while at the source side a difference of 36.5 mm was fitted.

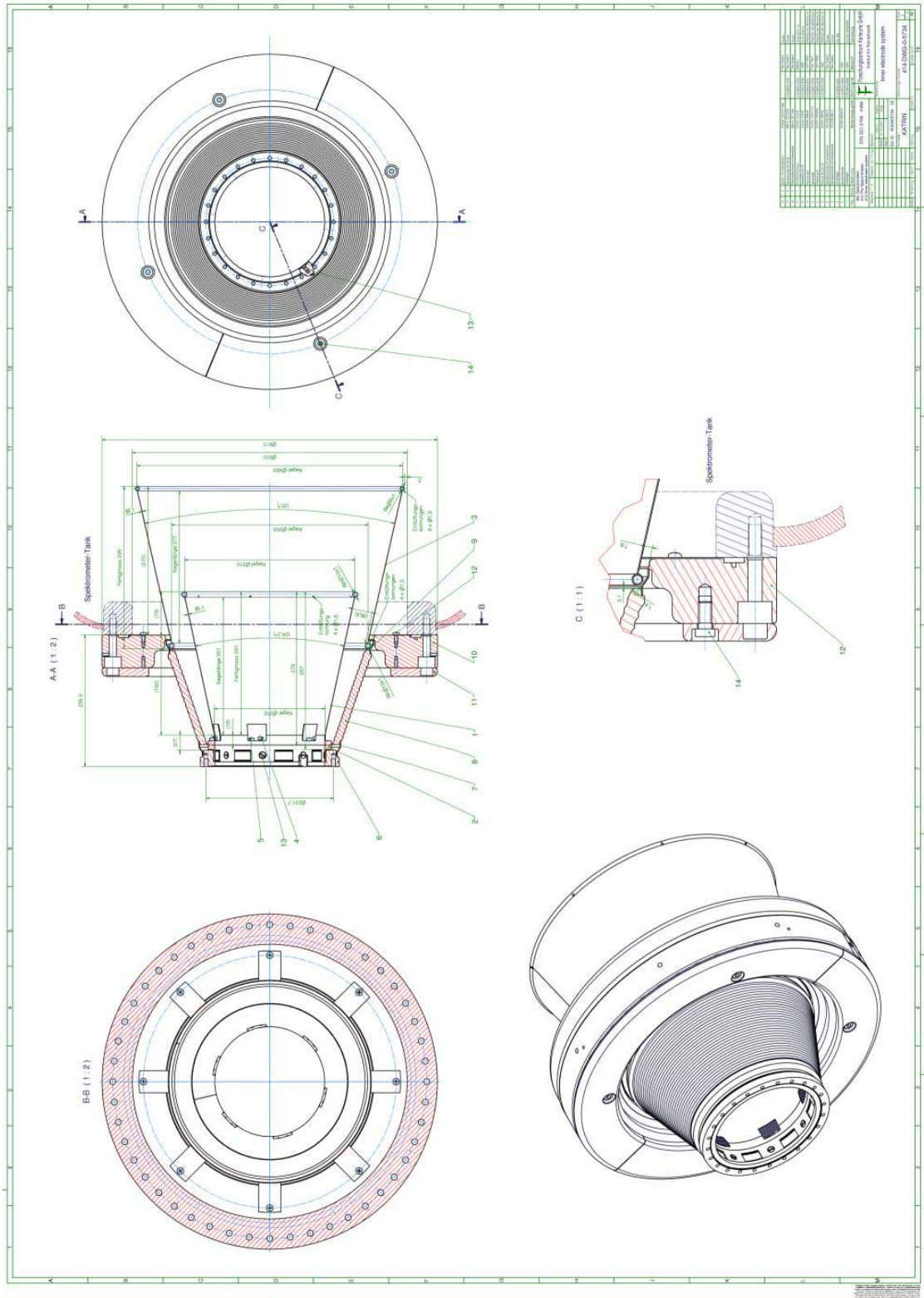


Figure A.2: Technical drawing of the shielding electrode and new ground electrode for the pre-spectrometer

B The magnetic field design

The coil parameters used as input for the program package *magfield2*.

6 T detector magnet Last revision 29.11.2007.

22					
-16.490	0.227	0.0430	0.320	2120000.	entrance magnet PS
-12.130	0.227	0.0430	0.320	2120000.	entrance magnet MS
12.220	0.220	0.0215	0.500	3225000.	pinch magnet MS
13.820	0.270	0.0202	0.700	4230000.	detector magnet
<hr/>					
-6.800	6.000	0.0500	0.100	130.	air coils
-4.950	6.000	0.0500	0.100	130.	
-4.050	6.000	0.0500	0.100	100.	
-3.150	6.000	0.0500	0.100	110.	
-2.250	6.000	0.0500	0.100	140.	
-1.350	6.000	0.0500	0.100	140.	
-0.450	6.000	0.0500	0.100	135.	
0.450	6.000	0.0500	0.100	135.	
1.350	6.000	0.0500	0.100	140.	
2.250	6.000	0.0500	0.100	140.	
3.150	6.000	0.0500	0.100	140.	
4.050	6.000	0.0500	0.100	160.	
4.950	6.000	0.0500	0.100	160.	
6.800	6.000	0.0500	0.100	-1050.	
<hr/>					
0.000	20.000	0.1000	200.0	-3246.	earth magnetic field, component
-38.500	0.115	0.0200	15.00	53100000.	
-27.200	0.065	0.0400	6.500	29000000.	
-20.000	0.120	0.0400	6.500	25170000.	

3.5 T detector magnet Last revision 13.12.2007.

22					
-16.490	0.227	0.0430	0.320	2120000.	entrance magnet PS
-12.130	0.227	0.0430	0.320	2120000.	entrance magnet MS
12.220	0.220	0.0215	0.500	3225000.	pinch magnet MS
13.820	0.270	0.0202	0.700	2540000.	detector magnet
-6.800	6.000	0.0500	0.100	60.	air coils
-4.950	6.000	0.0500	0.100	80.	
-4.050	6.000	0.0500	0.100	100.	
-3.150	6.000	0.0500	0.100	100.	
-2.250	6.000	0.0500	0.100	150.	
-1.350	6.000	0.0500	0.100	150.	
-0.450	6.000	0.0500	0.100	150.	
0.450	6.000	0.0500	0.100	150.	
1.350	6.000	0.0500	0.100	160.	
2.250	6.000	0.0500	0.100	160.	
3.150	6.000	0.0500	0.100	150.	
4.050	6.000	0.0500	0.100	130.	
4.950	6.000	0.0500	0.100	90.	
6.800	6.000	0.0500	0.100	-300.	
0.000	20.000	0.1000	200.0	-3246.	earth magnetic field, component
-38.500	0.115	0.0200	15.00	53100000.	
-27.200	0.065	0.0400	6.500	29000000.	
-20.000	0.120	0.0400	6.500	25170000.	

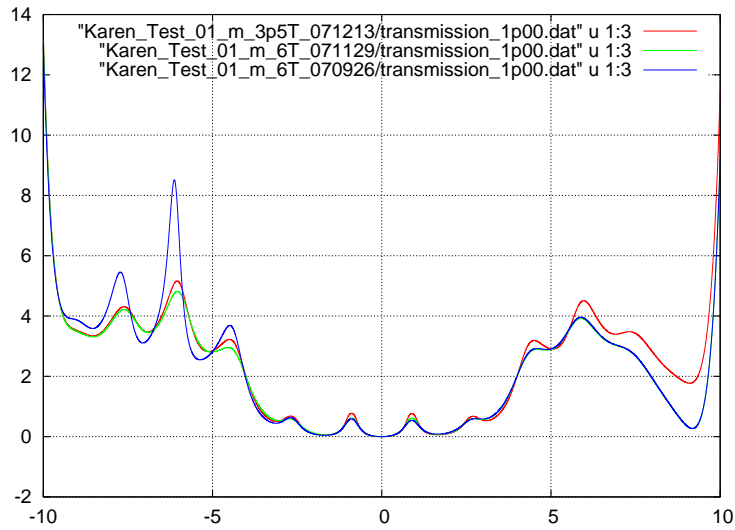


Figure B.1: The transmission of the full flux tube for the different magnetic field configurations

List of Figures

1.1	The solar neutrino flux divided into the different emission processes . . .	2
1.2	The zenith angle distribution for Sub-GeV neutrino energies	4
1.3	The neutrino flux of flavour μ, τ versus the flux of electron neutrinos . . .	5
1.4	Transition probability $\bar{\nu}_e \rightarrow \bar{\nu}_e$	6
1.5	Oscillation parameters from KamLAND	6
1.6	Favoured and excluded regions for neutrino oscillation parameters	8
1.7	A timeline of the evolution of the Universe	9
1.8	Content of the Universe in the Λ CDM Universe	12
1.9	CMBR distribution for different temperature sensitivities	12
1.10	CMB fluctuation and polarization measured by WMAP	13
1.11	Angular power spectrum measured by the WMAP project	14
1.12	Angular power spectrum simulated for different neutrino masses	15
1.13	The neutron decay as an example for a β^- -decay	17
1.14	Schematic view of a β spectrum	18
1.15	Form of the β -spectrum for different neutrino masses	19
2.1	Schematic drawing of a MAC-E filter	23
2.2	Theoretical transmission function for a MAC-E filter	24
2.3	Definition of the angle Θ	24
2.4	The influence of field inhomogeneities on the transmission function	29
2.5	Illustration of the wire electrode principle	30
2.6	Modular design of the KATRIN main spectrometer wire electrode	31
2.7	The total KATRIN setup	32
2.8	Schematic view of the WGTS and the gaseous T_2 density profile	33
2.9	Segmentation of detector area	34
3.1	Illustration of Biot-Savart's law	35
3.2	Magnetic field induced by loop	36
3.3	The central convergence circle	37
3.4	Convergence radius for a two-coil system	38
3.5	Multiple source points	38
3.6	Input parameters for the magfield2 program	40
3.7	Illustration of the remote source point	40
3.8	Input parameters for the magfield3 program	42
3.9	The different magnetic field configurations for magfield2 and magfield3 . .	43
3.10	Example for inaccuracies in the BEM calculations	46
3.11	Graphic explanation of input parameters for elcd3_2	47

3.12	Input for <i>elcd3_2</i>	48
3.13	The spectrometer vessel in form of the input for <i>elcd3_3</i>	48
3.14	Geometry input parameters in <i>elcd3_3</i>	49
3.15	Different perspectives of the main spectrometer seen with <i>rootsim</i>	51
4.1	Geometry setup for the tolerance simulations	56
4.2	Potential depression for original input with no displacements	57
4.3	Transmission of outer electrons for original input with no displacements	58
4.4	Schematic view of the wire electrode displacements	59
4.5	Transmission problems due to a displacement of module ring 09 by -1 mm	60
4.6	Changes in the transmission for displacements towards the vessel hull	61
4.7	Technical drawing of the comb structure in the radial plane	62
4.8	A tooth as implemented in <i>elcd3_3</i> simulations	62
4.9	Schematic close-up view of the mounting structure in the conical part	63
4.10	Graphic illustration of equation (4.1)	64
4.11	Schematic view of setup for electric field strength simulations	65
5.1	Simulated potential depressions in the spectrometers	68
5.2	Simulated magnetic field strength depressions in the spectrometers	68
5.3	A gold-plated electron gun tip	70
5.4	Main components of the pre-spectrometer electron gun	70
5.5	Electric field lines for a circle and a polyangular	72
5.6	Sketch of the e-gun tip with the starting points	72
5.7	Electron gun setup for <i>elcd3_2</i>	73
5.8	An electron path from electron gun tip to center of the entrance magnet	74
5.9	The kinetic energies for an electron starting at the electron gun tip	75
5.10	Longitudinal energy for an electron not reaching the entrance magnet	76
5.11	Dependency of the angle Θ on the starting radius at the tip	77
5.12	Schematic illustration of the angular dependency on the emission point	78
5.13	Starting angle at the electron gun tip calculated with different models	79
5.14	Conversion line emission to area emission	80
5.15	Angular distribution at the center of the entrance magnet	80
5.16	Transmission function measurement $1000S$	81
5.17	The total transmission function as a convolution of its components	82
5.18	Transmission functions calculated for different starting energies	83
5.19	Transmission function for all energies added up	84
5.20	Angular distribution of electrons reaching the MCP	84
5.21	Measured MCP efficiency	85
5.22	Transmission function with and without MCP correction	86
5.23	Comparison of measured and simulated transmission function	86
5.24	Comparison of measured and simulated transmission function - with noise	87
6.1	The Paschen curve $U(p \cdot d)$	90
6.2	The breakdown potential $U(p \cdot d)$ for different gases	91

6.3	Crossed electric and magnetic fields	93
6.4	Electron motion in a cylinder with radial electric and axial magnetic field	94
6.5	Schematic breakdown conditions: dependence on magnetic and electric field	95
6.6	Schematic view of electron movent inside trap	96
6.7	A Penning trap for ion spectroscopy	97
6.8	Experimental ignition curves for various pressure	98
6.9	Cathode to cathode and vacuum to vacuum Penning traps	99
6.10	Schematic view of the Troitsk experimental setup	100
6.11	Schematic view of the improved Mainz setup	102
6.12	Schematic view of the Mainz I setup	103
6.13	Location and depth of Penning traps in the Mainz I setup	104
6.14	Schematic view of the Mainz 2 setup	105
6.15	Location and depth of Penning traps in the Mainz II setup: no insulator .	106
6.16	Location and depth of Penning traps in the Mainz II setup: with insulator	108
6.17	Schematic view of the Mainz III setup	109
6.18	Potential wells in the low magnetic field region, Mainz III	110
6.19	Penning traps for Mainz III with potential on the ground electrodes . . .	111
6.20	Schematic view of the pre-spectrometer setup to 2007	112
6.21	Soldering joint at the ceramic insulator	113
6.22	Welding seam at the pre-spectrometer ground electrode	114
6.23	Magnetic field lines with a Penning trap in the KATRIN pre-spectrometer	115
6.24	Dependency of the ignition voltage on the magnet current	118
6.25	Magnetic field lines: symmetric magnetic field configuration and positive potential	119
6.26	Magnetic field lines: asymmetric magnetic field configuration and positive potential	120
6.27	Technical drawing of mounting point for the additional electrode	122
6.28	The pre-spectrometer with shielding electrode and new ground electrode .	123
6.29	Characteristics of the pre-spectrometer: normal measurement mode . . .	124
6.30	Characteristics of the pre-spectrometer: neutrino mass measurement mode	125
6.31	Characteristics of the pre-spectrometer: optimized transmission mode . .	126
6.32	The Penning trap inside the main spectrometer	128
6.33	Example geometry for the high field region	129
6.34	Transmission properties of the new geometry	131
6.35	The Penning trap for a geometry fitting through the flange	132
6.36	The Penning trap for a geometry fitting through the flange at -18300 V .	133
6.37	Possible setup in the high field region	135
6.38	Possible new electrode configuration	137
6.39	Possible end rings for the shielding electrode to avoid high field strength .	138
A.1	Lasertracking measurement on the vessel hull	141
A.2	Technical drawing: shielding electrode and ground electrode (pre-spectrometer)	142
B.1	100 % transmission for the different magnetic field configurations	144

List of Tables

1.1	Best-fit parameters for the three-year WMAP data	15
1.2	Constraints on the neutrino mass for different data sets	16
2.1	Parameters of the KATRIN main spectrometer wire electrode	31
3.1	Number of terms n_{min} needed to achieve double precision accuracy	39
4.1	Results of the design simulations: maximum displacement in radial direction	57
4.2	Number of wires for the different module rings	60
4.3	Electrid field strength on a wire surface simulated of one wire	64
4.4	Electrid field strength on a wire surface simulated of three wires	65
5.1	Maximum starting radius of electrons reaching the entrance magnet	78
6.1	Dependence of ignition on system pressure	116
6.2	Dependence of ignition on sytem pressure II	117
6.3	Penning trap: influence of distance between shielding and ground electrode	136

Bibliography

- [Aha05] B. Aharmim et al., Phys. Rev. C **72** (2005)
- [Ahn06] M. H. Ahn et al, Phys. Rev. D **74** (2006) 072003
- [Ahr01] J. Ahrens et al, Ice Cube Preliminary Design Document, 2001
- [Alt03] C. Weinheimer, Laboratory Limits on Neutrino Masses,
in: G. Altarelli and K. Winter (Eds.), Neutrino Mass, Springer, 2003
- [And59] P. Anderson, Phys. Rev. **115** (1959) 553 - 554
- [Ara05] T. Araki et al., Nature **436** (2005) 499 - 503
- [Ard06] F. Ardellier et al., Double Chooz Proposal (2006)
arXiv: hep-ex/0606025 v4
- [Ash05] Y. Ashie et al., Phys. Rev. D **71** (2005)
- [Bah64] J. N. Bahcall, Phy. Rev. Let. **12** 1964 300 - 302
- [Bah05] J. Bahcall, ApJ **621** (2005) L85
- [Bio87] R. M. Bionta, Phys. Rev. **58** (1987) 1494 - 1496
- [Bor00] B. Bornschein, Dissertation,
Institut für Physik, Johannes Gutenberg-Universität Mainz, 2000
- [Bor02] L. Bornschein, Dissertation,
Institut für Physik, Johannes Gutenberg-Universität Mainz, 2002
- [Dav64] R. Davis, Phy. Rev. Let. **12** (1964) 303 - 305
- [Dav06] Y. I. Davydov, 2006
arXiv: physics/0409156 v2
- [Deh89] H. G. Dehmelt, Nobel Prize lecture, 1989
- [Dol02] A. D. Dolgov, 2002
arXiv: hep-ph/0202122 v2
- [Dos06] N. Doss et al., Phys. Rev. C **73** 025502 (2006)

- [Dun07] J. Dunmore, KATRIN internal document, 2007
BSCW: Review of Detector Design SUMMER 07
- [ELOG] Electronic log book of the pre-spectrometer, KATRIN internal document
<http://www-ik.fzk.de:8080/pre-spectrometer>
- [Ess04] K. Essig, Diploma thesis
Helmholtz-Institut für Strahlen- und Kernphysik
Rheinische Friedrich-Wilhelms-Universität Bonn, 2004
- [Fer34] E. Fermi, Zeitschrift für Physik **88** (1934) 161 - 177
- [Fla04] B. Flatt, Dissertation
Institut für Physik, Johannes Gutenberg-Universität Mainz, 2004
- [For07] J. Formaggio and B. Monreal, KATRIN internal document, 2007
BSCW: BASI - Physics
- [Fra06] F. Fränkle, Diploma thesis
Institut für Kernphysik, Forschungszentrum Karlsruhe, 2006
- [Fra07] F. Fränkle, KATRIN internal document, 2007
BSCW: Detector - Electron Gun
- [Fow28] R. H. Fowler, F. R. S. and Dr. L. Nordheim
Proc. Roy. Soc. London. **119** (1928) 173 - 181
- [Glu04] F. Glück, KATRIN internal document, 2004
BSCW: EMD - Programs - electric fields
- [Glu05] F. Glück, KATRIN internal document, 2005
BSCW: EMD - Background
- [Glu06a] F. Glück, KATRIN internal document, 2006
BSCW: EMD - Programs - magnetic fields
- [Glu06b] F. Glück, KATRIN internal document, 2006
BSCW: EMD - Task meetings - 05-05-06 Münster
- [Glu06c] F. Glück, KATRIN internal document, 2006
95-TRP-4153-C1-FGlueck.ppt
- [Glu06d] F. Glück, KATRIN internal document, 2006
BSCW: EMD - Task meetings - 11-12-06 Fulda
- [Glu07a] F. Glück et al., KATRIN internal document, 2007
BSCW: EMD - Pre-spectrometer - Penning Trap Investigations
- [Glu07b] F. Glück, KATRIN internal document, 2007
BSCW: EMD - Pre-spectrometer - Penning Trap Investigations

- [Glu07c] F. Glück et al., KATRIN internal document, 2007
BSCW: EMD - Pre-spectrometer - Penning Trap Investigations
- [Glu08] F. Glück, priv. com., 2008
- [Gol95] D. Goldmann, Diploma thesis
Institut für Physik, Johannes Gutenberg-Universität Mainz, 1995
- [Hae53] R. Haefer, *Acta Physica Austriaca* **7** (1953) 52
- [Hae53] R. Haefer, *Acta Physica Austriaca* **7** (1953) 251
- [Ham] Hamamatsu product documentation for Deuterium Lamp L6565
<http://www.hamamatsu.com>
- [Han06] S. Hannestad, 2006
arXiv: hep-ph/0602058 v1
- [Har89] M. Hara et al., *Cryogenics* **29** (1988) 448 - 456
- [Hir87] K. Hirata, *Phys. Rev.* **58** (1987) 1490 - 1493
- [KAT04] The KATRIN collaboration, KATRIN Design Report 2004
FZKA Scientific Report 7090
- [KAT06] Komitee für Astroteilchenphysik (KAT), 2006
Kosmische Spurensuche - Astroteilchenphysik in Deutschland
- [Kaz07] O. Kazachenko, private communication, January 2007
- [Kla97] H.-V. Klaptor-Kleingrothaus, K. Zuber: *Teilchenastrophysik*
Teubner Verlag 1997
- [Kra03] Ch. Kraus, Dissertation
Institut für Physik, Johannes Gutenberg-Universität Mainz, 2003
- [Kra05] Ch. Kraus, *Euro Phys. J. C* **40**, 447 - 468 (2005)
- [Kri07] J. R. Kristiansen, Gausdal, 2007
Talk at the Nordic Winter School
- [Kri06] J. R. Kristiansen et al., *Phys. Rev. D*, **75** (2007)
- [Lan67] L. D. Landau und E. M. Lifschitz, *Lehrbuch der theoretischen Physik VIII*
Elektrodynamik der Kontinua, Akademie Verlag Berlin, 1967
- [Les06] J. Lesgourgues and S. Pastor, *Phys. Rep.* **429** (2006) 307 - 379
- [Lob01] V. M. Lobashev, *Nuclear Physics B* **90**, 280 - 286 (2001)
- [Mat99] J. C. Mather et al., *ApJ* **512** (1999) 511 - 520

- [Mue02] B. Müller (now: Ostrick), Diploma thesis
Institut für Physik, Johannes Gutenberg-Universität Mainz, 2002
- [Mur06] H. Murayama, Oscillation Parameter Plots, 2007
- [Ost08] B. Ostrick, Dissertation (in prep.)
Institut für Kernphysik, Westfälische Wilhelms-Universität Münster, 2008
- [Pas89] F. Paschen, Annalen der Physik **273** 5, 1889
- [Pau30] W. Pauli, Collected Scientific Papers
Eds. Kronig & Weisskopf, Vol 2, 1316 - 1317
- [Pic90] A. Picard, Dissertation
Institut für Physik, Johannes Gutenberg-Universität Mainz, 1990
- [Pic92] A. Picard et al, Nucl. Instr. Meth. **63** (1992) 345 - 358
- [Pyr] Pyrometerhandbuch, Firmenschrift der IMPAC Infrared GmbH, 2004
- [Sch01] J.-P. Schall, Diploma thesis
Institut für Physik, Johannes Gutenberg-Universität Mainz, 2001
- [Sis04] M. Sisti et al., Nucl. Instr. Meth. A **20** (2004) 125 - 131
- [Smo08] J. Smollich, Diploma thesis (in prep.)
Institut für Kernphysik, Westfälische Wilhelms-Universität Münster, 2008
- [Spe07] D. N. Spergel et al, ApJS **170** 377 - 408
- [Ste07] M. Steidel, KATRIN internal document, 2006
BSCW: Review of Detector Design SUMMER 07
- [Tow10] J. S. Townsend, The Theory of ionization of gases by collision
published by Constable & Company LTD, 1910
- [Tüm07] T. Tümmeler, Dissertation
Institut für Kernphysik, Westfälische Wilhelms-Universität Münster, 2007
- [Ulr00] H. Ulrich, Diploma thesis
Institut für Physik, Johannes Gutenberg-Universität Mainz, 2000
- [Val04] K. Valerius, Diploma thesis
Helmholtz-Institut für Strahlen- und Kernphysik
Rheinische Friedrich-Wilhelms-Universität Bonn, 2004
- [Val06] K. Valerius, KATRIN internal document, 2006
95-TRP-4156-C1-KValerius.pdf
- [Val08] K. Valerius, Dissertation (in prep.)
Institut für Kernphysik, Westfälische Wilhelms-Universität Münster, 2008

- [Voe08] S. Vöcking, Diploma thesis
Institut für Kernphysik, Westfälische Wilhelms-Universität Münster, 2008
- [Wei93] Ch. Weinheimer, Dissertation
Institut für Physik, Johannes Gutenberg-Universität Mainz, 1993
- [WMAP] The WMAP mission, official homepage: <http://map.gsfc.nasa.gov/>
- [Wol07] J. Wolf, shielding electrode design meeting in Karlsruhe, 12.01.2007
- [Wol08] I. Wolff, Diploma thesis (in prep.)
Institut für Kernphysik, Westfälische Wilhelms-Universität Münster, 2008
- [Yao06] W.-M. Yao, J. Phys. G: Nucl. Part. Phys. **33** (2006) 1 - 1231
- [Zac08] M. Zacher, Diploma thesis (in prep.)
Institut für Kernphysik, Westfälische Wilhelms-Universität Münster, 2008
- [Zbo06] M. Zboril, Diploma thesis
Faculty of Nuclear Science and Physical Engineering, Department of Physics
Czech Technical University in Prague, 2006
- [Zub04] K. Zuber, Neutrino Physics
Institute of Physics Publishing Bristol and Philadelphia, 2004